A serendipitous MeerKAT discovery of a neutral hydrogen (H I) rich galaxy group with megaparsec-scale filamentary-like structure.

By

Graham David LAWRIE



UNIVERSITY OF THE
WITWATERSRAND,
JOHANNESBURG

School of Physics
UNIVERSITY OF THE WITWATERSRAND

Submitted in partial fulfilment of the requirements for the degree of MASTER OF SCIENCE (MSC) IN PHYSICS in the Faculty of Science.

May 5, 2023

Supervisor: Prof. Roger DEANE

UNIVERSITY OF THE WITWATERSRAND

Abstract

Faculty of Science
School of Physics

Master of Science (MSc) in Physics

A serendipitous MeerKAT discovery of a neutral hydrogen (H I) rich galaxy group with megaparsec-scale filamentary-like structure.

by Graham David LAWRIE

Supervisor: Prof. Roger DEANE

Neutral hydrogen (H I) makes up a significant portion of cold gas in galaxies, and is an important component within galaxy formation and star formation. Environmental effects within cosmological overdensities such as galaxy clusters and groups are known to dramatically influence galaxy evolution, and H I content and morphology are important diagnostics thereof. This thesis reports the discovery of an H I galaxy group of 32 galaxies at $z \sim 0.041$, as well as detail the H I and multiwavelength properties. The group, being H I-rich and spatially-resolved, allows for a detailed study of the role of the environment in the early stages of transforming its members' gas content. Star formation rate (SFR) for individual galaxies is derived from near and mid-infrared photometry, and host galaxy study is done using sub-arcsecond imaging with Dark Energy Survey. The group appears to have a Mpc-scale filamentary-like structure. The data used in this project was observed as part of the MeerKAT Galaxy Cluster Legacy Survey (MGCLS), a radio continuum survey, but shows the potential for commensal spectral line and continuum science with modern radio interferometers.

Declaration of Authorship

I, Graham David LAWRIE, declare that the thesis, which I hereby submit for the degree of MSc in Physics at the University of the Witwatersrand, is my own work and has not previously been submitted by me for a degree at this or any other tertiary institution.

Signature: 

Date: 05/05/2023

Acknowledgements

To my supervisor, Prof Roger Deane. Thank you for always being encouraging and supportive, I could not have asked for a better supervisor. The guidance and opportunity you have given me throughout this degree has been invaluable to say the least. Even before starting this thesis you introduced me to the wonderful world of astronomy and I will forever be grateful. Working together has been an absolute pleasure and I look forward to continuing on to do a PhD under your guidance.

Thank you to all my colleagues in the office. After two years I now find myself with an entirely new friend group that provides assistance with work as well as brilliant company during lunch. A special thanks to William, who was often very relatable and ensured I never had to experience new challenges alone. Also thanks to Shilpa, who might not have been an office mate but was always willing to help and acted as an ideal role model.

To my family, I thank you all for the support. Firstly to my mom, for the unending encouragement, love, and motivation. To Kevin and Jana for the occasional oasis from stress in the form of our weekend braais, and for always being willing to help with adulting. To Denzil, Liz and Kyle for being the light at the end of the tunnel each semester, as I know I will have a wonderful time with you all when visiting home in the holiday.

To Laetitia, thank you for long calls after a days work, the games and movies, and the prized memories we've made together over the past two years. I would not have been able to get through it all without you.

The financial assistance of the South African Radio Astronomy Observatory (SARAO) and the National Research Foundation (NRF) towards this research is hereby acknowledged (www.sarao.ac.za, www.nrf.ac.za). We acknowledge the use of the ilifu cloud computing facility (www.ilifu.ac.za).

Contents

Abstract ii

Declaration of Authorship iii

Acknowledgements iv

1 Introduction 1
- 1.1 Galaxy evolution . . . 1
  - 1.1.1 Galaxy formation . . . 1
  - 1.1.2 Internal feedback mechanisms . . . 2
  - 1.1.3 Environmental effects on galaxies . . . 3
  - 1.1.4 The star formation main sequence . . . 4
- 1.2 Large-scale structure . . . 5
  - 1.2.1 Overview . . . 5
  - 1.2.2 Clusters . . . 6
  - 1.2.3 Filaments . . . 8
  - 1.2.4 Groups . . . 8
  - 1.2.5 Tendrils . . . 9
  - 1.2.6 Voids . . . 10
- 1.3 Importance of H I . . . 12
  - 1.3.1 Overview of neutral hydrogen . . . 12
  - 1.3.2 H I mass function . . . 13
  - 1.3.3 Large scale-structure effects on H I content . . . 14
  - 1.3.4 H I in relation to star formation . . . 15
- 1.4 Thesis outline . . . 16

2 Observations, data reduction, and ancillary data 20
- 2.1 Radio interferometry overview . . . 20
- 2.2 MeerKAT . . . 23
- 2.3 MeerKAT Galaxy Cluster Legacy Survey . . . 23
- 2.4 Calibration and imaging . . . 24
  - 2.4.1 First generation calibration (1GC) . . . 26
  - 2.4.2 Imaging . . . 27
  - 2.4.3 Second generation calibration (2GC) . . . 29
  - 2.4.4 Spectral line imaging . . . 29
- 2.5 Ancillary data . . . 30
  - 2.5.1 MGCLS continuum . . . 30
  - 2.5.2 The Dark Energy Survey . . . 30
  - 2.5.3 The Wide-field Infrared Survey Explorer . . . 30

3 Source finding **33**
3.1 Source finding with SoFiA 2 . . . 33
3.1.1 Source finding algorithm selection . . . 33
3.1.2 Strategy and implementation specifics . . . 34
Preconditioning and smoothing . . . 34
Smoothing . . . 35
Explanation of the flux threshold . . . 35
Linking, reliability, and mask dilation . . . 36

4 Results **38**
4.1 H I cubes . . . 38
4.2 Group membership classification . . . 39
4.3 Individual galaxy properties . . . 46
4.3.1 H I properties . . . 46
4.3.2 Stellar mass and SFR . . . 46

5 Discussion **55**
5.1 Scaling relations . . . 55
5.2 Individual galaxy analysis . . . 59
5.3 Group properties . . . 62
5.4 Classification of group structure . . . 62
5.5 MeerKAT serendipitous discoveries at $z \sim 0.04$ . . . 63

6 Conclusion **64**

A ROBUST comparison **65**

B H I spectra **71**

Bibliography **72**

List of Figures

1.1 Internal feedback mechanisms effect on galaxy luminosity function . . 3
1.2 Morphology-density relation 4
1.3 Star formation main sequence 5
1.4 Large scale structure of the universe 7
1.5 Galaxy distribution with all galaxies included. 9
1.6 Galaxy distribution for different forms of LSS. 11
1.7 IllustrisTNG simulation image of LSS 12
1.8 M81 H I triplet interaction 13
1.9 H I mass function 14
1.10 Schematic of various baryonic components within a typical disk-like galaxy 16
1.11 Various baryonic components and quantities as a function of redshift . 17
1.12 Model of star formation cosmic history 18
1.13 H I mass as a function of stellar mass 18

2.1 Two element interferometer 21
2.2 Antenna locations for inner core of MeerKAT 23
2.3 Antenna locations for all MeerKAT dishes 24
2.4 MeerKAT (u, v) coverage of observation of A3365 25
2.5 MGCLS 1.28 GHz continuum map 31

4.1 Channel map of Cube 1 39
4.2 Pre-classification moment 0 map 40
4.3 MCMC fit on galaxy velocity distribution 42
4.4 Galaxy group spatial location scatter plot 42
4.5 Moment 0 map of the group galaxies 43
4.6 Moment 1 map of the group galaxies 44
4.7 DES map with HI contours overlaid 45
4.8 Multiwavelength depiction of group galaxy members (1) 49
4.9 Multiwavelength depiction of group galaxy members (2) 50
4.10 Multiwavelength depiction of group galaxy members (3) 51
4.11 Multiwavelength depiction of group galaxy members (4) 52
4.12 Multiwavelength depiction of group galaxy members (5) 53

5.1 H I mass distribution 55
5.2 H I mass comparison between cubes 56
5.3 H I diameter as a function of H I mass 57
5.4 H I mass as a function of stellar mass 58
5.5 Star formation rate as a function of stellar mass 58
5.6 Gas-to-stars ratio in relation to spatial location 59

A.1 H I cube ROBUST comparison (1) 66
A.2 H I cube ROBUST comparison (2) 67

A.3 H I cube ROBUST comparison (2) 68
A.4 H I cube ROBUST comparison (3) 69
A.5 H I cube ROBUST comparison (4) 70

B.1 ROBUST 2 H I spectra of group galaxies 71

List of Tables

4.1 H I cube comparison 39
4.2 H I catalogue of group galaxies 54

5.1 Individual galaxy properties 60

List of Abbreviations

1GC	First **G**eneration **C**alibration
2GC	Second **G**eneration **C**alibration
2MASS	Two **M**icron **A**ll **S**ky **S**urvey
AGN	**A**ctive **G**alactic **N**uclei
ASKAP	**A**ustrialian **SKA** **P**athfinder
CGM	**C**ircum-**G**alactic **M**edium
CHILES	**C**OSMOS **HI** **L**arge **E**xtragalactic **S**urvey
CMB	**C**osmic **M**icrowave **B**ackground
COBE	**Co**smic **B**ackground **E**xplorer
CWD	**C**osmic **W**eb **D**etachment
DECam	**D**ark **E**nergy **Cam**era
DES	**D**ark **E**nergy **S**urvey
DisPerSE	**Dis**crete **Per**sistent **S**tructure **E**xtractor
FWHM	**F**ull **W**idth **H**alf **M**aximum
EHT	**E**vent **H**orizon **T**elescope
GAMA	**G**alaxy **A**nd **M**ass **A**ssembly
HI	Neutral **H**ydrogen
H_2	Molecular **H**ydrogen
HIMF	**HI** **M**ass **F**unction
HIPASS	**HI** **P**arkes **A**ll-**S**ky **S**urvey
ICM	**I**ntra-**C**luster **M**edium
IDIA	Inter-university **I**nstitute for **D**ata **I**ntensive **A**stronomy
IGM	**I**nter **G**alactic **M**edium
IG_rM	**I**ntra-**G**roup **M**edium
IRAS	**I**nfra**r**ed **A**stronomical **S**atellite
KINGFISH	**K**ey **I**nsights on **N**earby **G**alaxies: a **F**ar-**I**nfrared **S**urvey with **H**erchel
LADUMA	**L**ooking **A**t the **D**istant **U**niverse with the **M**eerKAT **A**rray
ΛCDM	**L**ambda **C**old **D**ark **M**atter
LF	**L**uminosity **F**unction
LNA	**L**ow **N**oise **A**mplifier
LSS	**L**arge-**S**cale **S**tructure
MCMC	**M**arkov **C**hain **M**onte **C**arlo
MGCLS	**M**eerKAT **G**alaxy **C**luster **L**egacy **S**urvey
MIGHTEE	**M**eerKAT **I**nternational **G**iga-**H**ertz **T**iered **E**xtragalactic **E**xploration
MS	**M**easurement **S**et
NIR	**N**ear **I**nfra**r**ed
PSF	**P**oint **S**pread **F**unction
RFI	**R**adio **F**requency **I**nterference
RGB	**R**ed **G**reen **B**lue
RMS	**R**oot **M**ean **S**quare
S+C	**S**mooth and **C**lip
SARAO	**S**outh **A**frican **R**adio **A**stronomy **O**bservatory

SDSS	**S**loan **D**igital **S**ky **S**urvey
SFMS	**S**tar **F**ormation **M**ain **S**equence
SFR	**S**tar **F**ormation **R**ate
SIRTF	**S**pace **I**nfra**r**ed **T**elescope **F**acility
SKA	**S**quare **K**ilometer **A**rray
SN	**S**uper**N**ovae
SNR	**S**ignal-to-**N**oise **R**atio
SoFiA	**So**urce **Fi**nding **A**pplication
sSFR	**s**pecific **S**tar **F**ormation **R**ate
SSRS	**S**outhern **S**ky **R**edshift **S**urvey
THINGS	**T**he **HI** **N**earby **G**alaxy **S**urvey
WALLABY	**W**ide-field **A**SKAP **L**-band **L**egacy **A**ll-sky **B**lind **S**urvey
WISE	**W**ide-field **I**nfrared **S**urvey **E**xplorer
WMAP	**W**ilkinson **M**icrowave **A**nisotropy **P**robe

I dedicate this thesis to my late father, Dennis Graham Lawrie, who passed on the 10th June 2021. Not a day passes by without me thinking about you. For all the love and support I have received in my life, I thank you. None of this would have been possible if it was not for you, Dad.

Chapter 1

Introduction

This chapter is structured as follows: Section 1.1 introduces the reader to the concept of galaxy evolution through giving an overview of galaxy formation, feedback mechanisms, environmental effects, and star formation. Section 1.2 describes the four primary components of the large-scale structure of the universe (filaments, clusters, groups, and voids) as well as introducing tendrils. In Section 1.3 we explore how H I can be used to better our understanding of galaxy evolution. A thesis outline is given in Section 1.4, summarising the work done in this thesis and briefly describing each chapter.

1.1 Galaxy evolution

1.1.1 Galaxy formation

Galaxy evolution and cosmology are intertwined since galaxy observations span cosmological time and spatial scales. Most modern cosmologies assume that the universe consists of three components: baryonic matter, which includes electrons, protons, and neutrons and makes up the visible universe; dark matter, which does not interact with the electromagnetic force but does interact with gravitational force and so evidence thereof has been inferred from observations of galaxy rotation curves, velocity dispersions, and gravitational lensing; and dark energy, of which the existence is also inferred by using tools such as observations of supernovae (SN) and the cosmic microwave background (CMB). Supernovae observations give independent distance measures which become more apparently distant with an increase in distance, this is used to infer the cosmological parameters. The latter two components are still poorly understood as the exact nature of dark matter and dark energy still eludes us. In the currently prevailing cosmology of Lambda cold dark matter (ΛCDM) the ratios are as follows: $\Omega_\Lambda = 0.6911$, $\Omega_m = 0.3089$, $\Omega_b = 0.0486$, and $\Omega_c = 0.2589$ (Planck Collaboration et al., 2016). Where the parameters represent the densities of the dark energy, matter, baryonic matter, and dark matter respectively.

Gravitational instabilities are thought to be a key starting point in the formation of galaxies. The term gravitational instabilities describes the situation where, in the early universe, small matter overdensities would attract nearby matter more so than the average to low matter density regions and so would become more over-dense. Similarly low density regions would not have sufficient attraction of surroundings when compared to the average density regions and so would become progressively under-dense. The expansion of the universe slows accretion onto these perturbations to where the density growth is described by a power law (Jeans, 1902). These perturbations grow in size as accretion occurs in the early universe, in the linear

regime where dark matter can be treated as a pressureless fluid. The shift to the non-linear regime signifies the point at which a perturbation has achieved a significant overdensity and starts to succumb to gravitational collapse, in this case the linear and pressureless fluid approximations can no longer be used and the full Newtonian theory of gravity needs to be applied. The result of this collapse depends on the matter composition of the perturbation and plays an important role in the formation of galaxies. The first possible outcome of this collapse is a dark matter halo, this occurs when the perturbation consists of dark matter, i.e. collision-less matter. In this case the perturbation will collapse without any shocks into a quasi-static equilibrium state in a process known as violent relaxation. In the event that the perturbation consists of baryonic matter, the collapse will result in shock heating, and if the radiative cooling is too slow, or inefficient, the matter will collapse into a hydrostatic equilibrium between gravitation collapse and radiative pressure. The ΛCDM cosmology stipulates that the universe, and so too the perturbations, consist of part baryonic and part dark matter (and part dark energy), thus the collapse results in baryonic matter in hydrostatic equilibrium within a dark matter halo (in the event that radiative cooling is inefficient). This baryonic proto-galaxy in the potential of a dark matter halo then forms the basis for galaxy formation (Mo, van den Bosch, and White, 2010).

Galaxies are generally classified into two types: early-type and late-type. Early-type galaxies are older, massive, elliptical galaxies where often star formation has quenched and the stellar population is more red than in late-type galaxies. A red stellar population refers to stars that emit red light and are older, dimmer, and much cooler at 3000 K than their blue counterparts which are young bright stars that have temperatures of up to 50 000 K. Additionally observations have found early-type galaxies to be considerably more gas deficient. Late-type galaxies are younger, less massive, disk galaxies. Late-type galaxies are found to be much more gas rich on average and thus have higher star formation activity, this causes late-type galaxies to have blue stellar populations. The timing of star formation in relation to the collapse of the baryonic gas cloud is thought to play a role in the type of galaxy that forms from the collapse (Eggen, Lynden-Bell, and Sandage, 1962; Larson, 1974). If star formation occurs during the collapse, the stars begin to exhibit random motion as is characteristic of an early-type elliptical galaxy. On the contrary, when the cloud remains gaseous during the collapse, shocks effectively dissipate the gravitational energy resulting in a shrinking of the cloud to the point where it is supported by angular momentum, this manifests itself in the disk-like structure.

It has been shown in numerical simulations that, alternatively, elliptical galaxies could form from mergers of disk galaxies in a hierarchical manner (Steinmetz, 1999, and references therein). More recently this theory was further reinforced with modern semi-analytic and hydrodynamical models as shown by Somerville and Davé (2015).

1.1.2 Internal feedback mechanisms

The study of feedback processes first emerged when astronomers predicted (using CDM models) that the majority of baryonic matter cools to form cold gas, then cools further to form stars. This contradicted the observational results heavily, as it was clear that only a small percentage of all baryonic matter took the form of cold gas

and stars. This raised the question: are the baryons being reheated in some manner? It is now understood that there exists an intricate internal feedback cycle between supernovae, active galactic nuclei (AGN), and star formation within galaxies (Cortese, Catinella, and Smith, 2021). Supernovae occur when sufficiently massive stars go through their final evolutionary phase, undergoing gravitational collapse and resulting in a neutron star, black hole, or being destroyed entirely based on the progenitor mass. The explosion results in shock waves that reheat cool gas and can push star forming gas out of the galaxy, this decreases star formation significantly (Larson, 1974). Similarly, AGN produce powerful jets that dissipate large amounts of energy, reheating cool gas and removing star forming fuel. These mechanisms are self regulating to a certain extent, for example when supernovae reheat cool gas and prohibit star formation, this leads to lower stellar population and less supernovae and thus allowing gas to cool once more. The contribution of the various feedback mechanisms are dependent on the mass of the galaxy in question. For low mass galaxies SN provide an accepted solution for gas disruption, while for massive galaxies SN are often inefficient and AGN are generally accepted as the dominant internal feedback mechanism (Silk and Mamon, 2012). Although there has been much recent progress in understanding internal feedback mechanisms, much work is still needed to truly comprehend these feedback mechanisms which are clearly fundamentals in galaxy evolution. This is illustrated in Figure 1.1.

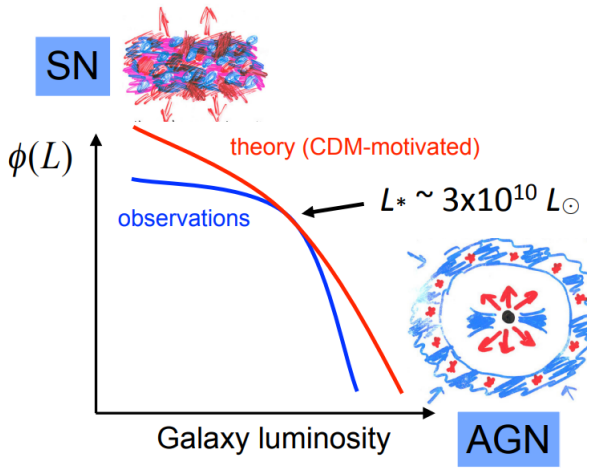


FIGURE 1.1: The role that internal feedback mechanisms play in modifying the galaxy luminosity function. Figure credit: Silk and Mamon, 2012.

1.1.3 Environmental effects on galaxies

Galaxy environment has been shown to have a major impact on factors of galaxy evolution such as color, morphology, and star formation. For instance, the number of late-type blue galaxies residing within a cluster increases as a function of redshift (Butcher and Oemler, 1978a). This has been confirmed by subsequent spectroscopic studies such as Dressler and Gunn, 1982, that found the blue galaxies in question were in fact cluster members and not line-of-sight interlopers. Additionally Dressler (1980) famously found the correlation between morphology and local density within low redshift clusters, known as the morphology-density relation (which is claimed to hold even in non-cluster environments (Geller and Beers, 1982)) see Figure 1.2. Interestingly, in later work Dressler investigates this correlation at higher redshift

($z \sim 0.5$) and find that it holds for regular, highly concentrated clusters, however the correlation is absent in irregular clusters. This could be interpreted as the morphological separation being a hierarchical process that affects high density groups of galaxies before affecting lower density groups (Dressler et al., 1997).

Simulations again provide us with a tool to confirm theories that originate from observations. Somerville and Davé (2015) illuminates the convergence of various models and methods at correctly predicting a set of core physical processes that include but are not limited to: suppression of star formation within galaxies by supermassive black hole feedback, galaxy evolution through hierarchical merging accompanied by environmental effects, and the influence of stellar winds on galaxy evolution. As computational limitations are reduced with modern technology advancements, simulations will play an increasingly important role in linking galaxy evolution on different scales and probing the environmental effects that contribute at these scales.

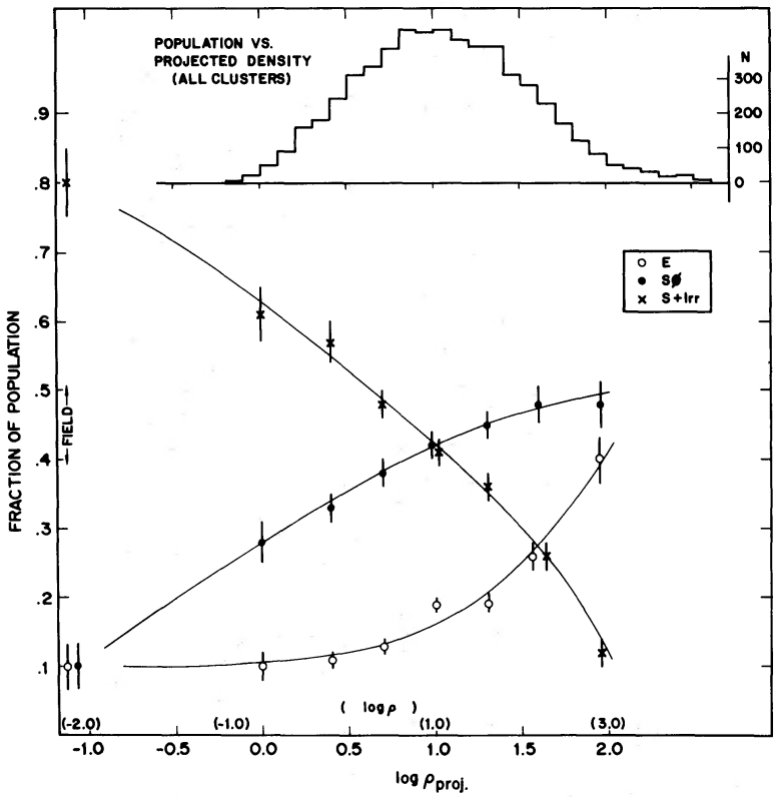


FIGURE 1.2: Fraction of galaxies present in clusters versus log of projected density in Mpc^{-2} for elliptical, lenticular, and spiral or irregular galaxies. The number distribution of the galaxies over the projected density bins is shown in the histogram. Figure credit: Dressler, 1980.

1.1.4 The star formation main sequence

The star formation main sequence (SFMS), or galaxy main sequence is the term used to describe the relationship between stellar mass and star formation rate (SFR). There exists a tight correlation between the stellar mass and the star formation rate of normal star forming galaxies (Daddi et al., 2007; Elbaz et al., 2007). The galaxies below

the main sequence are normally quenched, which means star formation has ceased. The mechanisms behind quenching within galaxies are a topic of ongoing study with mechanisms such as starvation (halted cold gas accretion), tidal stripping (removal of cold gas by tidal interactions), and AGN or supernovae (removal/heating of cold gas) being promising solutions (Cortese, Catinella, and Smith, 2021, and references therein). On the other end, galaxies that are above the main sequence with unusually high star formation rate with respect to their stellar mass are often starburst galaxies. Generally the rapid star formation in starburst galaxies is associated with dust that obscures optical wavelengths. However, young blue stars that form have their radiation absorbed and re-emitted by the dust in the far-infrared wavelengths. Starburst galaxies are typically defined as galaxies that go though a period of extremely high star formation after a disruptive interaction such as a gas-rich merger that would causes star forming gas to compact at higher than normal rates (Mo, van den Bosch, and White, 2010). Variations within the main sequence could possibly be attributed to the internal feedback cycle discussed earlier, with AGN and supernovae periodically altering the gas content of the galaxies (Tacconi et al., 2013). Finally the redshift of a galaxy also plays a role in where it fits into the star formation main sequence, with higher redshift galaxies typically having higher star formation rates out to $z = 2.5$ as expected from the Butcher-Oemler effect (Whitaker et al., 2012). See Figure 1.3 for an illustration of the star formation main sequence.

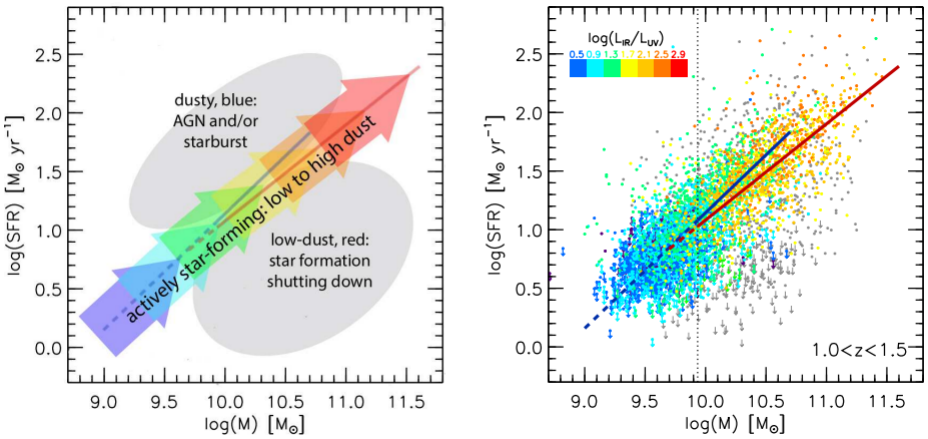


FIGURE 1.3: Left: A cartoon schematic showing galaxy content, SFR, and type on the SFMS. Right: Observed view of how the SFMS plane is populated with galaxies. 54 per cent of galaxies reside on the star formation main sequence. The amount of dust increases (higher L_{IR}/L_{UV} ratios) as one moves up the SFMS. The shallower slope indicates a lower specific star formation rate (sSFR) at the high end of the stellar mass. 7 per cent of galaxies have blue colors and high dust, putting them in the upper grey envelope. 11 per cent of galaxies have low dust and red colors and fall into the lower grey envelope. Figure credit: Whitaker et al., 2012

1.2 Large-scale structure

1.2.1 Overview

The large-scale structure (LSS) of the universe consists of filaments that interconnect to form the cosmic web as well as voids, see Figure 1.4 for a depiction of the large

scale structure of the universe observed by Sloan Digital Sky Survey (SDSS[1]). The term LSS is used to describe Mpc scale structure including filaments and clusters as well as less extensive structure such as groups. Classification methods differ in the way that they define filaments, clusters, groups, and voids using various different local density values to classify LSS. This creates a situation where there is an overlap in definitions for different methods, see Libeskind et al. (2018) for a review and comparison of various methods. The current LSS of the universe is thought to have initially formed from overdensities in the early universe (Bond, Kofman, and Pogosyan, 1996). The prevailing theory that provides the needed initial conditions required for overdensities and underdensities to form is that of cosmic inflation, wherein it is proposed that the universe was supercooled through exponential growth resulting in huge expansion (Guth, 1981). Inflation addresses two problems: The horizon problem and the flatness problem. The horizon problem arises because we observe the CMB at the same temperature at all locations in the universe, however there are parts of the universe that are too far for a signal to travel between them for thermal equilibrium to occur without the inclusion of inflation theory. The flatness problem refers to the seemingly improbable observation that the curvature of the universe is flat. The curvature of the universe is calculated to be flat using the CMB, despite the origins of the universe being governed by quantum fluctuations. Inflation accounts for this since it is capable of changing any initial shape of the universe to a flat shape through rapid expansion. In addition to this, inflation is capable of explaining the amplification of quantum fluctuations in the early universe leading to the required perturbations that eventually form the cosmic web. Observational evidence for these perturbations exists in the form of the CMB. The CMB radiation is captured during the epoch of recombination at $z \sim 1100$, where temperatures were cold enough for the universe to be opaque since opacity $<<1$ at this time. Photons were then free to propagate until present time where they are detected at 2.725 K, downshifted from 3000 K due to the expansion of the universe. The Cosmic Background Explorer (COBE) was the first to detect anisotropies in the CMB (Efstathiou, Bond, and White, 1992), thereafter Wilkinson Microwave Anisotropy Probe (WMAP)(Spergel et al., 2003), and then Planck (Planck Collaboration et al., 2016).

1.2.2 Clusters

Galaxy clusters are large groups of gravitationally bound galaxies. Clusters contain up to thousands of galaxies and have a wide range of virial radii and virial masses with typical radii being $\sim 2\,\mathrm{Mpc}$ and virial masses being between $10^{14}\,\mathrm{M}_\odot$ and $10^{15}\,\mathrm{M}_\odot$, (Girardi et al., 1998, and references therein). The origin of these massive galaxy clusters is thought to be the collapse of the largest of the overdensities in the early universe (Kravtsov and Borgani, 2012). Clusters are predominantly located at filament intersections within the cosmic web, referred to as nodes, due to the prevalence of large overdensities at these locations in the early universe. Historically galaxy clusters have been classified according to a number of different methodologies (Bautz and Morgan, 1970; Abell, 1958; Abell, 1965).

While the general consensus is that the majority of the mass of a cluster comes from the dark matter, having a ~ 80 per cent contribution, the majority of the baryonic mass within a cluster is due to the ionised intracluster medium (ICM). The

[1] https://www.sdss4.org/science/orangepie/

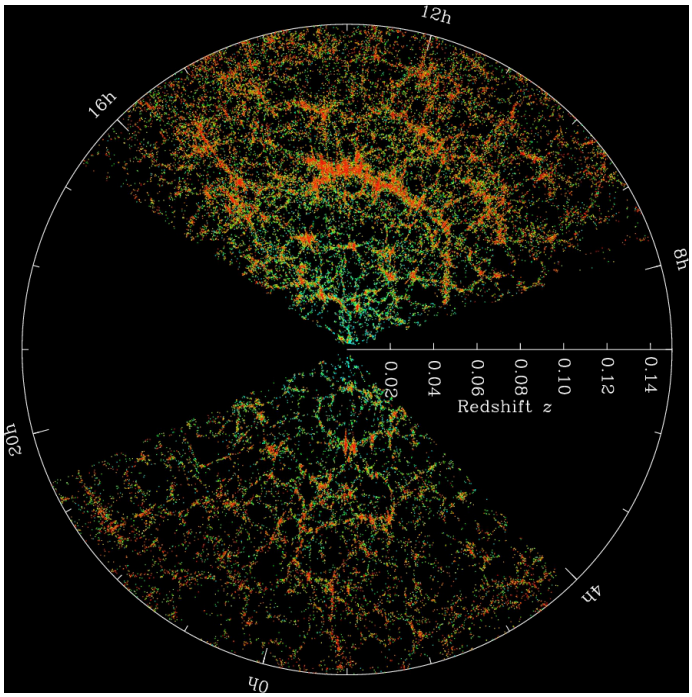


FIGURE 1.4: Large scale structure map of the universe where every dot is a galaxy and the color is the g-r colour of the galaxy. Figure credit: M. Blanton and SDSS.

ICM is a hot gas present in galaxy clusters which is mainly detected through thermal bremsstrahlung. The ICM, which consists mainly of ionised hydrogen and helium at temperatures up to 10^8 K or 10 keV (Mohr, Mathiesen, and Evrard, 1999), is not associated with the cluster galaxies, however very tight correlations exist between ICM gas and stellar properties. One such example is the mass relation, where $M_*/M_{ICM} = 0.2$ for small clusters (virial mass $\sim 10^{13}\,M_\odot$) and $M_*/M_{ICM} = 0.05$ for the largest of clusters (virial mass $\sim 10^{15}\,M_\odot$) (Kravtsov and Borgani, 2012, and references therein), where M_* is the stellar mass of the cluster and M_{ICM} is the mass of the ICM gas.

Butcher and Oemler (1978b) found that the percentage of spiral galaxies within a cluster was inversely proportional to the central concentration of the cluster. They used a central concentration parameter to compare the clusters instead of a regularity parameter due to the simplicity thereof. It was found that in their sample of 21 clusters at low redshift ($z < 0.17$) only clusters with low central concentration had a large percentage of spiral galaxies. When considering the earlier study, (Butcher and Oemler, 1978a), we see that at intermediate redshift ($0.39 < z < 0.46$) there are significantly higher percentages of spiral galaxies overall, even for clusters with high central concentrations. This is known as the Butcher-Oemler effect and is indicative of a potential surge in star formation rate corresponding to that period in time. A similar result to the morphology-concentration relationship found by Butcher and Oemler (1978a) was found by Dressler (1980), where it was found that the elliptical population would increase, and thus the spiral population decrease, with increasing local density (Dressler, 1980). These results highlight the influence that environmental effects have on galaxy morphology.

Galaxy clusters are an important bridge between theoretical cosmology and observational astronomy, making them crucial to the necessarily coupled understanding of formation of large-scale structure and galaxy evolution.

1.2.3 Filaments

Filaments are the largest known structures in the universe. They are high density environments where clusters and groups of galaxies are preferentially found, particularly at nodes which form at the intersections of multiple filaments. These structures form on the filamentary dark matter that make up the cosmic web through gravitational attraction of baryonic matter to the dark matter potential wells. Generally, filaments span up to $\sim 80\,h^{-1}$ Mpc and interconnect to form the filament-void network, for example Bharadwaj, Bhavsar, and Sheth (2004). Individual filaments have been detected at larger sizes, however these are not statistically significant, see Horváth, Hakkila, and Bagoly (2014) and Deng et al. (2006) for examples of these large filaments referred to as "walls". Filaments have a large impact on galaxy evolution as they are suspected to play a role in replenishment of star forming gas through streams of cold gas accretion, see Kleiner et al. (2017). Aragon Calvo, Neyrinck, and Silk (2019) describes a model of Cosmic Web Detachment (CWD) whereby galaxies are quenched. The effect that the distance to the nearest neighboring filament has on galaxy properties such as angular moment and H I content is currently a topic up for debate, as numerous studies within the field contradict one another such as Kleiner et al. (2017) and Crone Odekon et al. (2018). In these studies Kleiner et al. (2017) finds decreasing H I deficiency with decreasing distance, while Crone Odekon et al. (2018) finds the opposite relationship. Spin alignment to the nearest filament is found to be preferentially aligned to the filament, increasingly so for galaxies with low gas fraction ($M_{\rm H\,I}/M_*$) (Tudorache et al., 2022).

1.2.4 Groups

Galaxy groups are the smaller counterparts to galaxy clusters, albeit having distinct differences. Galaxy groups account for more than half of galaxies in the local universe, typically consist of as few as 4 or as many as 20 or more galaxies, and have virial radii of $R_{200} \sim 400\,\mathrm{kpc}$ and virial masses of $\sim M_{200} = 10^{13}\,\mathrm{M}_\odot$ (Feldmann, Carollo, and Mayer, 2011). R_{200} is defined as the virial radius enclosing a mean matter density of $200/\Omega_m$ times the mean desity of the universe, and M_{200} the mass enclosed within that radius. The first significantly large sample of galaxy groups was presented in (Huchra and Geller, 1982). One distinguishing property is the temperature of the intra-group medium (IG$_{\rm r}$M) when compared to the ICM. While the IG$_{\rm r}$M still emits x-rays through thermal bremsstrahlung, it is substantially cooler at $0.3 - 2\,\mathrm{keV}$ (Mulchaey, 2000). In addition to the temperature difference, the electron density of order $10^{-6}\,\mathrm{cm}^{-3}$ for $10^{12.5} - 10^{13}\,\mathrm{M}_\odot$ halos and $\sim 6 \times 10^{-5}\,\mathrm{cm}^{-3}$ for halos $> 10^{14}\,\mathrm{M}_\odot$ (Robson and Davé, 2020), indicating that higher mass halos, such as clusters, have higher electron density in the ICM than the lower mass halos such as groups have in the IG$_{\rm r}$M. Finally, the large virial mass difference leads to a significant difference in velocity dispersion with groups generally having velocity dispersions of $< 500\,\mathrm{km\,s}^{-1}$ (Muñoz et al., 2013), which is marginally higher than the velocity dispersion of individual massive galaxies (Mulchaey, 2000). The density difference creates the expectation that medium driven environmental effects, such as ram pressure stripping (Gunn and Gott, 1972), are not as important in a lower electron density environments, such as the IG$_{\rm r}$M, as it is in the high electron density ICM

present in groups. However the velocity dispersion of a group being comparable to the individual galaxy velocity dispersion points towards galaxy-galaxy interactions being more important in a group environment (Mulchaey, 2000).

1.2.5 Tendrils

Tendrils are elongated low density LSS first discovered by Alpaslan et al. (2014) in data from the Galaxy and Mass Assembly (GAMA) survey. Alpaslan et al. (2014) describes the structure type as consisting of an average of ~ 6 galaxies and spanning an average of $10\,h^{-1}$ Mpc. Typically tendrils are found at the edges of filaments, being rooted in the filament and terminating in a void. In other situations tendrils are found spanning between, and thus connecting, two filaments. See Figure 1.6 for a comparison between different forms of the LSS, contrasting the differences in location, spatial extent, and density (Crone Odekon et al., 2018). Figure 1.5 shows a combination of all the galaxies in Figure 1.6, thus presenting all galaxies in the sample (Crone Odekon et al., 2018). See Crone Odekon et al. (2018) for information on how galaxy environments were classified. The local density of tendrils fall between that of voids and filaments, with local density systematically increasing from voids to tendrils and then filaments and groups, groups being the most locally dense (Crone Odekon et al., 2018). Interestingly galaxies in tendrils are found to be more H I gas rich than galaxies in the surrounding void. In addition to this tendril galaxies are no more red than void galaxies despite being more massive (Crone Odekon et al., 2018). While study on tendrils is limited, the findings of these studies are significant. For instance, Alpaslan et al. (2014) points out that SDSS voids that overlap with GAMA regions contain many "tendril" galaxies. Environmental effects of tendrils could also be significant, such as the potential for tendrils to act as reservoirs to replenish star-forming gas of nearby galaxies through cold gas accretion, making them potential galaxy evolution drivers in lower density parts of the universe.

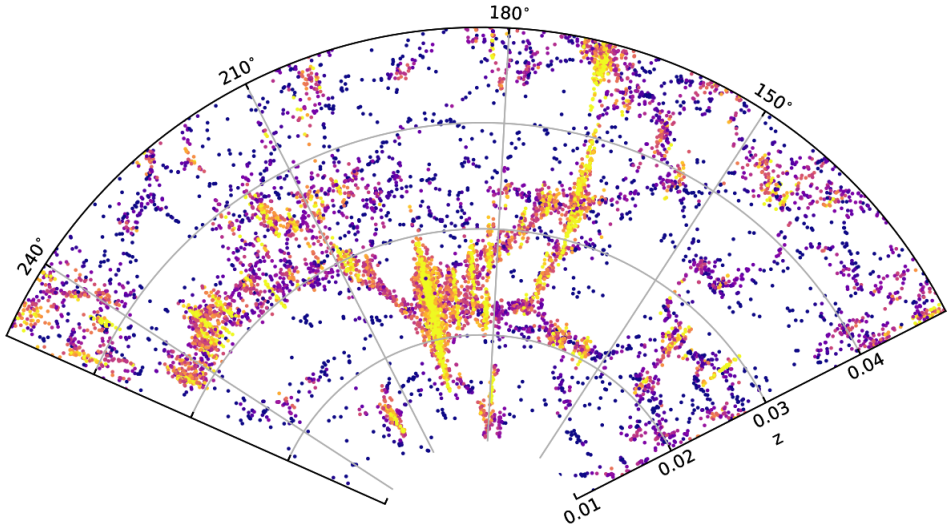


FIGURE 1.5: Distribution of galaxies with all galaxies included and color-coded by nearest neighbor density (Crone Odekon et al., 2018)

1.2.6 Voids

Voids are regions between the interconnecting filaments that make up the cosmic web. These regions have very low density have few or no detectable galaxies within them. Pan et al., 2012 studied the distribution of cosmic voids in the SDSS Data Release 7 and found the voids to be significantly underdense and have a median radius of $17\,h^{-1}$ Mpc. While having a notably lower density, voids are not completely devoid of galaxies as $\sim$ 7 per cent of galaxies in SDSS DR7 reside in voids (Pan et al., 2012). Pan et al. (2012) also compared these results to mock catalogues from ΛCMD simulations and found similar void population and sizes. Several void identification algorithms have been developed, one of which is the VOID FINDER algorithm that provides a way to objectively quantify voids (El-Ad and Piran, 1997). In testing VOID FINDER, El-Ad and Piran (1997) found that voids make up 50 per cent of the volume in both the Southern Sky Redshift Survey (SSRS) and in full-sky 1.2 Jy Infrared Astronomical Satellite (IRAS) survey. Similarly to filaments, the origin of voids is thought to be the same density fluctuations in the early universe where the under-densities formed the voids (Bond, Kofman, and Pogosyan, 1996). When compared to the relationship between filaments and the anisotropies in the CMB, voids instead correspond to the cold anisotropies present in the CMB (Granett, Neyrinck, and Szapudi, 2008).

To summarise the different forms of LSS that our cosmic web is comprised of (the main ones being filaments, clusters, groups, and voids), a image from the IllustrisTNG[2] simulation is show in Figure 1.7.

[2]https://www.tng-project.org

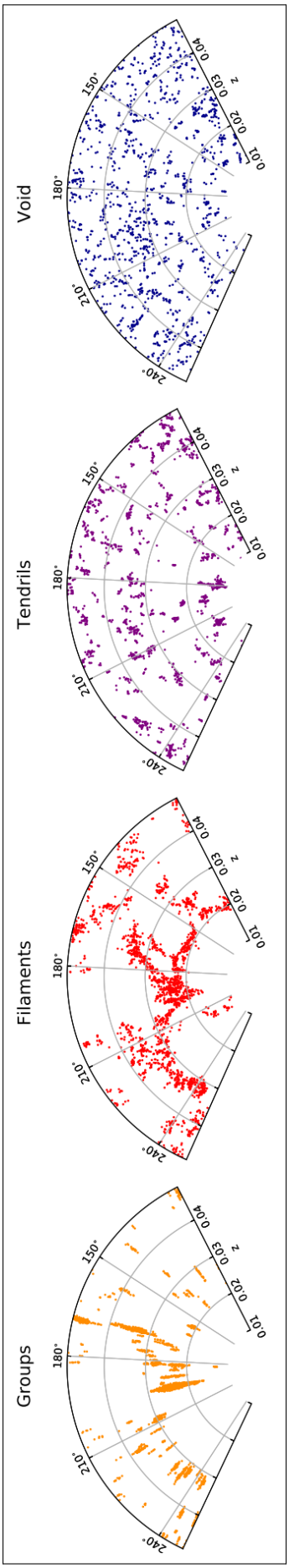


FIGURE 1.6: Distribution of galaxies according to different forms of LSS in right ascension and redshift of a slice in declination between 22 deg and 25 deg where each dot is a galaxy (Crone Odekon et al., 2018).

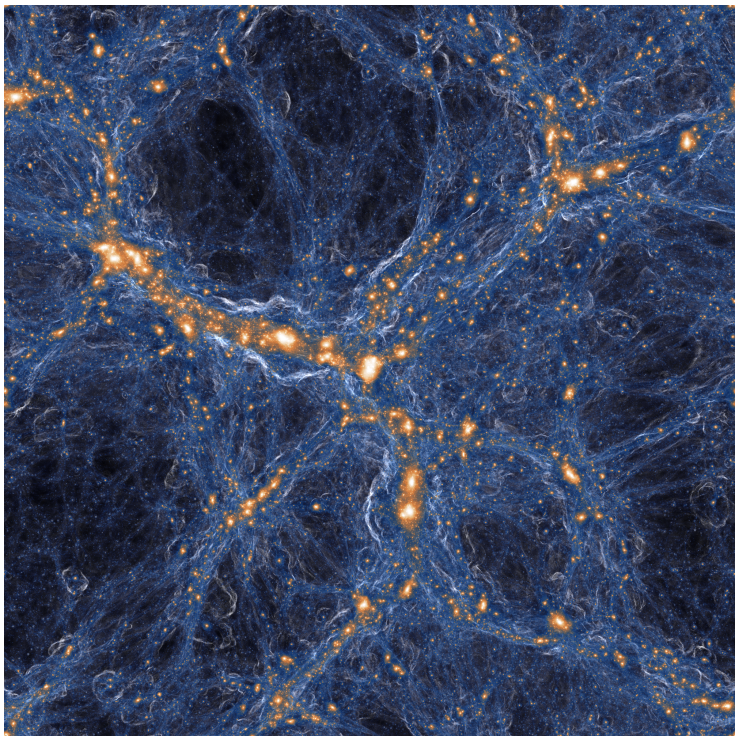


FIGURE 1.7: Composite image of the output of the IllustrisTNG cosmological shock finder with an overlay of a projection of the dark matter density. The orange and white colours show the gravitationally collapsed structure, while the blue colours indicate shock surfaces. Figure credit: IllustrisTNG.

1.3 Importance of H I

1.3.1 Overview of neutral hydrogen

Throughout this thesis H I and neutral hydrogen are used interchangeably and refer to atomic hydrogen in its ground state. In its neutral state, the hydrogen atom consists of one proton and one electron. This makes neutral hydrogen the lowest mass element, since lower mass elements formed first and more readily, this lead to hydrogen being the most abundant element in the universe. Together with helium, the second lowest mass element, neutral hydrogen makes up a significant fraction, approximately 99 per cent, of the baryonic content of the universe. Detection of neutral hydrogen comes from the notable 21 cm line. The 21 cm line corresponds to a frequency of 1420.405751768 MHz putting it in the radio regime of the electromagnetic spectrum, specifically in the L-band when observing sources at low redshift ($z < 0.5$). Different configurations of the atom result in different energy levels, i.e., while the spin of the electron is parallel with the proton the atom is in a slightly higher energy state, in the event that the spins of the proton and electron are anti-parallel the atom is in a slightly lower energy state. The transition from one state to another is referred to as a hyperfine transition and is accompanied by the emission of the 21 cm line if the transition is from parallel to anti-parallel. The transition itself is spontaneous but also highly forbidden with a occurrence rate of $2.9 \times 10^{-15}\,\mathrm{s}^{-1}$ analogous to about one transition from high energy state to low energy state every 10 million years (10 Myr), see Wiese and Fuhr (2009). Fortunately, the abundance

of H I counteracts the forbidden nature of the transition, allowing H I to be detected through the 21 cm line rather easily at low redshifts.

It is well known that the H I component of galaxies extends far further than the optical galaxy, see Broeils and Rhee (1997) for evidence thereof. Broeils and Rhee (1997) also investigates the correlations of the H I diameter and found that it does not depend on morphological type. They found the strongest correlator to be that of the one between H I mass and H I diameter (Broeils and Rhee, 1997). The H I component of galaxies is sensitive to environmental interactions both with other galaxies on long dynamical timescales, such as mergers, or with the medium through which it is moving (be that ICM or IG$_r$M) in the form of ram pressure stripping. The sensitivity of H I to these interactions is of particular importance in this work as it lets H I act as a dynamical tracer of these environmental effects that are vital in progressing our understanding of galaxy evolution. A renown example of how H I traces interactions is shown in Figure 1.8 (Yun, Ho, and Lo, 1994). The gas filaments connecting the galaxies seen in Figure 1.8 are not present in the optical map, highlighting the power of H I to probe galaxy interactions.

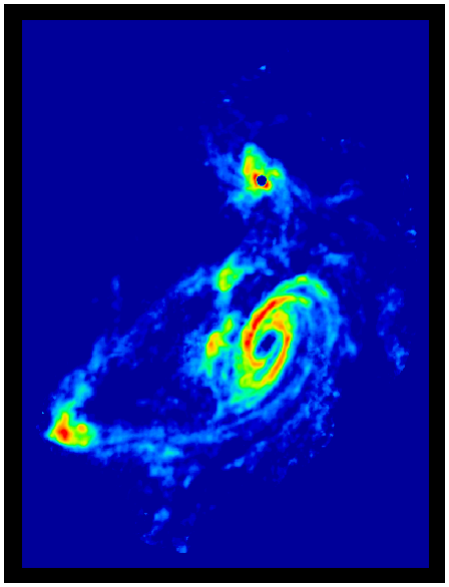


FIGURE 1.8: H I map of M82 (top), M81 (middle), and NGC3077 (bottom left) interacting (Yun, Ho, and Lo, 1994).

1.3.2 H I mass function

The luminosity function (LF) describes the number density of galaxies, or stars, as a function of luminosity. Unlike the LF which is well studied and understood, the H I mass function (HIMF) which is the radio analogue of this function, is less well understood. The H I function is useful for deriving the H I mass density of the universe. Since H I gas makes up a significant fraction of the baryonic matter of the universe, this H I mass density ($\Omega_{\mathrm{H\,I}}$) plays an important role in constraining the baryonic density within cosmological models (Zwaan et al., 2005).

Both the LF and the HIMF are described by a Schechter function, (Schechter, 1976). In the case of the HIMF, the function consists of a power-law at the low mass end

and a exponential at the high mass end with a "knee" mass, or a turnover mass, that separates the parts of the function. The HIMF is then given by the following,

$$\theta\left(\hat{M}_{\rm HI}\right) dM_{\rm HI} = \theta^* \hat{M}_{\rm HI}^{\alpha} e^{-\hat{M}_{\rm HI}} dM_{\rm HI} \tag{1.1}$$

$$\hat{M}_{\rm HI} = \frac{M_{\rm HI}}{M_{\rm HI}^*}, \tag{1.2}$$

where θ^* is the normalisation factor, α gives the slope of the power-law part, and $M_{\rm HI}{}^*$ is the turnover mass. The number density of galaxies above this mass drops exponentially, seen in Figure 1.9.

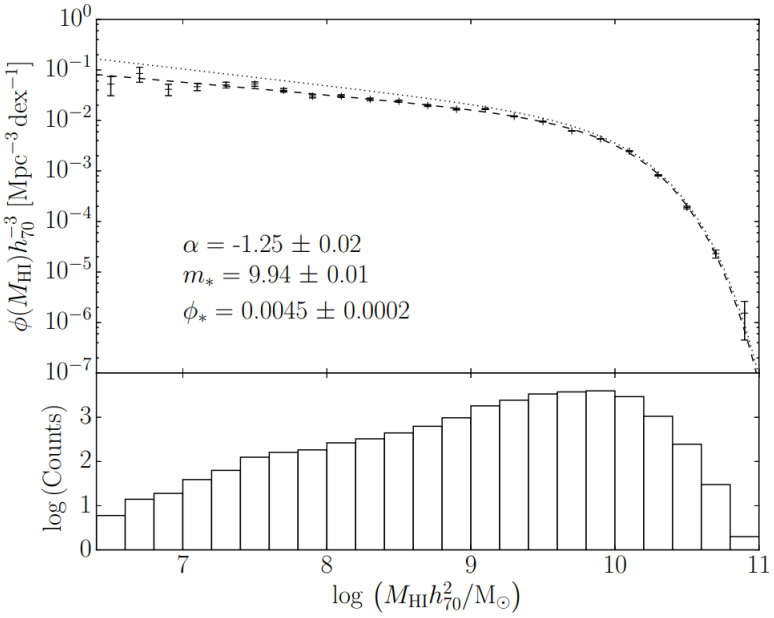


FIGURE 1.9: Figure of the ALFALFA 100 per cent HIMF directly reproduced from Jones et al. (2018). The histogram at the bottom shows the number distribution across the H I mass bins, while the points in the plot above give the calculated number abundances. The error bars are calculated from Poisson counting errors. The parameters given in the bottom left of the top plot are those for the Scheter function of the best fit to the data. The dotted line represents the ALFALFA 40 per cent best fit (Martin et al., 2010)

1.3.3 Large scale-structure effects on H I content

With the effect of local density on galaxy properties shown by the likes of Dressler (1980) and Butcher and Oemler (1978a), the next step is to investigate the effects of the galaxy position within the cosmic web. The distance from filamentary structure is predicted to have an effect on the neutral hydrogen gas content of nearby galaxies (Cortese, Catinella, and Smith, 2021, and references therein). It is argued that there is a relationship between the distance to the nearest filament and H I mass, see Crone Odekon et al. (2018), Kleiner et al. (2017), and Blue Bird et al. (2020). However there is little agreement, for instance Kleiner et al., 2017 finds galaxies become more H I deficient with increasing distance to filament for galaxies with stellar mass $< 10^{11}\,{\rm M}_\odot$, while Crone Odekon et al. (2018) find H I content increases with increasing distance

from the filament. Furthermore, there appears to be correlation between H I spin orientation and galaxy location with respect to the nearest filament shown in hydrodynamical simulations (Aragón-Calvo et al., 2007; Codis et al., 2012; Kraljic, Davé, and Pichon, 2020). Observational evidence is rather scarce, with Blue Bird et al. (2020) investigating the effect of distance to nearest neighbor filament with a sample of 10 galaxies from first epoch COSMOS H I Large Extragalactic Survey (CHILES) and finding that galaxies closer to filaments preferentially align with filament orientation. Thereafter as part of the MeerKAT International GigaHertz Tiered Extragalactic Exploration (MIGHTEE) survey, 77 H I selected galaxies were used with COSMOS and XMM-LSS fields galaxies to investigate the relationship between galaxy spin alignment and properties such as: distance to nearest filament, H I content, baryonic fraction, and gas fraction (Tudorache et al., 2022). This was done by using COSMOS and XMM-LSS fields galaxies in combination with The Discrete Persistent Structure Extractor (DisPerSE, Sousbie, 2011) to create a cosmic web skeleton. Tudorache et al. (2022) found similar results to Blue Bird et al. (2020), showing that decreasing distance to filament increases chance of galaxy alignment, but also finding that galaxy alignment is heavily dependant on the ratio of H I mass to stellar mass, with more H I poor galaxies being preferentially aligned. Despite recent progress, it is clear that more studies of the environmental effects of filaments need to be done in order to better understand the phenomenon, this is true of both individual studies of filaments in the low redshift universe as well as statistical investigations over larger cosmological volumes.

1.3.4 H I in relation to star formation

The primary fuel for star formation is molecular hydrogen (H_2) which forms gas clouds, condenses, collapses, and eventually forms stars as elements compress and combine into heavier elements. Walter et al. (2020) investigates and constrains the evolution with redshift of baryonic components of galaxies by using recent science regarding the evolution of molecular hydrogen with redshift together with previous constraints on H I. Figure 1.10 shows the ionised hydrogen infall from the circumgalactic medium (CGM) to the H I extent of the galaxy where it replenishes the H I reservoir as it cools. H I then enters the central disk (the stellar extent of the galaxy) where it forms molecular gas. This molecular gas then forms stars after cooling and condensing. The net outflow indicates all material that flows out of the galaxy into the CGM or the IGM. This outflow is thought to be due to various feedback effects and to be proportional to the stellar mass of the galaxy (Walter et al., 2020). Figure 1.11 presents us with a holistic picture of the star formation history by combining the well known Madau and Dickinson (2014) plots (top) with recent constraints on atomic and molecular hydrogen density evolution.

One expects H I to then be a tracer for star formation, however studies have found that H I and SFR are not strongly correlated on sub-kpc scales. Bigiel et al. (2008) used 18 galaxies from The H I Nearby Galaxy Survey (THINGS) to find that while H_2 is proportional to SFR, H I has no clear correlation to SFR in normal star forming galaxies. Despite the lack of direct correlation, H I gas acts as a reservoir for star forming fuel making it an important component and transitory phase of studying the star formation of galaxies. It is also important to note that more recent work has found that a a tight correlation between the gas and the SFR volume densities exist if one assumes that the gas disk is in hydrostatic equilibrium (Bacchini et al.,

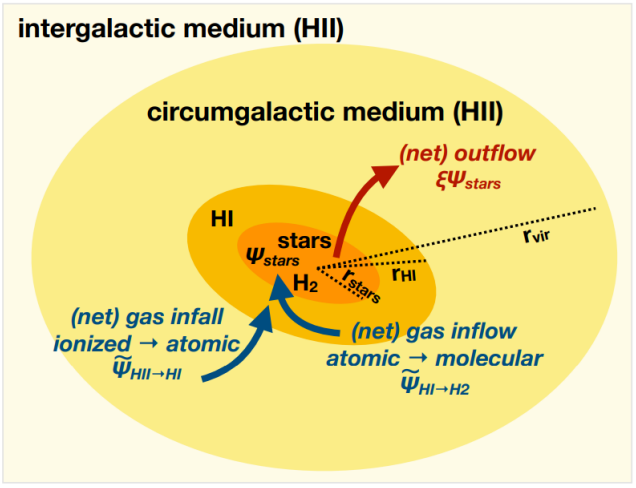


FIGURE 1.10: Schematic of a typical disk-like galaxy showing the IGM, CGM, H I extent, and stellar extent. The figure shows the infall of ionised gas into the H I extent of the galaxy, as well as the inflow of atomic hydrogen into the stellar extent of the galaxy with blue arrows. The red arrow indicates the outflow of various materials from the stellar extent to the CGM and IGM. Image credit: Walter et al. (2020).

2019). The link between H I and H_2 has been investigated by simulations such as (Obreschkow and Rawlings, 2009), who determined the following:

$$R_{\rm mol}^{\rm universe}(z) \approx 0.3(1+z)^{1.6}, \tag{1.3}$$

where $R_{\rm mol}^{\rm universe}(z) \equiv \frac{\Omega_{H_2}(z)}{\Omega_{\rm HI}(z)}$. Which reveals not only that H I and H_2 evolve differently with time, but also that $R_{\rm mol}^{\rm universe}(z)$ increases as a power-law with redshift. Galaxies at higher redshifts thus have higher $\Omega_{H_2}(z)$, reinforcing knowledge that at $\sim z = 2$ star formation peaks (Madau and Dickinson, 2014). See Figure 1.12 for a simple schematic overview of cosmic history of star formation.

We present Figure 1.13 to show the relationship between stellar mass and H I mass determined by Parkash et al. (2018). Parkash et al. (2018) uses the H I Parkes All-Sky Survey (HIPASS) to make up a sample of 3513 H I selected galaxies. Of the H I galaxies 2826 have good W1 and W2 Wide-field Infrared Survey Explorer band photometry, which is used to calculate the stellar mass as will be addressed in Section 4.3. Note that generally H I selected samples tend to overestimate the relation due to missing low H I mass galaxies.

1.4 Thesis outline

In this dissertation we report the serendipitous discovery of a gas-rich galaxy group with a filamentary-like Mpc-scale structure, in the foreground of Abell 3365 using MeerKAT. With H I being a useful tool for probing the effects of galactic environment

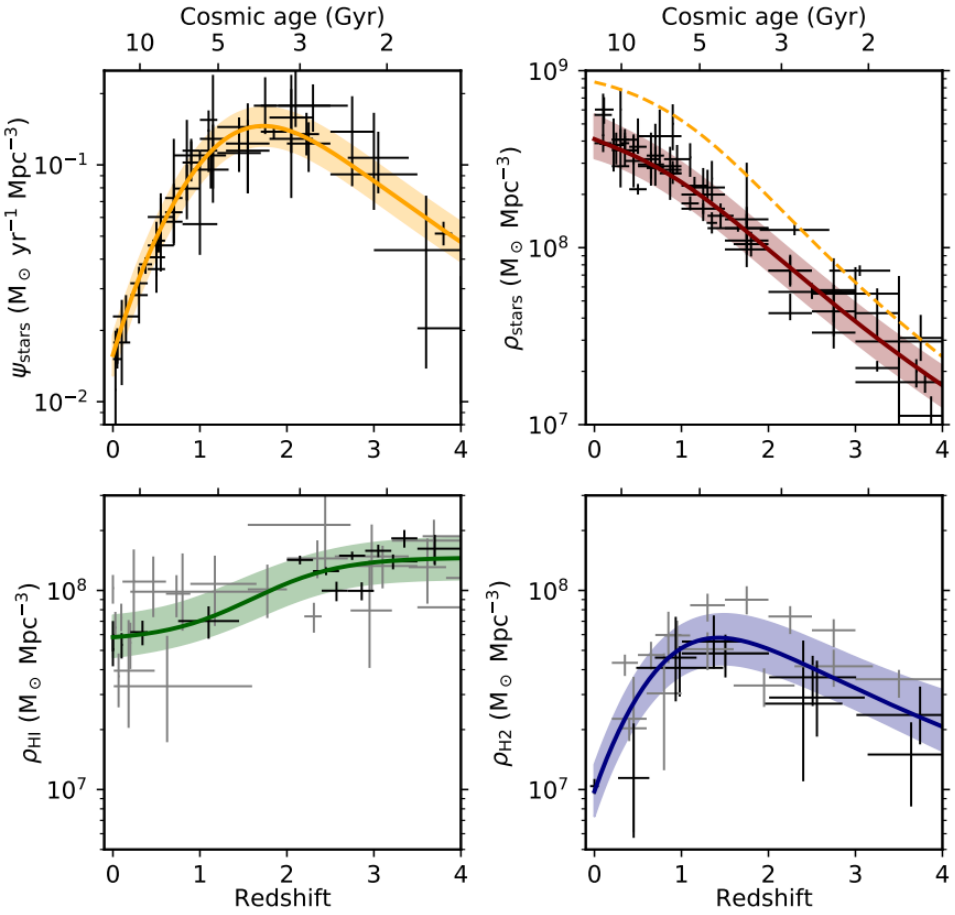


FIGURE 1.11: All solid lines are best-fits to the data and all shaded regions indicate the 1σ levels. Top left is the cosmic star formation rate density as a function of redshift and top right is the stellar mass density as a fucntion of redshift, both from Madau and Dickinson (2014). In the top left plot the difference between the orange dashed line (integration of the best-fit of the top left plot) and the solid red line is adressed in Madau and Dickinson (2014). Bottom left is H I density from Neeleman et al. (2016) with grey ($< 6\sigma$) and black ($> 6\sigma$) measurement points. Bottom right is molecular hydrogen density from Decarli et al. (2019) among other surveys with grey (dust continuum observations) and black (CO observations) measurement points. Image credit: Walter et al. (2020).

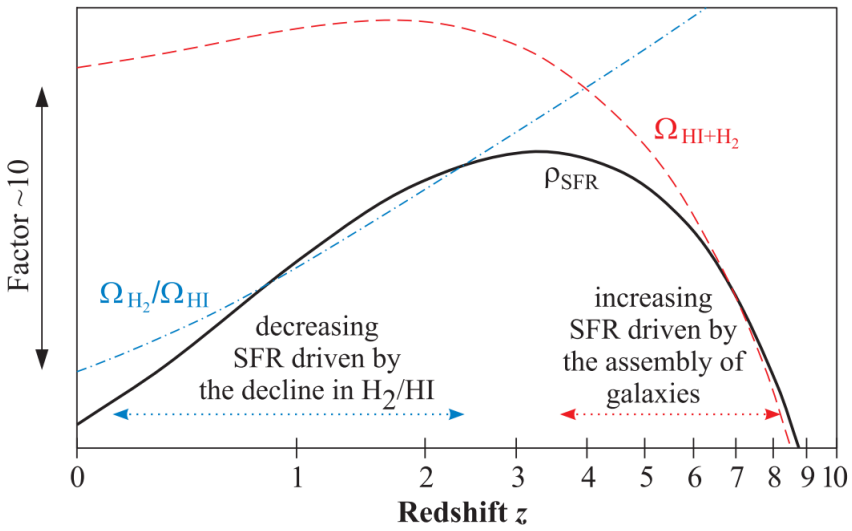


FIGURE 1.12: Simple schematic overview of cosmic history of star formation showing cosmological gas density ratio together with total cosmological gas density and star formation rate density as a function of redshift (Obreschkow and Rawlings, 2009).

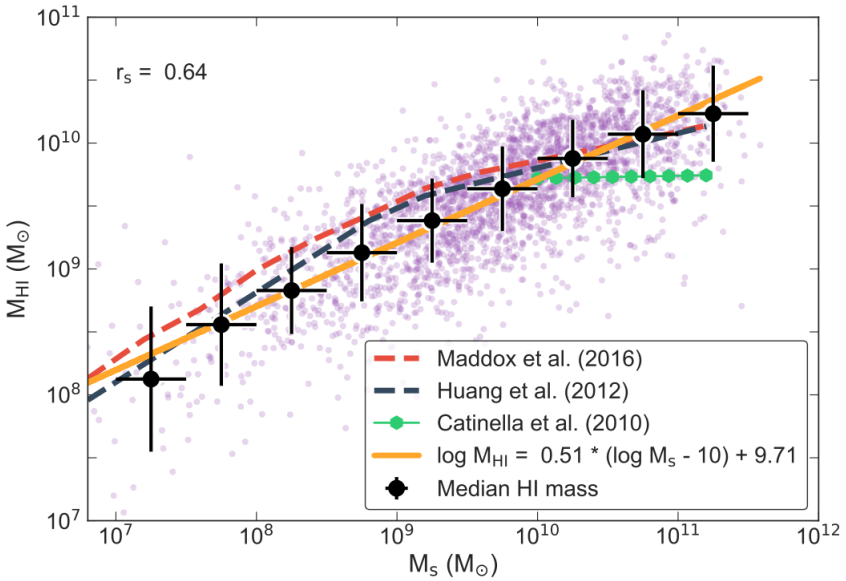


FIGURE 1.13: H I mass as a function of stellar mass for H I selected galaxies where the solid orange line is the relation determined by Parkash et al. (2018).

on galaxy evolution we use data from MeerKAT Galaxy Cluster Legacy Survey (MGCLS) to investigate H I properties of galaxies within the gas-rich group environment. A multiwavelength approach is taken to derive stellar mass and SFR with infrared imaging as well as bettering the understanding of morphology and interactions of individual galaxies using optical data.

Chapter 2 is an introduction to basic radio interferometry as well as the MeerKAT telescope itself. An overview of the observation, data set, and data reduction methodology is also described. Chapter 3 describes the source finding strategy using SoFiA. Chapter 4 includes the results, that being the discovery of a gas-rich galaxy group with a filamentary structure and the group membership algorithm implemented. We also derive the properties of the galaxies within the group using H I, radio continuum, infra-red, and optical data. Discussion with regards to the scaling relations, the group properties, and the classification of the group structure is given in Chapter 5. Chapter 5 also singles out individual galaxies or interacting systems of particular interest. Finally Chapter 6 summarises and concludes the findings of this dissertation.

Throughout this work the following cosmological values are assumed: $\Omega_{\rm m} = 0.307$ and $H_0 = 67.7\,{\rm km\,s^{-1}\,Mpc^{-1}}$ (Planck Collaboration et al., 2016).

Chapter 2

Observations, data reduction, and ancillary data

In this chapter we briefly cover the fundamental aspects of radio interferometry primarily following Smirnov (2011) in Section 2.1. We then describe some specifications of the MeerKAT telescope as an interferometer and the MeerKAT Galaxy Cluster Legacy Survey (MGCLS) in Section 2.2 and Section 2.3 respectively. Thereafter the methodology we implemented with regard to the calibration and imaging of the measurement sets used in this work is briefly described in Section 2.4. Finally, in Section 2.5 we describe the ancillary survey data used in our multi-wavelength analysis.

2.1 Radio interferometry overview

An imperative part of any observational astronomical study is having sufficient or at least appropriate angular resolution. Having high angular resolution allows one to study astronomical sources in more detail, enabling a much wider range of scientific return. The angular resolution of a single dish radio telescope is given by the following,

$$\theta = \frac{\lambda}{D}, \tag{2.1}$$

where θ is the angular resolution, λ is the wavelength of the light incident on the dish, and D is the diameter of the dish. It is thus more difficult to attain high angular resolution at longer wavelengths such as radio waves. To improve angular resolution we then need to increase the diameter of the telescope, however, the improvements we can make in this manner are limited by physical limits like structural integrity as well as by construction costs. These limitations are circumvented by the concept of an interferometer. An interferometer uses an array of separate antennas to simulate one large dish. In this way one can achieve significantly higher angular resolution as the formula for angular resolution is now given by

$$\theta = \frac{\lambda}{B_{max}}, \tag{2.2}$$

where B_{max} is the longest baseline (the distance between two given dishes) in the array. Interferometry allows us to achieve angular resolution typically only obtainable with unfeasibly large dish sizes. For instance, an $\sim$ 8 km maximum baseline in the case of MeerKAT or an Earth-sized maximum baseline for the Event Horizon Telescope (EHT). This solution is not without its additional set of challenges and limitations, one of which being geometric delays, shown in Figure 2.1, that need to be precisely accounted for to achieve accurate cross-correlation. This section takes

a concise look at the fundamental concepts involved in radio interferometry by following the formalism in (Smirnov, 2011, and references therin). Assuming emission

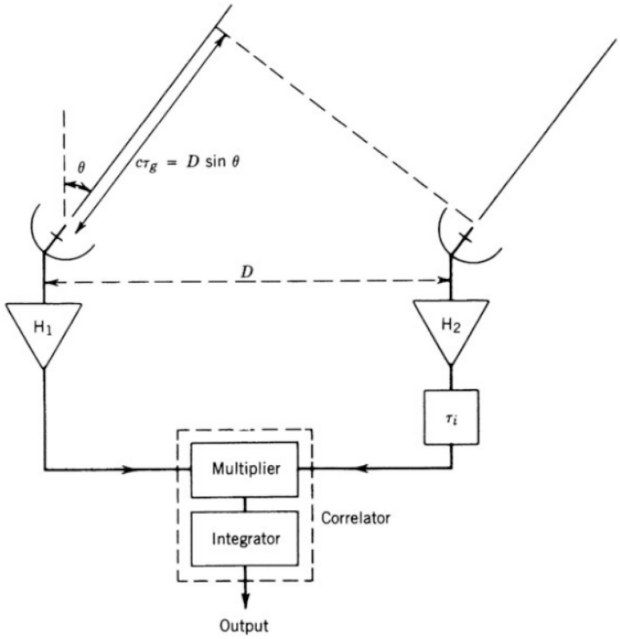


FIGURE 2.1: Two element interferometer showing key components of an interferometer such as the bandpass amplifiers (H_1 and H_2). as well as the geometric and instrumental delays (τ_g and τ_i). Image credit to Thompson, Moran, and Swenson (2017).

is from a constant-intensity, monochromatic, and coherent point source, we can represent this emission by a column vector of two complex numbers,

$$\boldsymbol{e} = \begin{pmatrix} e_x \\ e_y \end{pmatrix}, \tag{2.3}$$

where e_x and e_y are complex numbers representing the x and y components of the emission assuming an orthoganal co-ordinate system, xyz, with z pointing from the antenna to the point source. However, this emission will be corrupted by various effects that can all be represented by a single Jones matrix, $\boldsymbol{J} = \boldsymbol{J}_n \boldsymbol{J}_{n-1} ... \boldsymbol{J}_1$, comprised of all corrupting effects (such as atmospheric effects, Faraday rotation, etc.). The antenna thus measures a voltage represented in the following,

$$\boldsymbol{v} = \begin{pmatrix} v_a \\ v_b \end{pmatrix} = \boldsymbol{J}\boldsymbol{e}. \tag{2.4}$$

Now consider two-element interferometry that measures two voltages v_p and v_q where p and q are the locations of the two antennae. These voltages are combined by the correlator into 4 pairwise correlations corresponding to the 4 elements of the visibility matrix, V_{pq}, shown in Eq 2.5. In the following v^*_{pa} is the complex conjugate of v_{pa}, and the angle brackets enclosing the 4 pairwise correlations indicate an average over both frequency and time bins,

$$V_{pq} = 2 \begin{pmatrix} \langle v_{pa} v^*_{qa} \rangle & \langle v_{pa} v^*_{qb} \rangle \\ \langle v_{pb} v^*_{qa} \rangle & \langle v_{pb} v^*_{qb} \rangle \end{pmatrix}. \tag{2.5}$$

For an explanation of the factor 2 see Smirnov (2011). But Eq 2.5 can be represented differently by extracting the Jones matrix and rewriting in terms of the Stokes parameters I, Q, U, and V, see Hamaker and Bregman (1996) for a explanation of the relation to Stokes parameters. This is shown in the following, where H is the Hermitian conjugate transpose operator, and B is known as the brightness matrix,

$$\mathrm{V}_{pq} = 2\boldsymbol{J}_p \begin{pmatrix} \langle e_x e_x{}^* \rangle & \langle e_x e_y{}^* \rangle \\ \langle e_y e_x{}^* \rangle & \langle e_y e_y{}^* \rangle \end{pmatrix} \boldsymbol{J}_q^H = \boldsymbol{J}_p \begin{pmatrix} I+Q & U+iV \\ U-iV & I-Q \end{pmatrix} \boldsymbol{J}_q^H = \boldsymbol{J}_p \mathrm{B} \boldsymbol{J}_q^H. \tag{2.6}$$

The geometric phase delay τ_g needs to be compensated for by deriving the phase difference and accounting for it in the visibility matrix. We omit the details and refer the reader to Thompson, Moran, and Swenson (2017) for the full derivation. For antenna p (located at coordinates (u_p, v_p, w_p) in the co-ordinate system used by Thompson, Moran, and Swenson (2017)) the phase difference is found to be $\kappa_p = 2\pi\lambda^{-1}(u_p l + v_p m + w_p(\sqrt{1-l^2-m^2}-1))$ where l and m are directional cosines of $\boldsymbol{\sigma}$ (the direction from which the signal is arriving) and λ is the signal wavelength. We do not focus on this phase term and instead represent it by the Jones matrix K_p as follows,

$$K_p = \mathrm{e}^{-i\kappa_p} = \mathrm{e}^{-2\pi i(u_p l + v_p m + w_p(\sqrt{1-l^2-m^2}-1))}. \tag{2.7}$$

K_p is absorbed into $\boldsymbol{J}$, and by doing the same for antenna q we obtain the following,

$$\mathrm{V}_{pq} = \boldsymbol{J}_p \mathrm{B} e^{-2\pi i(u_{pq} l + v_{pq} m + w_{pq}(\sqrt{1-l^2-m^2}-1))} \boldsymbol{J}_q^H = \boldsymbol{J}_p K_p \mathrm{B} K_q^H \boldsymbol{J}_q^H = \boldsymbol{J}_p \mathrm{B} \boldsymbol{J}_q^H, \tag{2.8}$$

where $\boldsymbol{u}_{pq} = \boldsymbol{u}_p - \boldsymbol{u}_q$. When we account for contributions to visibilities from all directions Eq 2.8 becomes the following as we integrate over the solid angle,

$$\mathrm{V}_{pq} = \int_{4\pi} \boldsymbol{J}_p \mathrm{B} \boldsymbol{J}_q^H d\Omega. \tag{2.9}$$

To simplify this expression we do a sine projection onto the (l, m) plane and obtain,

$$\mathrm{V}_{pq} = \iint_{lm} \boldsymbol{J}_p(l,m) \mathrm{B}(l,m) \boldsymbol{J}_q^H(l,m) \frac{dldm}{n}, \tag{2.10}$$

where $n = \sqrt{1-l^2-m^2}$. If we then make the assumption that the visibilities are perfectly calibrated and have no direction-dependent effects we can negate the Jones matrices that makeup J such as the delay term K, antenna-based effects G, and direction-dependent effects E. Additionally, we absorb w_{pq} into E. The remaining simplified equation for perfectly calibrated visibilities is found to be the following,

$$\mathrm{V}_{pq} = \iint_{lm} \mathrm{B} e^{-2\pi i(u_{pq} l + v_{pq} m)} dldm. \tag{2.11}$$

Finally, we are able to recover the sky brightness B using a Fourier transform by the van Cittert-Zernike theorem. "The (2-D) lateral coherence function of the radiation field in space is the Fourier Transform of the (2-D) brightness (or intensity distribution) of the source" (Burke, Graham, and Wilkinson, 2019).

An interferometer does not fully sample the (u, v) plane, the way telescope measures Fourier components is described by its sampling function which is discussed in more detail in Subsection 2.4.2. To maximise the number of Fourier components measured, the rotation of the Earth is exploited in a process known as aperture synthesis. This is the name given to the process where the baselines cover larger arcs

in the (u, v) plane with more time that passes due to the rotation of the planet causing a change in the projected baseline lengths and orientations, enabling a broader sampling of spatial frequencies. An example of this is given in Figure 2.4, the (u, v) coverage of an observation used in this thesis.

2.2 MeerKAT

MeerKAT is a radio interferometer located in the Northern Cape of South Africa. The telescope serves as a precursor to the Square Kilometre Array (SKA). The MeerKAT array consists of 64 antennas in a layout where the majority of the antennas are located in a central region with only a minority being in an outer region. The core contains $\sim$ 70 per cent of the antennas with a minimum baseline of 29 m and a maximum baseline of 1 km. The outer region contains $\sim$ 30 per cent of the antennas with a maximum baseline of $\sim$ 8 km. Both regions are distributed such that they provide Gaussian (u, v) coverage. The core and outer array distributions are given in Figure 2.2 and Figure 2.3 respectively, reproduced directly from South African Radio Astronomy Observatory (SARAO[1]). All dishes are 13.5 m offset Gregorian and equipped with S-band, L-band, and UHF-band receivers with frequency ranges of $1750 - 3500$ MHz, $900 - 1670$ MHz, and $580 - 1015$ MHz respectively.

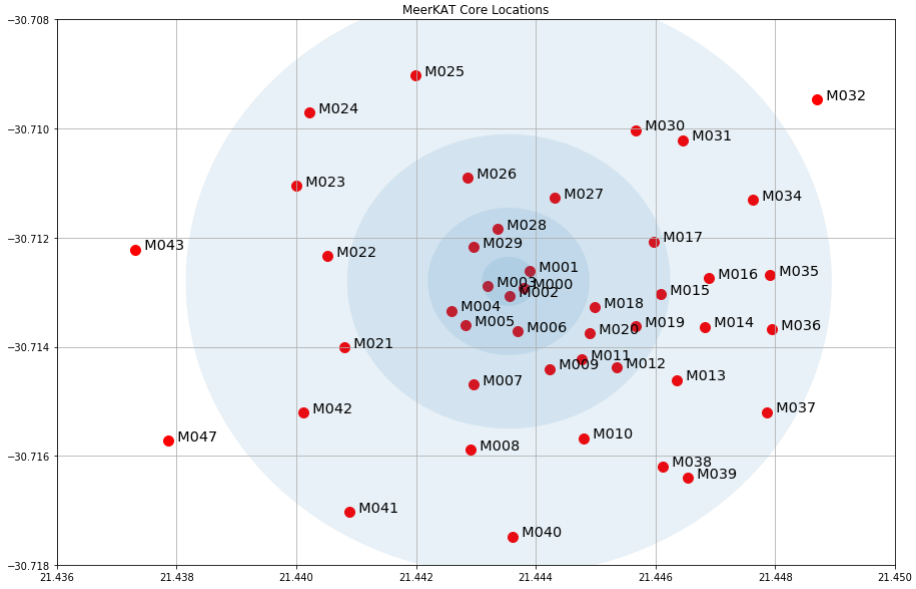


FIGURE 2.2: Dense inner core of MeerKAT's array configuration. Image credit: SARAO.

2.3 MeerKAT Galaxy Cluster Legacy Survey

MGCLS is a SARAO Science Legacy Survey that performed deep MeerKAT L-band observations of 115 galaxy clusters, observed for 6–10 hours each with MeerKAT in the correlator's 4k configuration. In this work, we use the first legacy data product release (MGCLS DR1) (Knowles et al., 2022), which includes the MeerKAT visibilities, enhanced, coarse resolution spectral and polarisation cubes at $\sim$ 8" and $\sim$ 15" that span the inner $1.2^\circ \times 1.2^\circ$ with a corrected primary beam. Regular image cubes

[1]https://skaafrica.atlassian.net/servicedesk/customer/portal/1/article/277315585

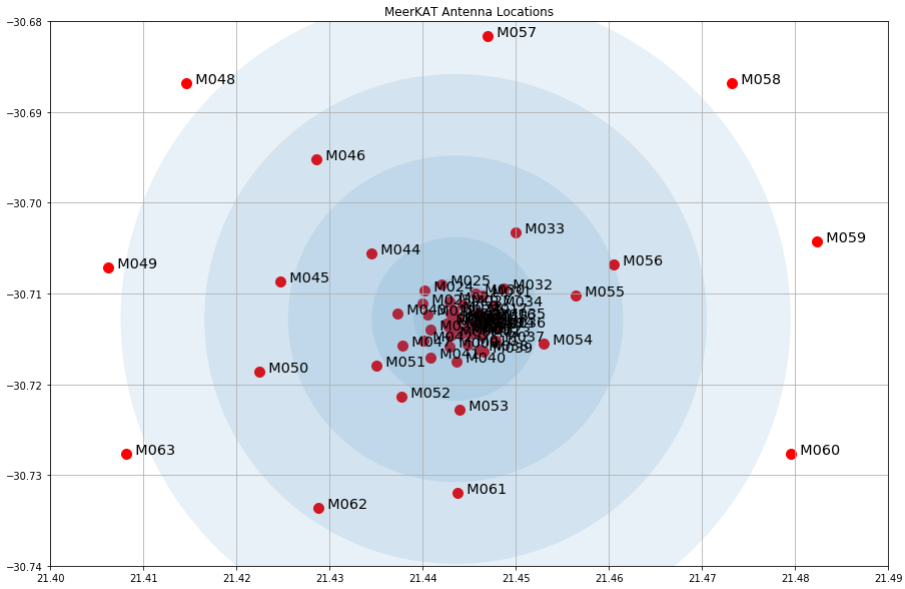


FIGURE 2.3: Portraying maximum baseline through showing antenna locations for all MeerKAT dishes. Image credit to SARAO.

at $\sim$ 8" angular resolution that span $2^\circ \times 2^\circ$ are also included. The frequency channels are $\sim$ 209 kHz in width. The angular resolution enables H I study of spatially resolved sources, while the fairly broad channel width enables H I mapping some cases, in the $0 \gtrsim z \gtrsim 0.9$ range.

Abell 3365 was the initial target of this study, before the serendipitous discovery, and is located at RA $=$ 05h48m12s and Dec $=$ $-$21d56m03s. A3365 has a velocity dispersion of 981 km s^{-1}, is at a luminosity distance of 440.3 Mpc ($z = 0.093$).

The raw visibility measurement sets used in this work comes from two observations of A3365 one on 14-15 November 2018 and the other on 18-19 November 2018. Both observations had a correlator dump time of $\sim$ 8 seconds. Both observations included 3 sources: J0408-6545 (RA $=$ 04h08m20s, Dec $=$ $-$65d45m07s), Abell 3365, and J0609-1542 (RA $=$ 06h09m40s, Dec $=$ $-$15d42m40s). The first observation was 10.05 hours long and used 56/64 of the MeerKAT antennas. The second observation was 10.1 hours long and used 59/64 of the MeerKAT antennas. In Figure 2.4 we show an approximation of the (u, v) coverage obtained during our observations, the plot was simulated using SARAO's uv-coverage calculator[2].

2.4 Calibration and imaging

We used OXKAT[3] (Heywood, 2020) to reduce the MGCLS Abell 3365 data. OXKAT is semi-automatic software geared towards being a complete pipeline (including flagging, reference calibration (1GC), self-calibration (2GC), and direction-dependant calibration (3GC)) for the data reduction of MeerKAT Measurement Set format data sets. OXKAT makes use of existing astronomy packages including but not limited

[2]https://apps.sarao.ac.za/calculators/uvbeam
[3]https://github.com/IanHeywood/oxkat

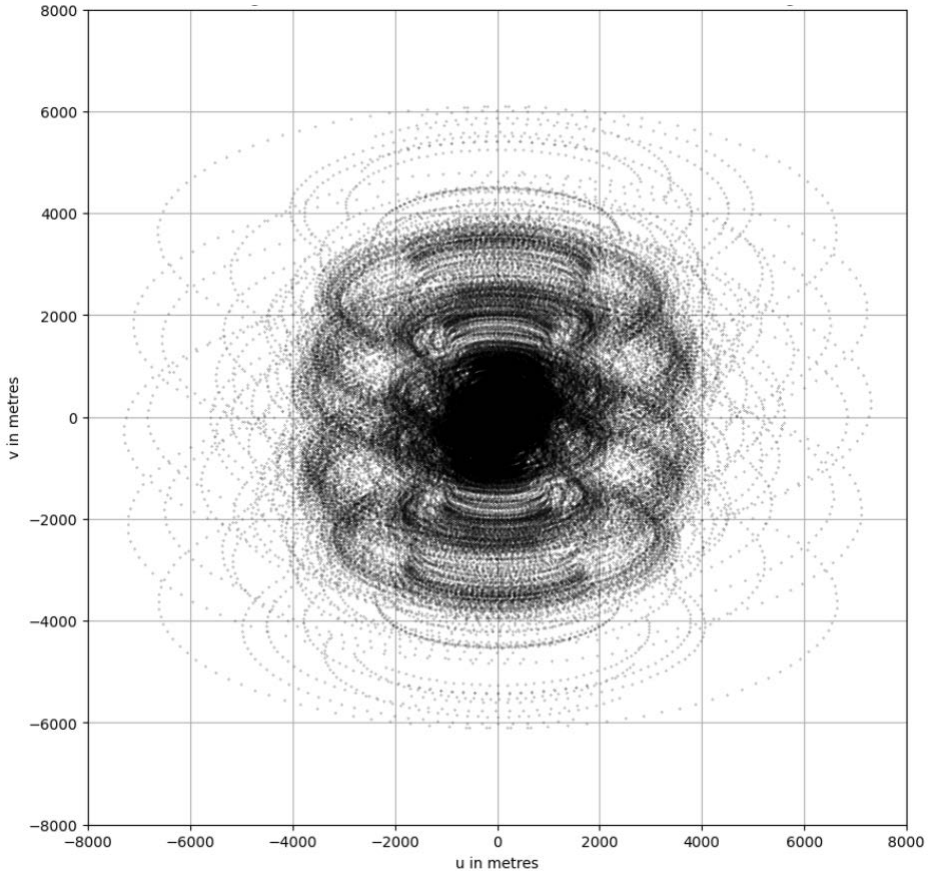


FIGURE 2.4: MeerKAT (u, v) coverage of observation of A3365 at RA=05:48:12 and Dec=-21:56:03 with a horizon of 15.0 degrees. This coverage is for a single frequency channel centred on 1.4 GHz.

to: CASA[4] (McMullin et al., 2007), WSCLEAN[5] (Offringa et al., 2014), and CUBICAL[6] (Kenyon et al., 2018) which are containerised by SINGULARITY[7]. OXKAT automatically generates slurm submission scripts to accommodate for use on high-performance computing (HPC) clusters such as the one used in this work. We use the ilifu[8] cloud computing facility developed and maintained by The Inter-university Institute for Data Intensive Astronomy (IDIA[9]) together with OXKAT to reduce the raw visibilities from MGCLS.

In this section, we briefly describe the calibration process. Calibration begins with first generation calibration (1GC) which includes multiple stages of automated and manual in parallel with reference calibration. Reference calibration is the term used to describe the process whereby sources that are particularly well characterised in terms of flux density, source morphology and/or spectral properties are observed in addition to the science target. These sources are then used as calibrators to correct for corrupting effects such as atmospheric effects, antenna/feed effects like system temperature and the primary beam, low-noise amplifier (LNA) effects on the gain, phase, and delay, and radio frequency interference (RFI). In 1GC we also establish the absolute flux scale as the raw visibility measurement set has an arbitrary flux scale. Thereafter the data cubes are imaged using WSCLEAN, which utilises multi-scale multi-frequency deconvolution algorithms. We then improve image fidelity using self-calibration during second generation calibration (2GC) where the image produced with WSCLEAN is used as a model in an iterative process to re-calibrate until a desired improvement on the gain solutions, initially produced in 1GC, is achieved. After 2GC, continuum subtraction is implemented to remove continuum emission and thereby separate out the spectral line emission.

2.4.1 First generation calibration (1GC)

The majority of the tasks that OXKAT uses throughout 1GC are from the CASA data processing software. One of the primary purposes of 1GC is to account for the corrupting effects that lead to misaligned phases and varying amplitudes. Furthermore, there is a need to scale the flux of all sources involved as the flux values have an arbitrary scale in the raw measurement set. Finally, we calibrate corrections for the bandpass, which is the spectral response of the system. Throughout the entire process, it is vital to consistently flag bad data due to RFI and other corrupting effects between steps.

We use TRICOLOUR[10], the autoflagger, to flag RFI and bad data intermittently during 1GC. Manual flagging is done with CASA's `flagdata` by specifying bad antennas, (u, v) ranges, etc., following close inspection of the data through a wide range of plots. OXKAT also autoflags data using the `tfcrop` and `rflag` modes between calibration steps.

Cross calibration is the process whereby complex gains (amplitude and phase) are

[4] https://casa.nrao.edu
[5] https://gitlab.com/aroffringa/wsclean/
[6] https://github.com/ratt-ru/CubiCal
[7] https://github.com/sylabs/singularity
[8] https://www.idia.ac.za/
[9] https://www.ilifu.ac.za/
[10] https://github.com/ratt-ru/tricolour

calibrated. Here we make corrections that account for corrupting effects like atmospheric phase shifts, such as those caused by free-electron induced diffraction and refraction in the ionosphere, tropospheric absorption and scattering, antenna flexure effects under gravity, etc. The calibrator used is generally a bright point source since it is well characterised in Fourier space. It has constant amplitude and zero phase (if at the phase centre) in Fourier space, therefore any deviations observed can be assumed to be caused by corrupting effects. The gain calibrator needs to be relatively close ($\lesssim 10$ deg) to the target since the observation will involve intermittently moving between observing the target and the gain calibrator on short timescales (every 10-25 minutes). To sufficiently sample time-variable complex gain fluctuations. OXKAT uses CASA's `gaincal` task to determine the complex gains. Thereafter, CASA's `applycal` is used to interpolate the solutions to the target field. The measurement set used in this work includes ~ 45 scans of ~ 1 min each of J0609-1542 as the complex gains calibrator. J0609-1542 was observed intermittently with the target (A3365), where the target was measured for ~ 10 min for every ~ 1 min scan of J0609-1542.

To obtain the flux scale of our target source we use an absolute flux calibrator source, this method is sometimes referred to as 'bootstrapping'. The flux calibrator is required to be very bright and well modelled with a stable flux density. This allows us to compare the arbitrary flux values in the measurement set with the true flux value we expect. Since the flux of the source is known, we can convert the arbitrary values into a physically meaningful absolute flux scale (Jansky in our case) using the deviation. This is done by first using CASA's `setjy` to set the amplitude scale, then applying this scale to the target source using `fluxscale`. Flux calibrators need not be close to the target source as fewer observations are needed since flux calibration is fairly time-in-dependant. J0408-6545 was used as the flux calibrator for this measurement set.

The bandpass is the spectral response of an individual antenna system. Corrupting effects in the bandpass are generally due to receiver passband function and signal processing artefacts among others. For each antenna, we derive solutions for the amplitude and phase. All baselines to an antenna can be used to derive the amplitude as a function of frequency. We expect to have a fairly constant amplitude as a function of frequency. Bandpass calibration calculates and fits a solution to the data to ensure constant sensitivity over the frequency range. We can achieve this by using a bright ($\gtrsim 1$ Jy) calibrator after amplitude and phase calibration. The bandpass calibrator needs to be bright since we derive solutions for each channel within each spectral window. This is done using `bandpass` within CASA through OXKAT. The flux calibrator, J0408-6545, doubles as the bandpass calibrator due to its sufficient brightness. J0408-6545 was observed every ~ 1 hour for ~ 10 min for a total of 9 scans.

2.4.2 Imaging

In this subsection, we briefly discuss the primary ideas behind the imaging process. Imaging is done through the exploitation of Fourier transforms to approximate the sky brightness from the Fourier components measured in (u, v) space by interferometers. However, the Fourier components measured by an interferometer are limited by the number of baselines, and thus by the number of antennas. This means we

have an incomplete measurement in Fourier space in contrast to the complete measurement needed to capture the true sky brightness distribution. To account for the incomplete Fourier components, one introduces a sampling function that is 1 where there is a Fourier component present and 0 where there is none. With the sampling function being implemented, the "dirty beam" or point spread function (PSF) is defined as the Fourier transform of the sampling function. Our interferometer thus measures the Fourier components multiplied with the sampling function. We can then recover the convolutional product by using a Fourier transform to obtain what is known as the "dirty image", which is the true sky brightness convolved with the point spread function. To improve the image, we need to deconvolve the PSF from the "dirty image" to recover the true sky brightness. It is possible to deconvolve the PSF since we know what the sampling function is from the locations of the antennas, as well as the pointing position and the rotation of the Earth. However this process is non-linear and is a mathematically ill-posed problem as many different sky brightness distributions could solve the deconvolution. This is alleviated by the primary assumption of the `CLEAN` algorithm that the sky can be approximated by a series of unresolved point sources. (Thompson, Moran, and Swenson, 2017).

We now give a general overview of the `CLEAN` algorithm:

1. Obtain the "dirty image" and the PSF by taking the inverse Fourier transform of the convolution product and the sampling function respectively, as described above. The maximum brightness (i.e. the highest peak in the "dirty image") is then located.

2. A fraction of the dirty image peak (typically 10 per cent) is then subtracted from the residual image. This is done by subtracting a scaled PSF centered on the location of the brightest pixel.

3. The location and amplitude of this scaled peak point source are then added to a clean map as a Dirac delta. The model image is "restored" using the "restoring beam" to the clean image. The "restoring beam" is a 2D Gaussian fit to the PSF. A Gaussian is a good approximation of the PSF without sidelobes, had the aperture been fully filled. This Gaussian function has the same full width at half maximum (FWHM) as the original PSF. Had the model not beam restored using the restoring beam, the clean image would only consist of numerous Dirac delta functions. To fit the restoring beam to the original PSF, it is best to ensure that the pixel scale is $< 3-6\times$resolution (Thompson, Moran, and Swenson, 2017). The clean map is the end product of the imaging process.

4. Iteratively perform the above steps until one of the user-specified criteria are reached, which are the maximum number of clean iterations or a residual image threshold peak is reached. When the residual image appears consistent with Gaussian noise the imaging process has most likely been completed. This is often clear when the RMS does not decrease after an iteration. What remains in the residual image at this point is likely noise and calibration artefacts (Thompson, Moran, and Swenson, 2017).

A (u, v)) weighting scheme, BRIGGS, used in the imaging of the data cubes is implemented in this work. In the (u, v) plane larger baselines are distributed over a larger number of grid points when compared to the shorter baselines in the inner

(u, v) regions. Weighting can to some extent tailor the imaging properties to the science requirements by either leaving weights unmodified (natural weighting) or by dividing weights by the local density of points (uniform weighting). In the BRIGGS weighting scheme, the ROBUST parameter can take a value between -2 (uniform) and +2 (natural). Natural weighting typically results in lower image RMS with the caveat of losing angular resolution, due to the gridding resulting in an increased weighting of small Fourier frequencies. Natural weighting also results in higher sidelobe levels. Uniform weighting maximises angular resolution and minimises PSF sidelobe levels at the cost of sensitivity due to small Fourier frequencies being weighted down (i.e. maximum baselines/large Fourier components that determine resolution have a larger effective weighting). In this work, 3 cubes are imaged with ROBUST parameters of 0, 1.0, and 2.0 using WSCLEAN. The ROBUST 2.0 cube serves as the most sensitive data product, and is used in the source-finding process while the cubes with ROBUST 0 and 1.0 are used for various calculations, analytics, and manual reliability checking.

2.4.3 Second generation calibration (2GC)

To improve both the fidelity and the dynamic range of our image, we implement self-calibration which we now give an overview of. Bright continuum emission causes corrupting artefacts within the post-1GC image. These artefacts are significantly reduced with the use of self-calibration. The essence of self-calibration is to use a self-generated model of the target field brightness distribution to iteratively refine time-variable complex gain solutions. To start, an initial sky model, as well as a mask, are created using the cross calibrated target field data, the post-1GC image. A mask is generated using the initial image to identify regions above a local threshold RMS of 6 σ. Using the generated mask, the target is re-imaged following a process similar to that described in Subsection 2.4.2 with the exception of being restricted to only deconvolving emission located within the mask. The resulting image is used as the first model and is Fourier transformed into the model column of the measurement set. From this point, self-calibration continues in a 3-step process which improves the complex gains solutions using the improved sky model. In the first step, CUBICAL is used to solve for the delay and phase solutions with 1 min solution intervals and WSCLEAN's clean depth is set to `niter` = 80,000 iterations (or 50 μJy beam^{-1}, however, the former criterion is what is met). The second step uses CASA's `gaincal` to derive new solutions for phase only gains at 1 min solution intervals, again followed by a deconvolution step using a maximum number of iterations of 80,000, refining previous solutions. Finally, in the third step `gaincal` is used once more to solve for amplitude and phase gains at 5 min intervals, with the maximum number of interation increased to 250,000. The majority of these clean iteration are spent on the large-scale relic found to the north-east of the Abell 3364 cluster. The refined solutions derived during these three steps are then applied to the visibilities followed by re-imaging of the target, providing an improved sky model to repeat the process with.

2.4.4 Spectral line imaging

Following the self-calibration procedure implemented in 2GC, the data cubes are fully calibrated but contain both spectral line and continuum emission. To pursue the science goals of this project it is necessary that the continuum emission is removed from the data cubes. This is done in a 3-step process using CASA whereby

first the subtraction occurs in the (u, v) plane and then in the image plane. We begin by subtracting the current sky model contained in the model data column from the corrected data using `uvsub` task. Thereafter `uvcontsub` is used to subtract remaining continuum emission through fitting a 1st order (specified through the `fitorder` parameter) polynomial to continuum emission in the visibility plane at the native 8-sec time resolution. This fit is then subtracted from all channels resulting in a new measurement set. This process is typically quite effective at removing residual continuum emission near the phase centre. We then image the output measurement set (MS) into three cubes, all with 102 channels at a channel width of 209 kHz, but with ROBUST weightings of 2, 1, and 0 for cube 1, cube 2, and cube 3 respectively. The basic specifications of the cubes produced are given in Table 4.1. To correct for the aforementioned continuum emission towards the primary beam centre we perform the third part to our continuum subtraction procedure in the image plane. The `imcontsub` task estimates continuum emission by fitting a polynomial (2nd order in our case) to the channels of a data cube in the image plane, then uses this as a model to subtract continuum emission. We are then left with the three continuum subtracted cubes used in this work.

2.5 Ancillary data

2.5.1 MGCLS continuum

The radio continuum image used in this thesis, see Figure 4.8-4.12 is from MGCLS (Knowles et al., 2022). The image used is a 6335 $\times$ 6335 pixel image at pixel increments of 1.25" $\times$ 1.25". The observation was of Abell 3365 at RA $=$ 05h48m12s and Dec $=$ $-$21d56m03s at a frequency of 1.28 GHz, an angular resolution of $\sim$ 8", and a sensitivity of $\sim 3 - 5\,\mu$Jy beam^{-1} across the field-of-view. In Figure 2.5, we show the map of continuum emission from MGCLS generated using the full L-band bandwidth and data processing pipeline described in Knowles et al. (2022). The image is relatively free of bright, troublesome sources with obvious artefacts. The centre of the image is dominated by a large continuum relic to the northeast of the Abell 3365 cluster.

2.5.2 The Dark Energy Survey

In this work, we use the Dark Energy Survey Data Release 2 (DES DR2), an optical imaging survey by the Dark Energy Camera (DECam) (Abbott et al., 2021). DECam is located in Chile at Cerro Tololo Inter-American Observatory on the 4 m Blanco telescope. This survey consists of a source catalogue, co-added images, and data products from previous DES operations. The data we use comes from the coadded images of the DES wide-area survey that covered $\sim$ 5000 deg^2 of the southern Galactic cap. DES DR2 observed in 5 bands: g, r, i, z, and Y at 1.11", 0.95", 0.88", 0.83", and 0.90" with a median coadded catalogue depth of 24.7, 24.4, 23.8, 23.1, and 21.7 mag (for an aperture of 1.95" diameter at SNR=10) respectively. The survey has an internal astronomical precision of $\sim$27 mas and a photometric accuracy of $\sim$10 mmag.

2.5.3 The Wide-field Infrared Survey Explorer

Between 7 January 2010 and 6 August 2010 NASA's Wide-field Infrared Survey Explorer (WISE) mapped the entire sky in the following 4 bands: W1 (3.4μm), W2 (4.6μm), W3 (12μm), and W4 (22μm) that have an angular resolution of 6.1", 6.4",

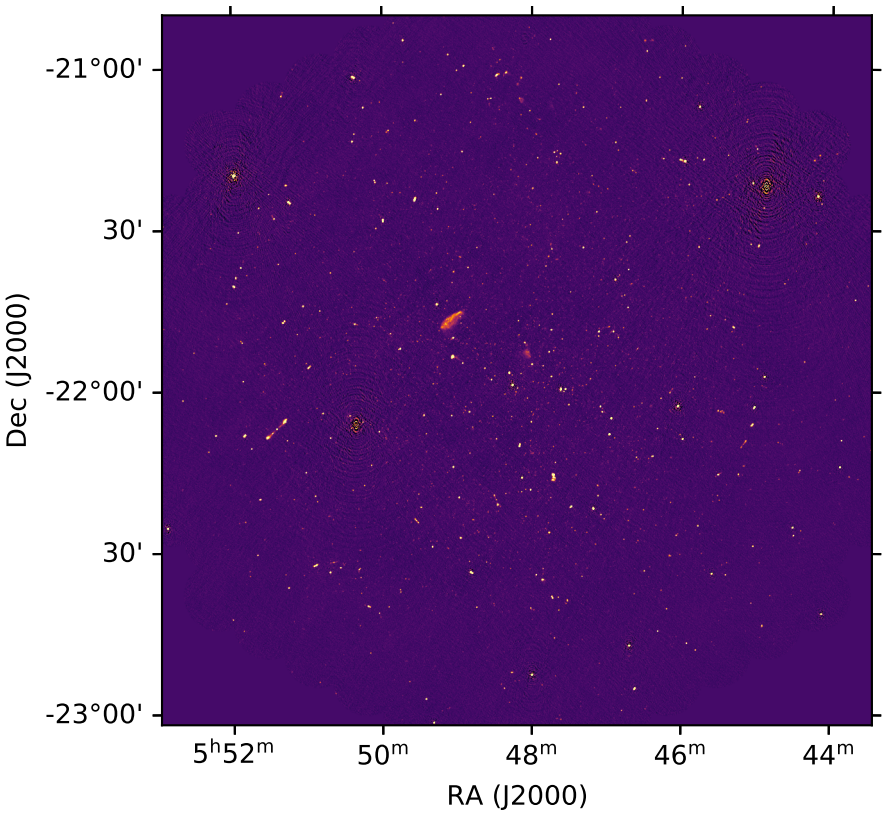


FIGURE 2.5: MGCLS continuum map at 1.28 GHz. The PSF is 8.63" × 7.43".

6.5", and 12.0" respectively (Wright et al., 2010). WISE used a 40 cm telescope feeding array with a total of 4 million pixels. WISE achieved 5σ sensitivities of 0.08, 0.11, 1.00, and 6.00 mJy in unconfused regions on the ecliptic (or better if nearer to the ecliptic poles due to denser coverage) for the bands respectively.

One of the main components of the WISE All-sky Release includes the WISE Image Atlas, which is comprised of 18,240 Atlas tiles. Each Atlas tile comes from one image set which is a 4095×4095 pixel FITS file covering $1.546^\circ \times 1.564^\circ$ at 1.375"/pixel. The other primary component is the WISE source catalogue. Sources are required to have a signal-to-noise ratio of greater than 5 (SNR > 5) as well as needing to pass a set of reliability criteria. After these conditions are applied there are 563,921,584 sources in the catalogue. Within the catalogue, the following measurements are given: J2000 positions, photometry in the four WISE bands, and various measurement quality flags including but not limited to: image artefact contamination, extended source, and variable source. For all sources with SNR > 40 the astronomical precision is ~ 200 mas RMS on each axis with respect to the Two Micron All Sky Survey (2MASS) (Skrutskie et al., 2006) reference frame.

Chapter 3

Source finding

3.1 Source finding with SoFiA 2

3.1.1 Source finding algorithm selection

Source finding is an useful tool for detection of various sources, as is the case when dealing with galaxy groups or clusters. It is generally a semi-automated or automated process where detection algorithms are used to identify sources based on particular input parameters. Often source finders provide the user with the option to output a source catalogue with an array of properties associated with the sources it has detected. Source finding is an important part of studying a medium to large number of galaxies as it significantly reduces manual intervention as well as providing convenient features such as cutouts and catalogues, thus reducing the time needed to study these multi-member systems.

Popping et al. (2012) compare the performance of various spectral line source finders based on completeness and reliability. This was to determine the optimal source finding application to use for surveys made using the Square Kilometre Array (SKA; Dewdney et al., 2009) precursors, MeerKAT (Jonas, 2009) and the Australian SKA Pathfinder (ASKAP; DeBoer et al., 2009), such as Looking At the Distant Universe with the MeerKAT Array (LADUMA; Baker et al., 2018), and the Widefield ASKAP L-band Legacy All-sky Blind Survey (WALLABY; Koribalski et al., 2020). Popping et al. (2012) tested DUCHAMP (Whiting, 2012), the 2D-1D Wavelet Reconstruction source finder (Flöer and Winkel, 2012), and smooth plus clip finder (S+C Serra et al., 2012) among other source finders. They tested the source finders on two cubes, the first with point sources with Gaussian velocity profiles and the second populated with spatially extended galaxies with inclinations and rotation curves. For the point sources, DUCHAMP performed the best, while for the spatially extended sources, the S+C finder was the most complete and reliable.

The S+C finder follows a simple procedure: The finder smooths the cube over the sky or velocity (or all 3 dimensions), then searches for voxels above a given threshold. In the event that a voxel is sufficiently bright, it is added to a mask. Masks are made from each smoothed cube and added together to form a final mask from the union of all masks (Popping et al., 2012). This is included in Source Finding Application (SoFiA Serra et al., 2015) and is the most commonly utilised source finding algorithm within SoFiA. SoFiA is specifically designed for H I source finding within extragalactic H I surveys and gives the user freedom to customise the smoothing kernels, flux thresholds, reliability tolerances, merging parameters, and many more. SoFiA has the capability of creating moment maps as well as catalogues that parameterise the candidate sources found.

While SoFiA generated catalogues are found to be sufficiently complete and reliable for extragalactic H I surveys, it has a significant memory footprint. SoFiA 2 is a re-implementation of SoFiA with parts of the original pipeline rewritten in the C programming language (Westmeier et al., 2021). SoFiA 2 is also an automated 3D source finding application that came to be through the necessity for efficient automated source finding due to the large amounts of data coming from modern radio telescopes. SoFiA 2 significantly reduces the memory footprint of its predecessor and makes substantial improvements in computation time. Large data cubes can be run through the pipeline in minutes with SoFiA 2 instead of the hours required for SoFiA. SoFiA 2 retains the ability to create moment maps, cubelets (cube cutouts centred on sources), catalogues, and parameterisation of the sources. For the reasons stated above, we selected SoFiA 2 as our source finding algorithm and all results in this thesis use it.

3.1.2 Strategy and implementation specifics

We briefly describe vital parameters that were altered within the SoFiA 2 pipeline. Parameters that are not discussed here were left as default and the values thereof can be found within the SoFiA 2 manual and the appendix. The S+C algorithm was used for all source finding done in this work.

Preconditioning and smoothing

We choose to enable continuum subtraction in the SoFiA 2 options, which is implemented before source finding commences in the pipeline. This is done through the `contsub.enable` parameter. When set to True, this enables SoFiA 2 to attempt to subtract residual continuum emission. The `contsub.threshold` and `contsub.padding` parameters were left at the default of 2.0 and 4 channels respectively. Channels will be excluded from the polynomial fit if the flux density is greater than the `contsub.threshold` times the local noise. The `contsub.padding` provides a buffer around the channels that are excluded, in our case a 4-channel buffer on either side. Finally, SoFiA 2 provides two choices for polynomialfits: zeroth order (constant offset) and first order (offset + slope). In our source finding strategy we applied the first order polynomial through `contsub.order` = 1. During testing, we found that 12 source detections were lost when running the pipeline with continuum subtraction turned off.

In order to correct for spatial and spectral noise variations across the input data cube we set `scaleNoise.enable` to True. This allows SoFiA 2 to measure the noise of the input data cube and then divide the cube by this value. All parameters associated with noise scaling were left at defaul.

The `rippleFilter.enable` parameter was set to `True`. Sometimes in data cubes there are spatially or spectrally extended artefacts that vary either across the sky or with frequency, resulting in spatial or spectral ripples. These artefacts could be elevated above the flux threshold after smoothing and result in false-positives. This option calculates the mean or median (the median mode is highly recommended in the documentation and is used in this work) within a running window, then subtracts this value from all individual pixels within the grid. Both the spatial and spectral size of the window and the step that the window moves in can be specified but were left at

the default of 31 spatial pixels and 15 channels. The step size was also left at the default of half the window dimensions. The documentation warns that the use of the `rippleFilter.enable` may cause real sources to be missed by the finder, however when this parameter is set to False we gain an additional 3 detections, all of which look to be false positives. Additionally, 2 real detections were missed when running the pipeline without artefact filtering.

Smoothing

The user can input the size of the kernels used to smooth the data cube using the `scfind.kernelsXY` and `scfind.kernelsZ` parameters which specify the size of kernels in pixels and channels respectively. SoFiA 2 uses a Gaussian kernel for spatial smoothing and a boxcar kernel for spectral smoothing. By choosing the kernels with relevant scales, sources with matching scales will have enhanced signal-to-noise ratios. SoFiA 2 can take a list of kernels for both parameters and will match all kernels from the spatial list with all the ones from the spectral list and vice versa. For `scfind.kernelsXY` we used 0,2,4,6 pixels (where one pixel is 2"×2") and for `scfind.kernelsZ` we used 0,1,2,3,7,15 channels (where one channel corresponds to ~ 46 km s^{-1}). These values result in the same minimum and maximum kernel sizes as the default values, but have a higher total number of kernels due to additional intermediate values to improve the likelihood of locating sources with sizes matching the intermediate kernel sizes.

Explanation of the flux threshold

The single most influential parameter in SoFiA 2 is that of the flux threshold, changed through `scfind.threshold`. Pixels found to have brightness above this threshold times the noise level in cube post-smoothing are added to the detection mask described in Subsection 3.1.1. The default value is 5. Higher values provide more reliable sources but might miss out on faint sources. Lower values result in more complete catalogues but have a higher probability of containing spurious detections. This parameter was extensively tested to find the optimal balance needed for a complete catalogue while minimising the amount of manual input needed to remove false positives. We iteratively ran three cubes with ROBUST weightings of 0, 1, and 2 through the source finding pipeline for thresholds from 3 to 9 with intervals of 0.2. For detection purposes we only use the results from the ROBUST 2 weighted cube, as the higher signal-to-noise allows for a more complete catalogue to be compiled. However putting the remaining cubes through the pipeline and thereby creating moment maps and catalogues is useful both when manually inspecting an individual detection's reliability and when analysing the galaxies, as the ROBUST 0 and 1 have better spatial resolutions. The documentation suggests a value of between 3 and 5. The reason for testing higher thresholds was that the source count fall-off after 6.0 was not significant, as most sources were still detected at thresholds above 6.0 while the amount of false positive detections were reduced. The final decision was to use a value of 6.4 as this gives us a high level of confidence that the sources deemed true detections by SoFiA 2 are in fact real, while still providing us with a complete catalogue comparable to those produced at lower thresholds. We found little success using the lower thresholds, as the number of detections by SoFiA 2 was unfeasibly high at thousands of detections.

Linking, reliability, and mask dilation

SoFiA 2 offers many linker and merger parameters which can be used to specify the manner in which pixels are allocated to individual sources. For each pixel detected above the flux threshold, SoFiA 2 searches the surroundings within a given pixel and channel number in order to link pixels to form sources. This simple friends-of-friends algorithm is efficient at forming pixels into parameterisable sources. The only parameter that we altered was `linker.minsizeZ` by setting it to 1 channel. This was done to include single-channel sources, with the caveat being that more manual inspection was required to remove false single-channel detections that are somewhat common within MeerKAT 4K mode data cubes in general. The default value of 5 channels resulted in many missed sources due to low velocity width galaxies. The values of `linker.radiusXY` and `linker.radiusZ` were left at the default 1 to clearly distinguish between individual sources as numerous interacting systems within the cube would be classified as one source by SoFiA 2 had we opted for a higher value.

SoFiA 2 gives the user the option to turn on a reliability algorithm that discards sources that fail to reach a reliability threshold set by the user. We will not go into detail on the workings of the reliability algorithm and refer the reader to the SoFiA 2 manual, we instead give a brief description. The algorithm works on the concept that false and real source pixel distributions will occupy different regions in parameter space. It also assumes that all real astronomical sources have positive flux. This means any negative flux is assumed to be noise peaks or artefacts while positive flux could be real sources or noise peaks. The algorithm was developed to allow the user to set the flux threshold to a low value ($\sim 3-4$) since the reliability threshold will filter many false detections out of the catalogue. The documentation warns that for the algorithm to be successful it is important that there are many negative flux detections in the catalogue produced without the reliability parameter enabled. While theoretically not particularly important for our case since we used a relatively high threshold of 6.4, we found during testing that with the setting turned on, we obtained 43 detections, and with the setting off we found 74 detections. This test was done with the default values for all reliability parameters, that is `reliability.theshold` = 0.9 and `reliability.minSNR` = 3.0 among others. Many of the additional detections were found to be real using manual inspection. The lack of negative voxels above the flux threshold could be the reason the reliability algorithm throws out real sources. The final catalogue used was produced with the reliability option turned off. This gives a more complete catalogue however requires much more manual intervention as many duplicate sources are included when the reliability option is not used. The majority of additional sources were duplicate or overlapping detections that SoFiA 2 failed to separate into different sources. Fortunately, these cases are trivially removed by manual inspection.

A common problem when running source finding applications at higher flux thresholds is that source masks often miss real emission. This happens when emission surrounding sources falls below the flux thresholds and is thus not included in the mask. SoFiA 2 provides a solution for this through its mask dilation option. When `dilation.enable` is set to True, SoFiA 2 will dilate the source mask outwards both spatially and spectrally in an attempt to capture all flux associated with a particular source. This is done by growing the mask in steps until either the total flux of the source is increased by less than a threshold set by the user, or until a maximum number of iterations is reached. For our work this was an instrumental setting to

utilise, considering the high flux threshold of 6.4 that was selected. The maximum iteration count was left at the default 10 spatial iterations and 5 spectral iterations, and the dilation flux threshold was also left at the default value of 0.001 (0.1%).

Finally, SoFiA 2 gives the user many options for output products such as catalogue (ASCII/SQL/XML), parameterisation, moment 0 and moment 1 map, cubelets (individual source cube cutouts), mask, and more. Besides the default outputs, we chose to output moment maps as well as cubelets. The cubelet option produces a moment 0 and moment 1 map as well as a table of the integrated spectra of the sources in addition to a cube cutout for each source. However, to make specific improvements, we did not utilise the SoFiA 2 moment 1 maps and instead manually reproduced the moment 1 maps. This was done by utilising the cubelets produced by SoFiA as well as the masks to create intensity-weighted velocity maps. The reason therefor was to give us freedom over the RMS ratio cut that we apply to our moment 1 maps, we selected 3.2 $\times RMS$.

Chapter 4

Results

In this chapter we state H I cube properties and uses in Section 4.1, and show a channel map. In Section 4.2 we address the question of assigning group membership to galaxies. We end the chapter by calculating H I properties and SFR and stellar mass as well as showing H I and multiwavelength maps of individual galaxies in Section 4.3.

4.1 H I cubes

Three cubes were produced and used throughout this thesis. Cube 1 being the primary cube, with a ROBUST weighting of 2, was used for source finding, moment map generation, H I spectrum plotting, and calculation of quantities such as the H I column density and H I mass of individual galaxies. The reasoning behind this decision is that with the ROBUST weighting of 2, one typically achieves higher signal-to-noise ratios by minimising the RMS in each channel due to each visibility contributing its maximum statistical weight to the corresponding channel map. This makes it the more pragmatic choice for source finding when compared with Cube 2 and Cube 3 which have considerably lower signal-to-noise ratios, resulting in a more complete source catalogue. Cubes 2 and 3 attain their value by having superior angular resolution when compared to Cube 1, as shorter baselines are down weighted. These two cubes play a role in analysing individual galaxies, both by helping to determine if SoFiA 2 detections are real galaxies and also by providing another means to cross-match galaxies through spectra derived from the different cubes. Cube 2 was also used for some H I property calculations, such as H I mass and H I diameter. See basic cube properties in Table 4.1. See Figure 4.1 for a channel map extracted from Cube 1, we can clearly identify emission associated with many galaxies within this single $\sim \Delta V = 46\,\mathrm{km\,s^{-1}}$channel map of width 209 kHz. Figure 4.2 shows the moment 0 map obtained from SoFiA 2 during the source finding process, this shows the 74 galaxy candidates given by SoFiA 2 in the H I catalogue.

While the initial goal of this project was aimed at the galaxy cluster Abell 3365, upon inspection of the average frequency of the H I galaxies in the SoFiA catalogue it was noticed that the galaxies detected were at a lower redshift of $z \sim 0.04$. This lead to the investigation of the newly discovered foreground galaxies.

TABLE 4.1: Comparison of basic properties of the cubes generated in this work. This highlights the trade-off between signal-to-noise and angular resolution.

ID	ROBUST	RMS (μ Jy beam^{-1})	Restoring beam FWHM
Cube 1	2.0	$\sim$53	30.654" $\times$ 30.654"
Cube 2	1.0	$\sim$54	25.792" $\times$ 25.792"
Cube 3	0.0	$\sim$74	7.641" $\times$ 7.641"

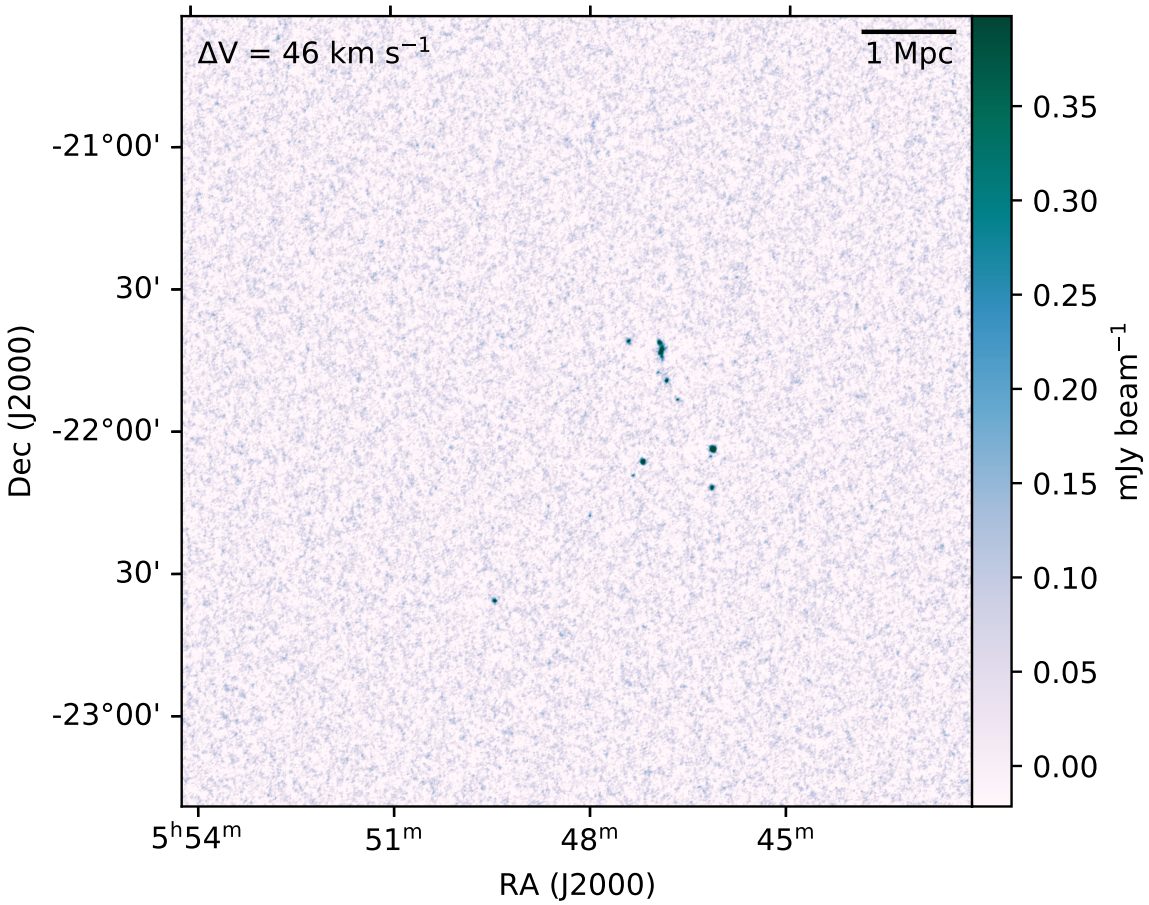


FIGURE 4.1: Channel map of Cube 1 at 1365.5039 MHz, with RMS = 53 μJy beam^{-1}. The PSF is 30.6547" $\times$ 30.6547".

4.2 Group membership classification

The SOFIA 2 catalogue produced using the ROBUST 2 cube resulted in 74 sources, of which 47 were deemed to be real after manual inspection. This manual inspection included assessing mid-infrared and optical counterparts in the WISE and DES data respectively. In addition to this, we cross-match between the cubes with differing ROBUST weightings. Finally, the integrated spectra of the sources were inspected for low signal-to-noise ratios.

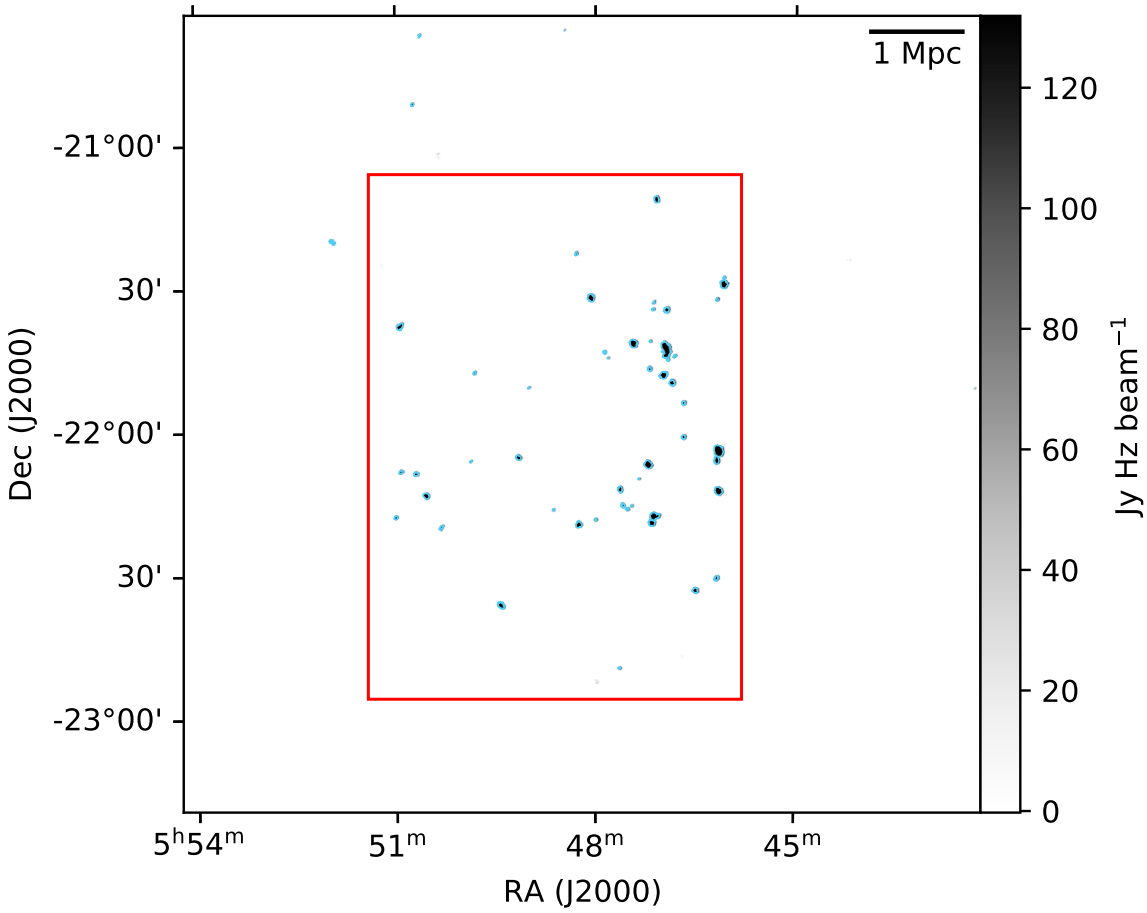


FIGURE 4.2: Moment 0 map produced by SOFIA 2 including all galaxies before manual intervention. The light blue contours show the 1×10^{20} atoms/cm^2 H I column density and the red rectangle represents the boundaries of Figure 4.7, which is a DES RGB image.

When examining the spatial distribution of the galaxies shown in Figure 4.2 we notice an extended structure. The structure appears to extend from the northern part of the group to the southern part. This observations is further strengthened upon spectral inspection of the group. We notice that the majority of the galaxies appear to grouped within a frequency range. Limiting the galaxies to a rough frequency range, the majority of galaxies on the left are not included while on the right most galaxies remain in the range. These hints of possible filamentary structure lead to the following, more robust, study of group membership. If the group is in fact in a filamentry structure, this would lead to some interesting study of group systems and could provide an intermediate state between a filament and a group. We discuss the implications thereof in chapter 5.

We do not expect a long-filamentary structure, such as the one reported, here to have a Gaussian velocity distribution as seen in virialized systems. However, we find it useful to perform a coarse quantitative analysis to determine group membership, which will be refined with future optical spectroscopy. To estimate group membership, we assume the group velocity centre is the 46 $\mathrm{km\,s^{-1}}$ velocity channel with the largest number of galaxies ($\nu \sim 1.3641$ GHz). Calculating redshift from this central frequency we find the group to be at $z \sim 0.041$. We then perform an Markov chain Monte Carlo (MCMC) analysis to find a Gaussian fit to the distributions of galaxies observed. While the binwidth used to create the data influences the Gaussian fits, the standard deviation of these distributions is comparatively similar for binning widths around $\sim 300\,\mathrm{km\,s^{-1}}$. Our selected value for the binwidth is $276\,\mathrm{km\,s^{-1}}$, that being a multiple of the channelwidth in the region of $\sim 300\,\mathrm{km\,s^{-1}}$, where testing showed the standard deviation to be fairly consistent. The MCMC chain plotted out on a histogram provides a proxy of the probability distribution of the parameters, the so-called posterior distribution function. We use the median of the posteriors to form our Gaussian model. The results of the Markov chain Monte Carlo derived Gaussian fit are shown in Figure 4.3. Pisano et al. (2011) perform thorough group membership identification through an iterative process whereby galaxies are identified as being part of the group if the optical velocity of a particular galaxy is within three velocity dispersions of the mean group velocity. The velocity dispersion is then, along with the mean recession velocity, recalculated and the process is repeated until the values of both change by less than 1%. The approach we took more closely represents the one shown by For et al. (2019), where the iterative process stops once there are no more exclusions. Our coarse approach to group membership classification deviates from the aforementioned methods in our assumption of the mean group velocity, and our recession velocities being derived from H I frequencies rather than using optical recession velocities. We do not use spatial information in assigning group membership due to the elongated filamentary-like structure, however, one can see in Figure 4.4 that despite using a velocity-only group identification approach, one can observe spatial clustering which supports our velocity-only based approach.

After applying the group member classification criterion of being within 3 σ from the mean velocity, 32 sources remain as part of the group. Figure 4.5 shows the final moment 0 map after galaxy group criteria are taken into consideration, Figure 4.6 shows the moment 1 map or the velocity field for the same group galaxies. We show a DES RGB image constructed from the i, r, and g bands covering the area shown by the red triangle shown in Figure 4.5 with light blue contours showing the

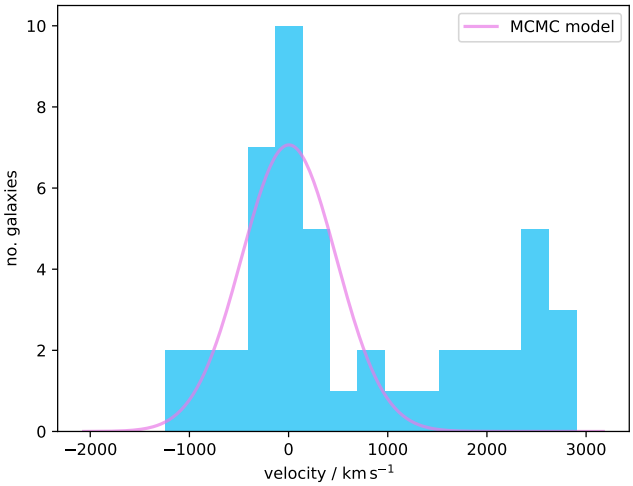


FIGURE 4.3: The distribution of galaxies by recession velocity, binned by a velocity width of 276 km s^{-1}. The pink line shows the median values of the MCMC-derived posteriors, and places 32 galaxies within the group selection velocity limit criteria.

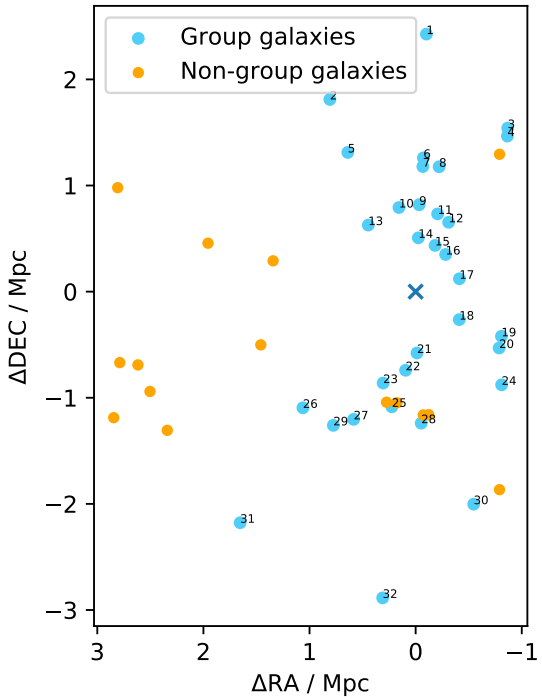


FIGURE 4.4: The relative spatial locations of the group galaxies. Light blue dots indicate group galaxies, while orange dots represent non-group galaxies based on the velocity distribution only. The blue cross corresponds to the geometric centre of the group.

1×10^{20} cm^{-2} H I column density in Figure 4.7. This DES map was created by combining multiple DES tiles (obtained with the DES TileFinder[1]) using MONTAGE[2].

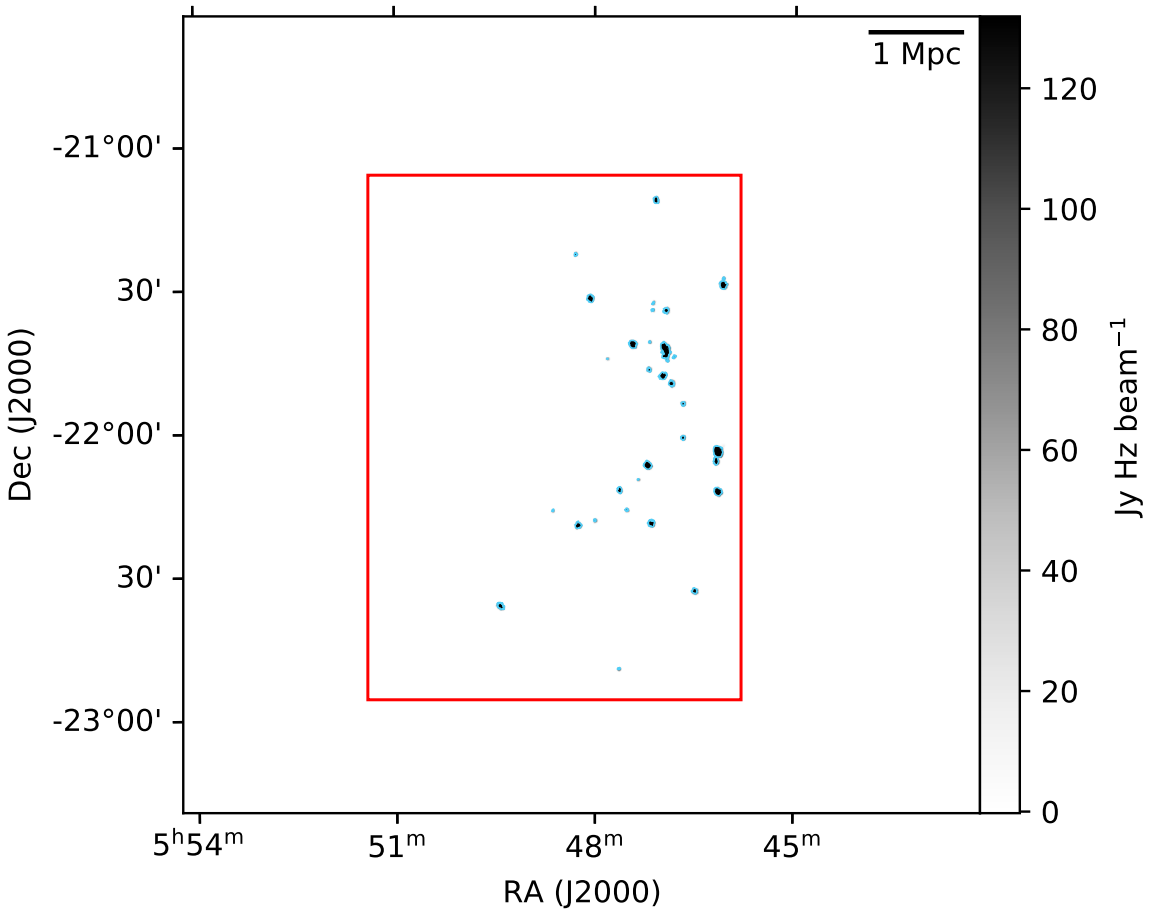


FIGURE 4.5: Final moment 0 map of the group galaxies. The light blue contours show the 1×10^{20} cm^{-2} H I column density and the red rectangle represents the boundaries of Figure 4.7.

[1]https://des.ncsa.illinois.edu/desaccess/tilefinder
[2]http://montage.ipac.caltech.edu/

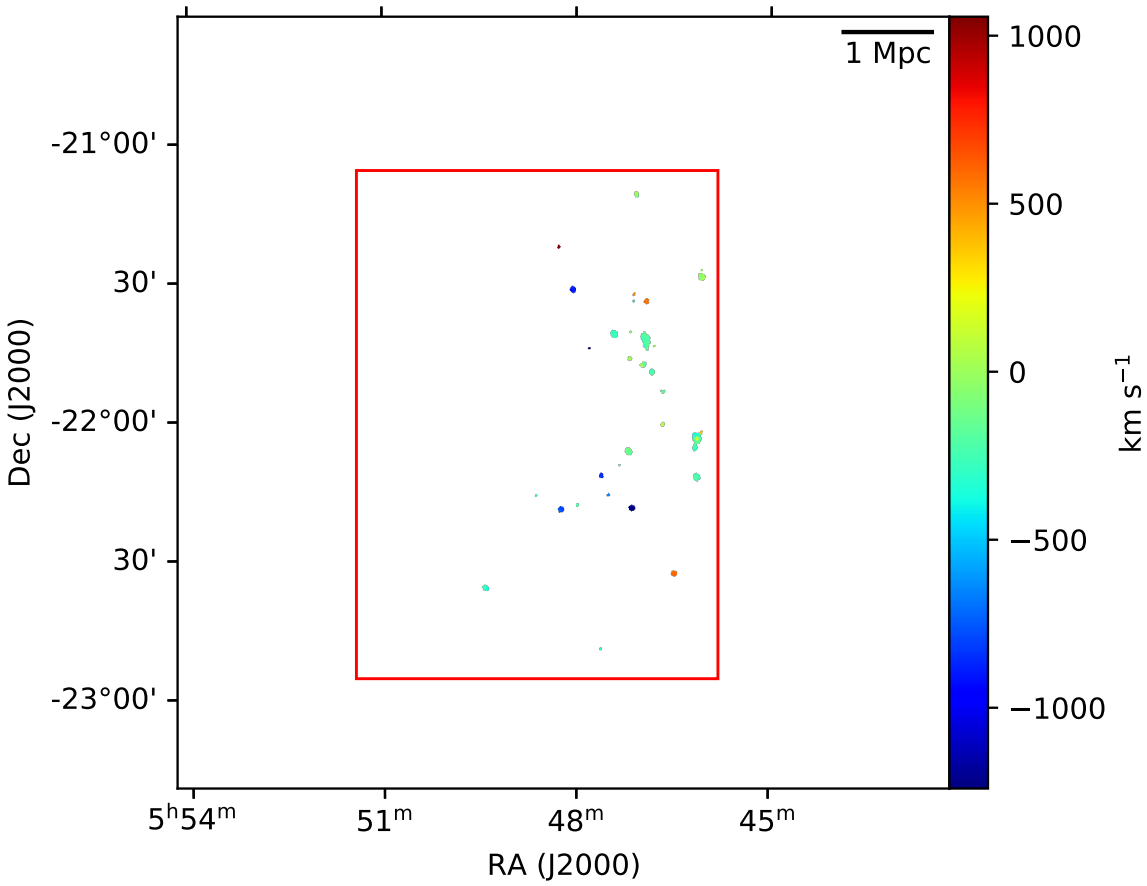


FIGURE 4.6: Final moment 1 map of the group galaxies. The red rectangle represents the boundaries of Figure 4.7.

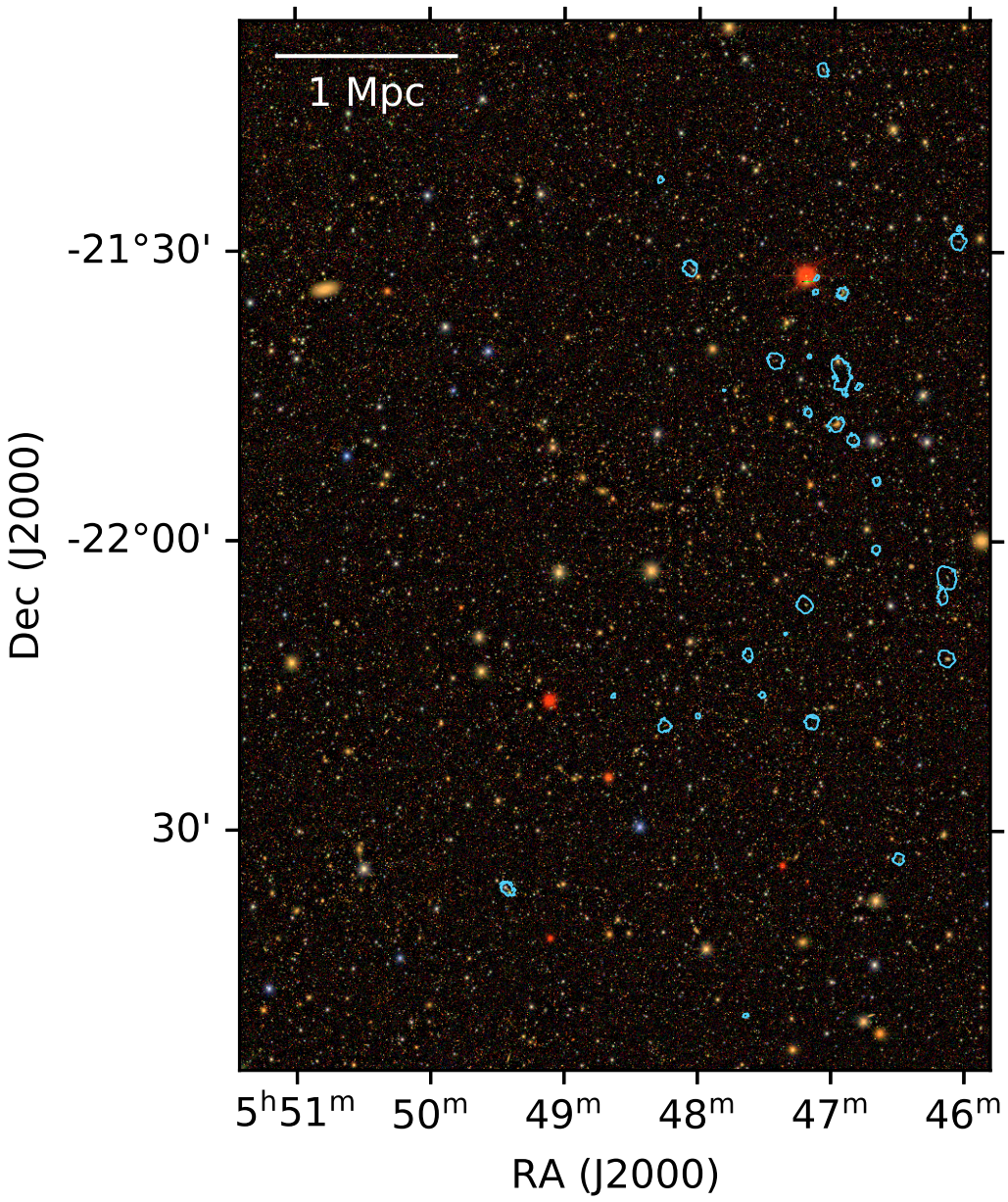


FIGURE 4.7: DES RGB image created from DES i, r, and g bands. Overlaid on the DES map we show the H I contours from the final moment 0 map including only group galaxies in light blue. The contour level represented corresponds to an H I column density of $1 \times 10^{20}\,\mathrm{cm}^{-2}$.

4.3 Individual galaxy properties

4.3.1 H I properties

For the group galaxies that are presented in Figure 4.5 we show H I and multiwavelength maps in Figures 4.8-4.12. We show the H I moment 0 (far left), H I moment 1 (middle left), radio continuum (middle), mid-infrared WISE W1 3.4 μm band (middle right), and optical DES RGB image, composed of the i, g, and r bands (far right).

H I column densities were calculated throughout this thesis using Equation 74 from Meyer et al. (2017). We calculate H I column densities as follows:

$$\left(\frac{N_{\rm HI}}{\rm cm^{-2}}\right) = 2.33 \times 10^{20} (1+z)^4 \left(\frac{S}{\rm Jy\ Hz}\right) \left(\frac{ab}{\rm arcsec^2}\right)^{-1}, \tag{4.1}$$

where $N_{\rm HI}$ is the column density in number of H I atoms per cm^2, S is the flux measured over the solid angle ab, where a and b are the angular major and minor axes of the restoring beam respectively. The assumptions are as follows: small angle approximation is used in calculating the area, $\frac{3}{4}$ H I atoms are in the upper hyperfine state, and the H I source is optically thin.

The following equation provides us with a way to specify the value of Hubble's Constant:

$$h_{\rm C} = \frac{H_0}{C\,{\rm km\,s^{-1}\,Mpc^{-1}}}. \tag{4.2}$$

An equation for H I mass is trivially achieved by multiplying the number of H I atoms with the mass of an H I atom, see Meyer et al. (2017) for details. We use Equation 45 given in Meyer et al. (2017) to calculate H I mass as follows:

$$\left(\frac{M_{\rm HI}}{h_{\rm C}^{-2}\,{\rm M_\odot}}\right) \simeq 49.7 \left(\frac{D_L}{h_{\rm C}^{-1}\,{\rm Mpc}}\right)^2 \left(\frac{S}{\rm Jy\,Hz}\right), \tag{4.3}$$

here $M_{\rm HI}$ is the H I mass, $h_{\rm C}$ is taken to be ≈ 1 (by assuming $C = H_0 = 67.7\,{\rm km\,s^{-1}\,Mpc^{-1}}$ in Eq 4.2, see Section 1.4 for assumed cosmological values.), and D_L is the luminosity distance.

For group galaxies we calculate the H I mass using Eq 4.3, where we obtain the flux from the sum of the integrated flux in the moment 0 maps of the galaxies. The uncertainties of the H I masses are estimated by using the per channel $\sigma_{\rm rms}$ and is found to be 1.9×10^7 M$_\odot$ thus we report masses in Table 4.2 with a typical uncertainty of ~ 0.019 dex for the average galaxy. The indicative uncertainties for H I masses are then as follows: $\log(M_{\rm HI}/{\rm M_\odot}) = \log(M_{\rm HI} \pm 0.019/{\rm M_\odot})$.

4.3.2 Stellar mass and SFR

To estimate individual galaxy star formation rates and stellar masses (M_*) we make use of NASA's Wide-field Infrared Survey Explorer (WISE, Wright et al., 2010) All-Sky catalogue data. In 2010 WISE mapped the full sky at mid-infrared wavelengths of 3.4, 4.6, 12, and 22 μm with the respective bands commonly referred to as W1, W2, W3, and W4. The bands have angular resolutions of 6.1", 6.4", 6.5", and 12.0" and achieve 5σ point source sensitivities of at least 0.08, 0.11, 1 and 6 mJy, with

sensitivity improving nearer to the ecliptic poles. WISE provides catalogue data for sources in multiple aperture sizes ranging from 5.5" to 24.75" for bands W1, W2, and W3.

The W1 and W2 bands are sensitive to evolved stellar population and are useful for estimating the stellar mass of a galaxy (Cluver et al., 2014). The W3 band is sensitive to polycyclic aromatic hydrocarbons and can be used to estimate star formation rate.

The cross-matching process was executed as follows: We cross-matched the coordinates of the flux weighted centroid of the H I galaxy from the SoFiA 2 catalogue with the mid-infrared source coordinates in the WISE All-Sky catalogue. The results were then manually inspected in each WISE band. In cases where there is foreground star contamination, we exclude the galaxy from M_* and/or SFR calculation based on which band was contaminated. When there is no clear match in the WISE catalogue, we use the sensitivity of the individual bands to obtain upper limits for M_* and SFR by assuming the flux of the galaxy is less than 3 times the sensitivity of the band in question. If the cross-matching was successful in finding a WISE counterpart, we first inspect the `ext_flg` parameter, if the galaxy is extended (`ext_flg` > 0) then the largest, non-contaminated aperture is then used to determine a Vega magnitude of the source using the catalogue. If the galaxy is not extended (`ext_flg` = 0), we use the 11 arcsecond aperture. Finally, the contamination flag parameter (eg. `w1flg_3` for the W1 11 arcsecond aperture) for each band is inspected for potential contamination. If possible contamination from other sources is present we have noted it with an *, and if the parameter suggests an upper limit we have quoted the provided upper limit, signified with "<". The results are shown in Table 4.2.

For the M_* calculation we use Equation 1 from Cluver et al. (2014), the W1 and W2 Vega magnitudes are read from the appropriately chosen aperture. These magnitudes are then used in as follows to calculate the stellar mass:

$$\log_{10} M_*/L_{\mathrm{W1}} = -2.54(\mathrm{W}_{3.4\mu m} - \mathrm{W}_{4,6\mu m}) - 0.17 \tag{4.4}$$

$$L_{\mathrm{W1}}(L_\odot) = 10^{-0.4(Mag - \mathrm{Mag}_{\mathrm{sun}})}, \tag{4.5}$$

where $\mathrm{W}_{3.4\mu m} - \mathrm{W}_{4,6\mu m}$ represents the rest frame colour of the source, Mag is the absolute magnitude of the source in W1, and Mag_{sun} = 3.24.

Cluver et al. (2017) calibrated the WISE W3 12 μm band to star formation rates (SFRs) using the combined sample of the SIRTF Nearby Galaxy Survey (Kennicutt et al., 2003) and Key Insights on Nearby Galaxies: A Far-Infrared Survey with Herschel (Kennicutt et al., 2011). The relation is given in Eq 4.7 where the SFR estimate was calibrated using the total infrared luminosity.

For the SFR calculation, the W3 Vega magnitude of the appropriate aperture is converted into a flux using the method outlined in the WISE data processing photometric calibration documentation[3] using the following:

$$F_\nu(\mathrm{Jy}) = \mathrm{F}_{\nu 0} \times 10^{\left(-\mathrm{m}_{\mathrm{Vega}}/2.5\right)} \tag{4.6}$$

[3]https://wise2.ipac.caltech.edu/docs/release/allsky/expsup/sec4_4h.html

where band-specific values for the $F_{\nu 0}$ are given in the documentation, and F_ν is the flux in Jy. Similarly to Cluver et al. (2017), we subtract 15.8% of the flux in W1 from W3 to account for the older stellar population in the W3 band.

With the newly obtained W3 12 μm flux, we can calculate the 12 μm luminosity, $L_{12\,\mu\mathrm{m}}$. We use then use the following to estimate the SFR of individual galaxies:

$$\log \mathrm{SFM}\ (\mathrm{M}_\odot \mathrm{yr}^{-1}) = (0.889 \pm 0.018)\ \log L_{12\mu\mathrm{m}}(L_\odot) - (7.76 \pm 0.15). \tag{4.7}$$

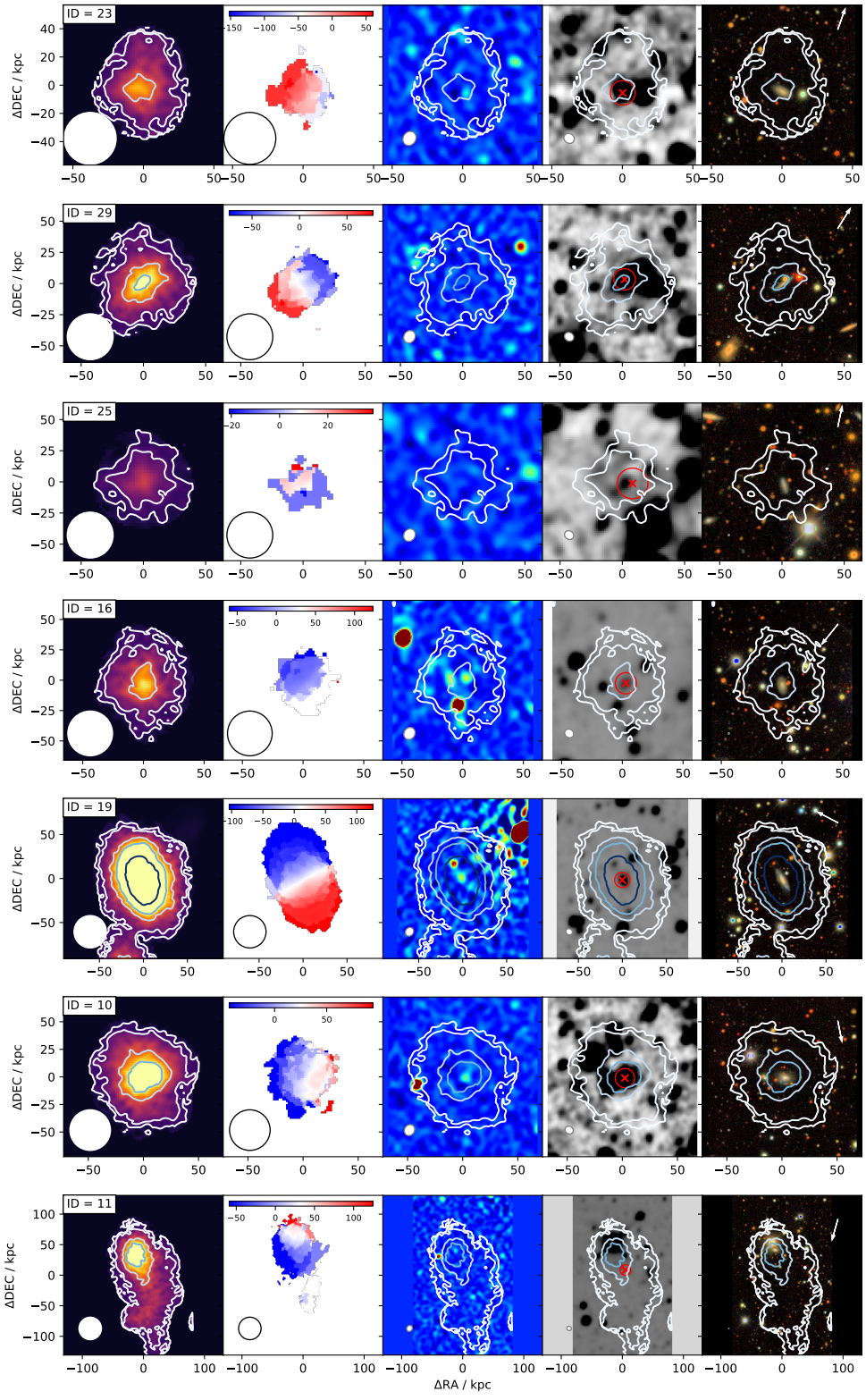


FIGURE 4.8: Individual galaxy group members cutout images in H I, radio continuum, NIR, and optical. Moment 0 (far left), moment 1 (middle left), MGCLS radio continuum (middle), WISE W1 band (middle right), and optical DES RGB image (far right). Each image has the restoring beam plotted in the bottom left and H I contours corresponding to column densities of 0.5×10^{20} cm^{-2}, 1×10^{20} cm^{-2}, 3×10^{20} cm^{-2}, 5×10^{20} cm^{-2}, 10×10^{20} cm^{-2} overlaid. The colourbar in the moment 1 map is in units of km s^{-1}. Red circles in the WISE W1 band show the aperture used for calculations and the red cross is centred on the coordinates of the cross-matched WISE source. The white arrow in the top right of the DES image points to the geometrical centre of the group.

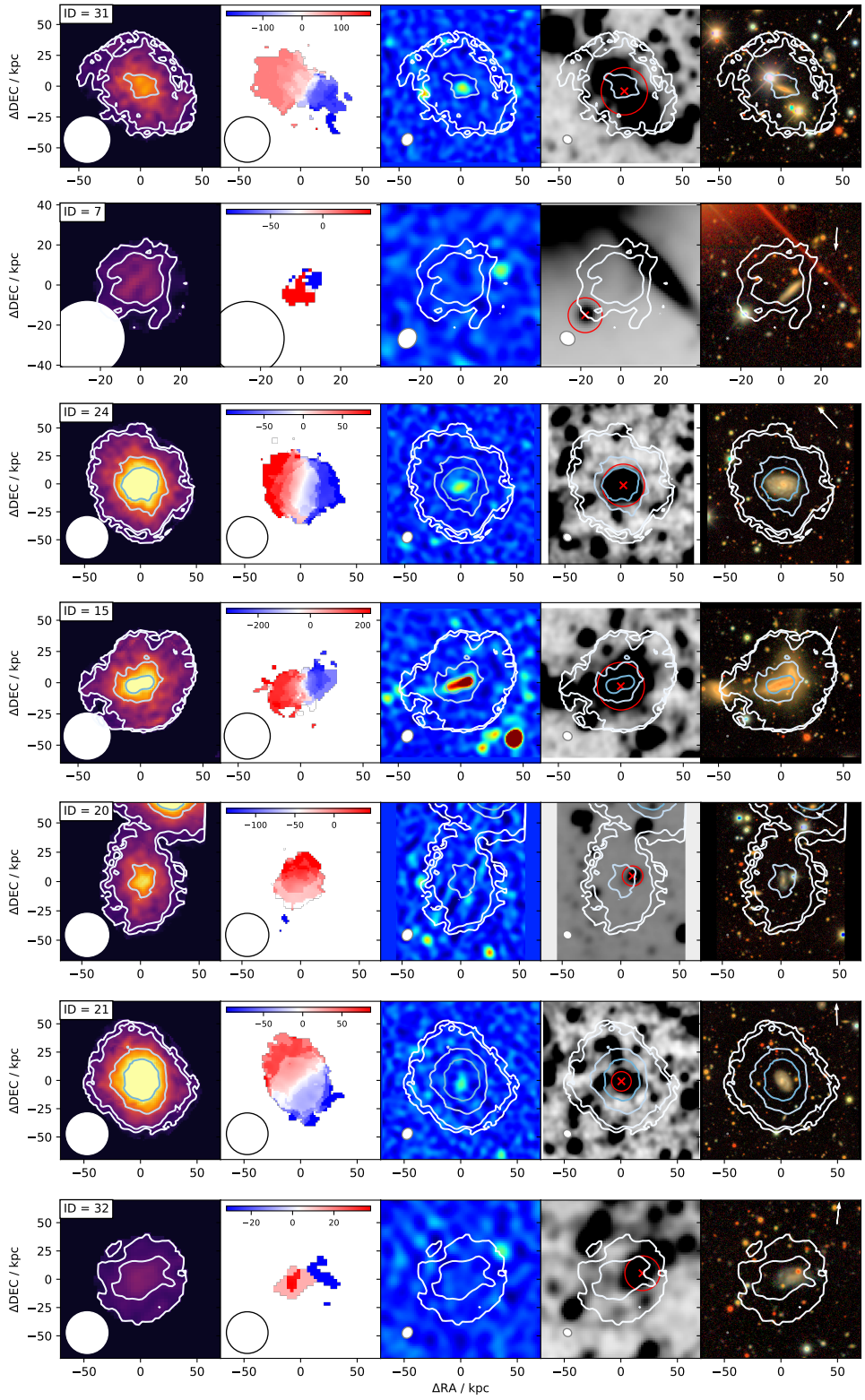


FIGURE 4.9: As per Figure 4.8,

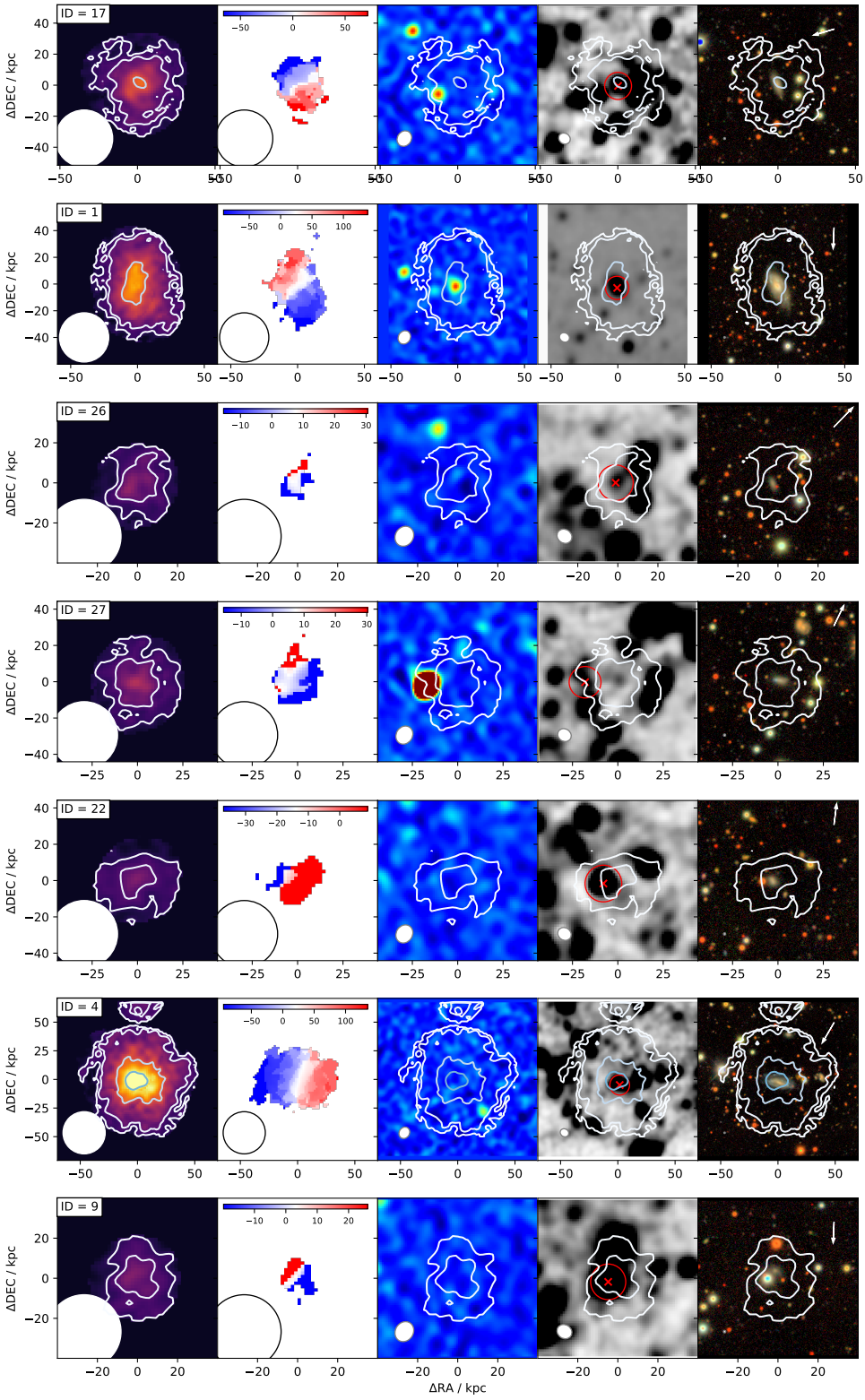


FIGURE 4.10: As per Figure 4.8,

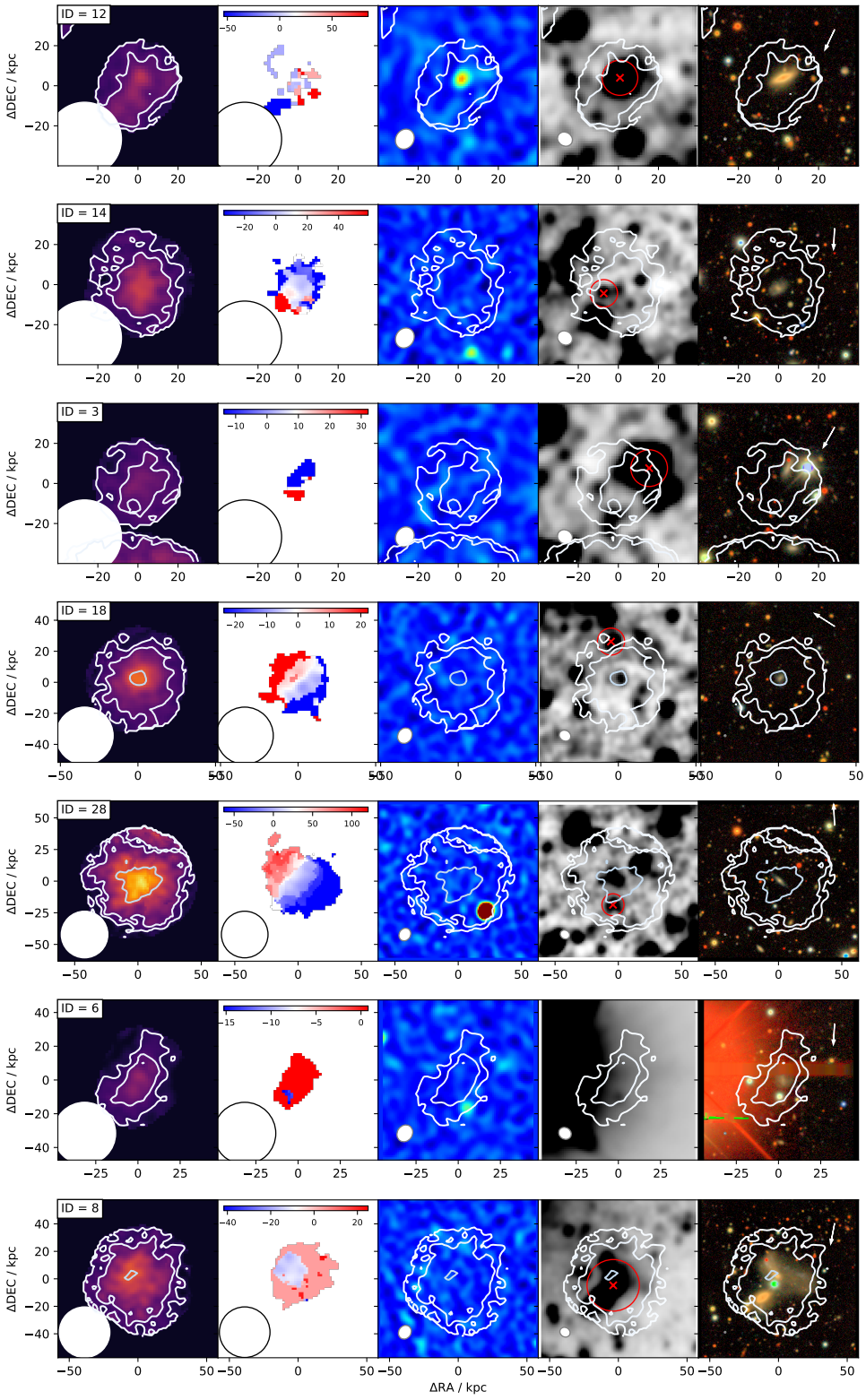


FIGURE 4.11: As per Figure 4.8,

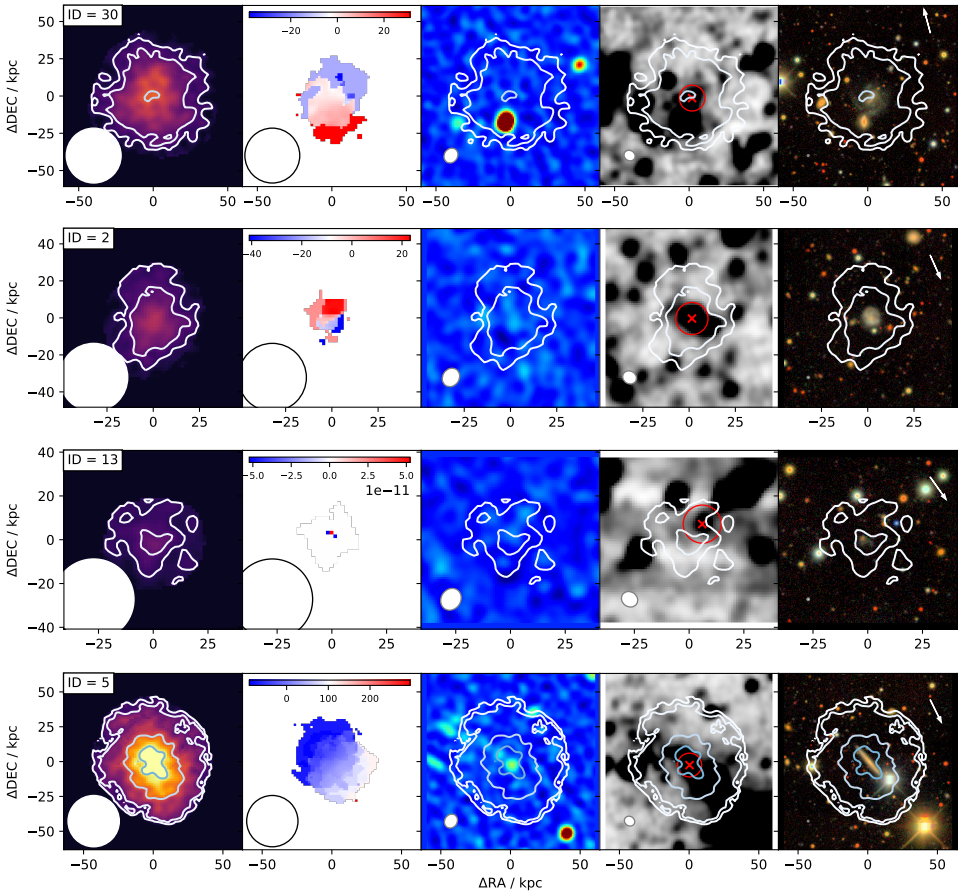


FIGURE 4.12: As per Figure 4.8,

TABLE 4.2: H I catalogue of group galaxies. Columns (2) and (3) give the astronomical location of the H I source from the SOFIA 2 catalogue in units of degrees. Columns (4) and (5) show the H I masses derived from the sum of the flux in the moment 0 map for different cubes. Column (6) gives the width of the spectral line at 50% of the peak flux density from the SOFIA 2 catalogue. Columns (7) and (8) are calculated using the WISE W1, W2, and W3 bands. Column (9) is log of the ratio of (4) and (7).

ID (1)	RA(J2000) (2)	Dec(J2000) (3)	$\log(M_{HI_{rob2}}/M_\odot)$ (4)	$\log(M_{HI_{rob1}}/M_\odot)$ (5)	w50($km\,s^{-1}$) (6)	$\log(M_*/M_\odot)$ (7)	$\log(SFR/M_\odot yr^{-1})$ (8)	$\log(M_{HI}/M_*)$ (9)
1	86.772	-21.186	9.14	9.15	5.467	9.921*	-0.0513*	-0.78*
2	87.072	-21.376	8.60	8.65	1.552	9.930*	<-0.869	-1.32*
3	86.519	-21.459	8.37	-	2.592	-	-	-
4	86.520	-21.482	9.42	9.41	4.872	8.077	-0.833	1.35
5	87.017	-21.529	9.39	9.41	5.002	9.179	-0.672	0.22
6	86.781	-21.545	8.47	8.50	1.176	-	-	-
7	86.783	-21.570	8.44	8.45	3.953	-	-	-
8	86.732	-21.571	9.05	9.06	1.868	-	-	-
9	86.794	-21.681	8.34	8.39	1.667	-	-	-
10	86.858	-21.689	9.50	9.49	3.738	9.933*	-0.713*	-0.43*
11	86.737	-21.707	9.81	9.67	3.475	-	-	-
12	86.703	-21.732	8.48	-	2.812	9.867	-0.646	-1.38
13	86.953	-21.740	8.24	8.23	1.059	<7.052	<0.153	-
14	86.797	-21.777	8.81	8.81	2.343	<7.052	<0.153	-
15	86.745	-21.799	9.34	9.34	12.156	11.049	0.518	-1.70
16	86.712	-21.825	9.15	9.15	2.963	-	-	-
17	86.669	-21.895	8.82	8.84	3.189	7.692*	<-0.611	1.13*
18	86.669	-22.014	8.85	8.86	2.091	<7.052	<0.153	-
19	86.537	-22.062	9.98	9.97	5.830	10.339	-0.311	-0.35
20	86.544	-22.096	9.17	9.15	3.040	-	-	-
21	86.801	-22.110	9.56	9.56	4.032	9.865*	-0.296*	-0.30*
22	86.837	-22.160	8.24	8.31	1.372	-	-	-
23	86.907	-22.197	9.05	9.03	3.928	9.574*	<-0.908	-0.52*
24	86.536	-22.202	9.52	9.49	5.032	10.646	0.342	-1.12
25	86.880	-22.266	8.58	8.62	2.027	-	-	-
26	87.158	-22.269	8.30	8.39	2.473	7.555*	<-0.704	0.75*
27	87.000	-22.303	8.52	8.62	1.875	<7.052	<0.153	-
28	86.788	-22.314	9.25	9.24	4.343	<7.052	<0.153	-
29	87.063	-22.320	9.23	9.22	3.750	-	-	-
30	86.623	-22.548	9.07	9.09	1.667	8.607*	-0.518*	0.47*
31	87.356	-22.601	9.21	9.19	6.533	10.011*	-0.053	-0.80*
32	86.909	-22.820	8.43	8.51	2.000	-	-	-

[1] Galaxies with potential contamination are indicated by "*".
[2] Upper limits are shown by "<".
[3] When no value is present there was foreground star contamination.

Chapter 5

Discussion

In this chapter we analyse results from Chapter 4 and infer properties of the group as well as comparing them to well know relations. Section 5.1 discusses and compares the H I and stellar properties of the group. Individual galaxies are studied in a qualitative way in Section 5.2, through visual inspection of galaxies from a multi-wavelength approach. Section 5.3 summarises the primary properties of the group. In Section 5.4 we speculate about where this group fits into the holistic picture of the LSS of the universe while addressing the future work that needs to be done to better understand this structure and others like it. Finally, in Section 5.5 we bring to light a previous serendipitous discovery by MeerKAT and also the power of MeerKAT continuum surveys for H I science.

5.1 Scaling relations

In Figure 5.1, we show the H I distribution of the 32 galaxies that pass our group membership criteria. All galaxies fall within the $8 < \log(M_{HI}/M_{\odot}) < 10$ range. When considering the HIMF determined by Jones et al. (2018) who find the 'knee' of the function to be at 9.94 ± 0.01 $\log(M_{HI}/M_{\odot})$ the sample contains no extreme outliers regardless of the cube used to calculate the H I mass, see values in Table 4.2.

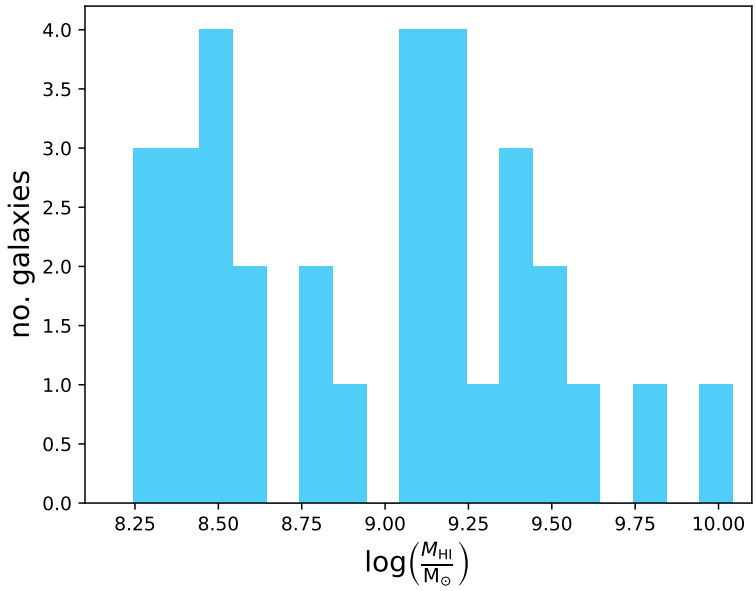


FIGURE 5.1: H I mass distribution of group galaxies from the ROBUST 2 cube.

In Figure 5.2 we compare H I masses derived using the Briggs weighted ROBUST 1 cube versus that of the values obtained from the ROBUST 2 cube. Both masses were calculated by summing the flux in the moment 0 map of a source. We see very good agreement as expected, the Pearson correlation coefficient for the relation is

$\rho = 0.9975$. The outlier on the relation is ID 11 and is due to more of the tail being recovered in the ROBUST 2 cube as a result of higher column density sensitivity, this leads to more flux being incorporated into the sum in the H I mass calculation when using the ROBUST 2 cube.

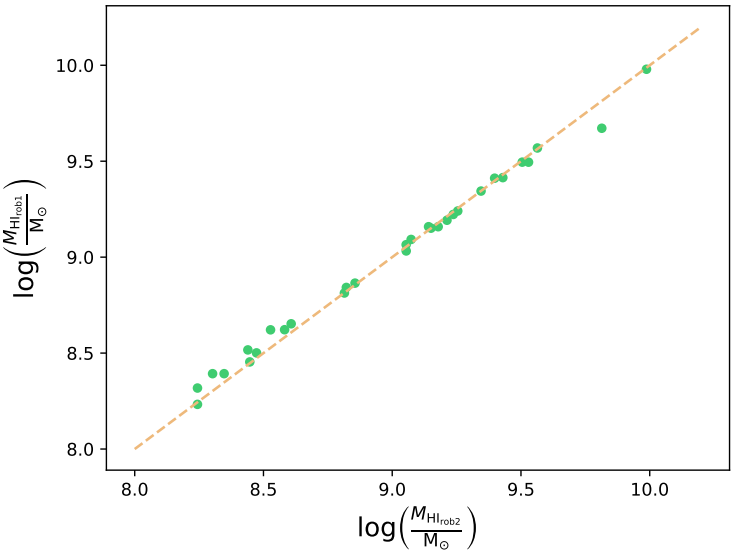


FIGURE 5.2: H I mass comparison between Briggs ROBUST 1 and BRIGGS ROBUST 2 cubes. The orange dashed line is the 1-to-1 relation.

To investigate the relationship between the H I diameter (D_{HI}) and the H I mass, which is an important relation to probe the gas accretion history of galaxies, we compare the sample to Wang et al. (2016). In Figure 5.3 the Wang et al. (2016) sample is shown with the solid orange line, and the 3σ confidence intervals are given by the dashed lines. In this work the H I diameter is taken to be the semi-major axis of the ellipse fitted to the source at 3 times the local RMS determined during source finding by SOFIA 2. The H I mass was determined by summing the flux associated with the source in the individual galaxy cutout moment 0 map. For both the diameter and the H I mass values we used the ROBUST 1 weighted cube. All but 6 sources are within 3σ of Wang et al. (2016) and all galaxies in the sample are above the average value of the relation. It is important to note the difference in definition of the H I diameter between the method used in Wang et al. (2016) and this work. Wang et al. (2016) calculates the H I diameter by taking the semi-major axis of an ellipse fitted to a detection at H I density levels $> 1\,\mathrm{M}_\odot\,\mathrm{pc}^{-1} = 1.249 \times 10^{20}\,\mathrm{cm}^{-2}$. This means that often the full H I extent of the galaxy does not fall within D_{HI}. In contrast, we define D_{HI} at an H I column density of $\sim 1.5 \times 10^{19}\,\mathrm{cm}^{-2}$ calculated using the per channel RMS. In this way we are overestimating D_{HI} when compared to Wang et al. (2016). Upon manual inspection, 4 of the sources outside of the relation are low H I flux detections and would thus likely have a smaller D_{HI} if calculated as in Wang et al. (2016). The two major outliers at H I mass of $\sim 8.13\,\mathrm{M}_\odot$ and $\sim 9.67\,\mathrm{M}_\odot$ correspond to IDs 22 and 11 respectively. ID 11 has clear ram pressure stripping which results in an extension of the semi-major axis, reflected in the plot. Similarly to the 4 minor outliers close to the 3σ upper limit seen in Figure 5.3, ID 22 is a weak detection with low H I flux. Several of these galaxies are also clearly involved in an interaction, which could also bias results. Note that we follow the approach in Ranchod et al. (2021) to estimate the D_{HI} uncertainty, that is we approximate it as the physical size corresponding to the angular size of half the semi-major axes of the restoring beam. The indicative D_{HI} uncertainty is found to be ~ 10 kpc. In future work we plan to compare to Wang et al. (2016) again with D_{HI} defined in a consistent way, this will be done by ellipse fitting manually to enable better control over the D_{HI} defining

criteria. To improve accuracy we would perform this study with a ROBUST 0 cube to attempt to retain angular resolution and thereby minimise D_{HI} uncertainties.

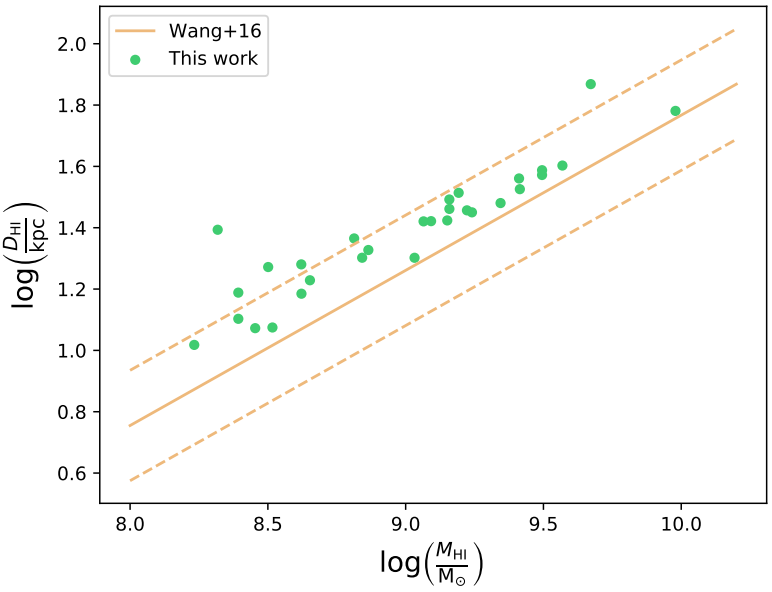


FIGURE 5.3: H I diameter as a function of H I mass (both from the ROBUST 1 cube). Green dots are galaxies from the sample in this work. The orange solid line indicates the relation found by Wang et al. (2016) (with D_{HI} defined at higher H I column density) with the dashed lines showing the 3σ confidence intervals. Uncertainties are 0.019 dex for M_{HI} and 10 kpc for D_{HI}.

Following the method outlined in Section 4.3 to calculate the stellar mass and the usual flux sum to calculate the H I mass, we plot the H I mass as a function of stellar mass in Figure 5.4. For this plot we use H I masses derived from the ROBUST 2 cube. The orange solid line shows the Parkash et al. (2018) relation and the dashed lines represent the 3σ confidence intervals. Upper limits are given by blue arrows (these are either non-detections or were stated as upper limits in the WISE catalogue), purple dots are sources that were flagged as potentially contaminated in the WISE catalogue but seemed reasonably uncontaminated during manual inspection, green stars are uncontaminated sources. Sources that were mismatched or clearly contaminated/dominated were excluded for this relation. All source in our sample fall within the 3σ range of the Parkash et al. (2018) relation.

Figure 5.5 plots the star formation rate as a function of the stellar mass of the galaxies within the sample. Section 4.3 briefly discusses the method used to calculate the SFR from the WISE W3 band. We have omitted galaxies that have been contaminated/dominated in either SFR or stellar mass. Additionally, we have not included any upper limit/non-detection galaxies. Again we compare to Parkash et al. (2018) and the 3σ limits thereof. From the 15 galaxies plotted, 2 galaxies find themselves above the 3σ limit. Both galaxies are potentially contaminated, this could be the reason for the increase in SFR as excess flux from nearby unassociated sources could have been erroneously included in the calculation.

We investigate the relationship between a galaxy's location within the group to the gas-to-stars ratio, $\log\left(\frac{M_{\mathrm{HI}}}{M_*}\right)$, of the galaxy in Figure 5.6. Red circles indicate galaxies with potentially contaminated M_* values from Table 4.2. Figure 5.6 highlights the large range of gas-to-stars ratio values present in the group, from -1.70 to 1.35. There appears to be no clear correlation between the projected distance to the geometric

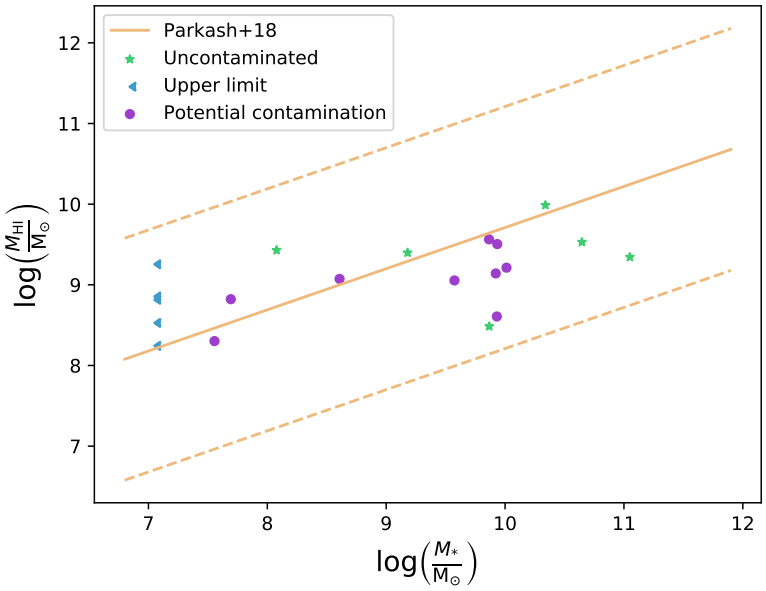


FIGURE 5.4: H I mass (ROBUST 2) as a function of stellar mass (M_*). The blue arrows are indicative of upper limits and obtained from non-detections or flagged as such in the WISE catalogue. Green stars are clean detections in the WISE map and catalogue. Purple circles are detections that appeared to be fairly free from contamination during manual inspection but were flagged as potentially contaminated in the WISE catalogue. The solid orange line represents the relation found by Parkash et al. (2018) with the 3σ confidence levels given by the dashed lines.

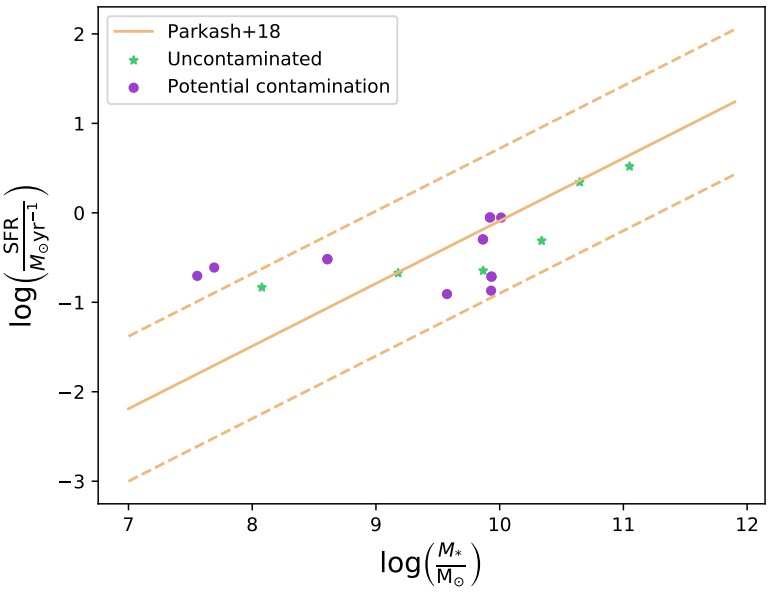


FIGURE 5.5: SFR as a function of stellar mass. Green stars are uncontaminated detections and purple circles are detections flagged as potentially contaminated by WISE but appeared uncontaminated during manual inspection. The solid orange line represents the relation found by Parkash et al. (2018) and the dashed lines show the 3σ confidence levels thereof.

centre of the group and the gas-to-stars ratio. This study could be further improved by adding the spectral dimension to the study.

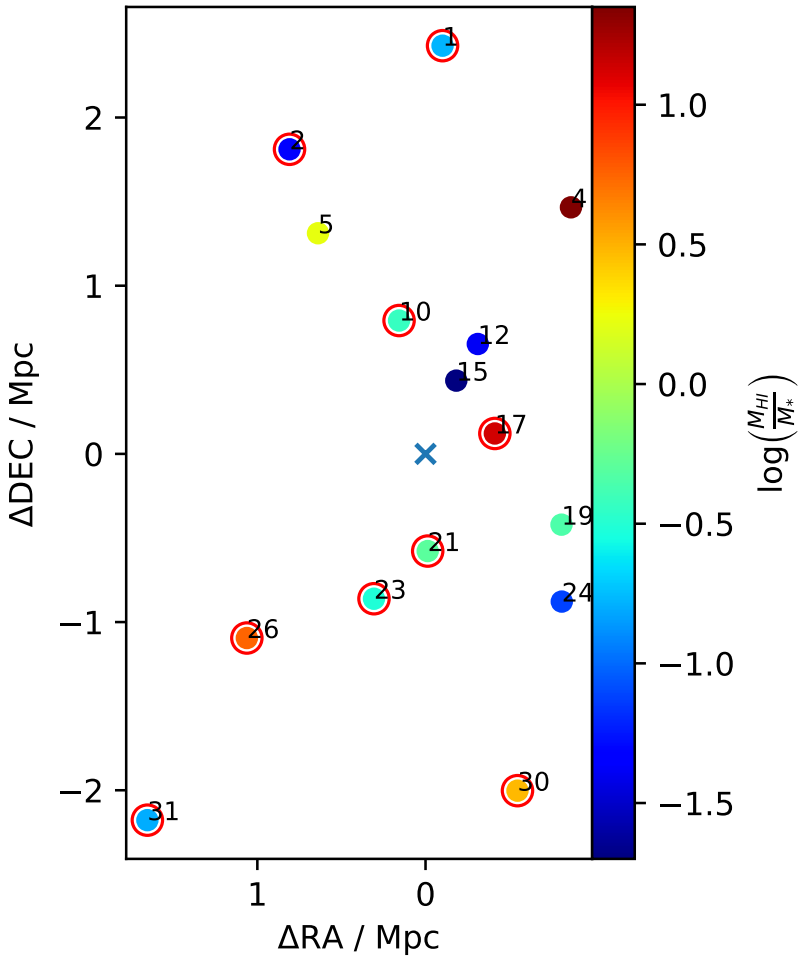


FIGURE 5.6: The gas-to-stars ratio, $\log\left(\frac{M_{\rm HI}}{M_*}\right)$, of galaxies is given on the coloraxis while galaxies are plotted on their projected location. Red circles indicate galaxies with potentially contaminated M_* values. The geometric centre of the group is given by the blue cross.

5.2 Individual galaxy analysis

In Table 5.1 we summarise some of the properties and characteristics of galaxies in the group. The "?" on IDs 3 and 4 interaction column brings attention to the small distance between them as well as the asymmetry of ID 3's moment 1 map. The H I content could be interacting at a column density below our sensitivity threshold. Note that the description given in the WISE W1 column is independent of the criteria used to calculate stellar mass, for an explanation on the use of different apertures and flags to calculate SFR and stellar mass see Subsection 4.3.2. Table 5.1 Many galaxies have unclear optical images and/or H I velocity profiles, finer spectral resolution is needed to more accurately map the kinematics of these galaxies and thus more confidently classify galaxy H I velocity profiles.

TABLE 5.1: Individual galaxy properties from visual inspection of the H I moment 1 map, H I spectrum, MGCLS 1.28 GHz radio continuum, WISE W1 band, and DES RGB image.

ID	H I velocity profile	Radio continuum	WISE W1 counterpart	Optical morphology	Interactions	Ram pressure stripping
1	double horn	point	yes	disk	-	-
2	single	-	yes	disk	-	-
3	single	-	contaminated	disk	yes(?)	-
4	double horn	-	yes	disk	yes(?)	-
5	double horn	point	contaminated	disk	-	-
6	single	-	contaminated	unclear	-	-
7	double horn	-	contaminated	disk	-	-
8	single	-	contaminated	interacting disks	yes	-
9	single	-	contaminated	unclear	-	-
10	single	point	yes	disk	-	-
11	asymmetrical	-	contaminated	unclear	-	yes
12	single	point	yes	disk	-	-
13	single	-	unclear	unclear	-	-
14	single	-	yes	disk	-	-
15	double horn	extended	contaminated	disk	yes	-
16	double horn	point	yes	disk	-	-
17	single	-	yes	disk	-	-
18	single	-	yes	disk	-	-
19	double horn	point	yes	disk	yes	-
20	single	-	contaminated	disk	yes	-
21	double horn	point	yes	disk	-	-
22	single	-	unclear	unclear	-	-
23	double horn	-	yes	disk	-	-
24	double horn	extended	yes	disk	-	-
25	single	-	yes	unclear	-	-
26	single	-	unclear	unclear	-	-
27	single	-	unclear	unclear	-	-
28	double horn	-	yes	disk	-	-
29	double horn	-	contaminated	disk	-	-
30	single	-	contaminated	disk	-	-
31	asymmetrical	point	contaminated	disk	-	-
32	single	-	contaminated	disk	-	-

From comparison with the DES images we see that, as expected, the H I extent far exceeds that of the optical extent. This is particularly clear in the case of IDs 19, 21, and 24, just to name a few of the many examples. While optical extents were not specifically measured, together with the DES images, H I moment 0 maps show that the PSF-convolved H I extent is often 3-4 times the size of the optical galaxy extent.

IDs 8, 11, 15, and the ID 19 and 20 system, are all interesting sources for various reasons which we now discuss:

ID 8 has no continuum emission and no clear velocity gradient is present in the H I moment 1 map, see Figure 4.11. The WISE W1 map is contaminated by a foreground star identifiable in the DES image. The flux peak in the H I moment 0 map corresponds to a slightly offset optical galaxy directly above the foreground star in the DES image. This optical counterpart appears to be embedded in an envelope of diffuse stellar emission extending to the east. There is another optical galaxy present in the southwest of the DES image that looks to also be connected to the aforementioned diffuse stellar emission. If this is an interacting system we expect to see more H I emission associated with the galaxy to the southwest that does not seem to be present in the H I moment 0 map. It is unclear whether or not these galaxies are interacting or if the optical galaxy to the southwest is a foreground galaxy. Better angular resolution could assist in clarifying the system. Unfortunately the signal-to-noise in the ROBUST 0 map is not sufficient to detect any H I emission to the southwest, see figure in Appendix A.

ID 11 showcases what is thought to be significant ram pressure stripping, see Figure 4.8. The H I tail to the south could be caused by the pressure of the IG_rM on the cold gas within the galaxy as it moves through the group, referred to as ram pressure stripping. Importantly this galaxy is ~ 0.71 Mpc from the centre of the group, which is relatively close when compared to other group galaxies, see Figure 4.4 where the red cross is the geometric centre of the group. Unfortunately, the foreground star detected in DES limits the information that can be extracted from the DES and WISE data about morphology and stellar properties respectively. The tail is large, extending ~ 90 kpc beyond the expected H I extent, which is larger than the full H I extent of many other galaxies in the group. While the gradient in the moment 1 map is largely unresolved, the H I spectrum is bright and seems fairly undisturbed.

The moment 1 map of ID 15, see Figure 4.9, shows a clear rotation with an exceptionally large velocity width, this is reflected in the *w50* measurement being the highest of the sample at 559 km s^{-1}. The DES image shows two optical galaxies, the central one is well aligned with the H I contours and is thought to be the primary optical counterpart. There is strong extended radio continuum emission that coincides with the H I moment 0 map flux weighted centroid. The H I spectrum shows an extended velocity width that could be either due to interaction between two galaxies resulting in a bimodal distribution or a large double horn profile of one galaxy. The source having the largest stellar mass and star formation comes as no surprise as the aperture used to calculate the SFR and stellar mass captures excess NIR emission from the additional galaxy, be it interacting or background. Despite these high values, the source still lies well within the Parkash et al. (2018) relations for both the stellar mass and the star formation rate. If this was an interacting system we would expect the galaxies to be close in frequency space and thus to see additional H I emission in the northeast, however, our angular resolution could be a limiting factor in identifying this emission as the source is unresolved. It is not clear if this is an interacting system or simply a galaxy with an exceptionally large velocity width and an optical galaxy in the background that inflates the stellar mass, better spectral and angular resolution would be needed to further investigate this source.

In the case of ID 19 and 20, there is an overlap in the H I extent shown in the H I moment 0 maps, on the contrary, the optical counterparts are distinctly separate, see Figure 4.8 and Figure 4.9. ID 19 has a clear WISE counterpart in W1, W2, and W3 and a hint of emission in the radio continuum. The moment 1 map is consistent with rotation associated with a large edge-on spiral disk galaxy, and the source has the third largest w50 measurement of all the sources. Additionally, we note that the source has the second highest stellar mass within the sample. On the other hand, ID 20 shows no clear continuum emission or WISE counterpart. During crossmatching only the bright star was found near the source, contaminating any emission that would have been associated with the source. The moment 1 map of ID 20 appears to have an asymmetrical rotation curve. ID 19 has a clear and symmetrical double horn profile. Taking all of this into consideration, this system could potentially be in the early stages of galaxy interaction between galaxies 19 and 20. This is a prime example of H I being a far superior tracer of early interactions when compared to optical wavelengths.

5.3 Group properties

In this section we summarise some important H I properties of the group as a whole. The group was serendipitously discovered at a geometric mean of RA = 05h47m14s and Dec = −21d56m24s at $z = 0.041$ with a corresponding central frequency of $\sim$ 1.3641 MHz. There are 32 galaxy members after applying group membership criteria. Of the the 32 group members, 4 are involved in interactions and 1 is undergoing ram pressure stripping. The sum of the H I mass of all members equates to $\sim 5.2 \times 10^{10}\,\mathrm{M}_\odot$ or $\log(M_{\mathrm{HI}}/\mathrm{M}_\odot) = 10.716$. The average H I mass and H I velocity profile *w50* of galaxies in the group are $\sim 1.6 \times 10^{9}\,\mathrm{M}_\odot$ or $\log(M_{\mathrm{HI}}/\mathrm{M}_\odot) = 9.20$ and $\sim 160\,\mathrm{km\,s^{-1}}$respectively. The full velocity width of the group is $\sim 1860\,\mathrm{km\,s^{-1}}$. The group appears to have a filamentary structure running approximately from north to south and spanning 5.33 Mpc from the northernmost to the southernmost galaxy.

5.4 Classification of group structure

The projected linear structure that can clearly be observed running down from north to south is not characteristic of galaxy groups. Figure 4.4 provides us with an illustration of the easily discernibly linear filamentary shape that the group appears to have. This is reminiscent of the massive filaments present in the large-scale structure of the universe, albeit at a much smaller scale. The filaments and walls located in the LSS of the universe span $60 - 100\,h^{-1}$ Mpc whereas this filamentary group is as a scale of $\sim$ 5 Mpc.

The tendrils discussed in Subsection 1.2.5 have been a topic of recent debate. This filamentary-like group has a separation length of 5.33 Mpc between the northernmost galaxy and the southernmost galaxy, which places it in a somewhat similar spatial range as the $10\,h^{-1}$ Mpc average length for tendrils (Alpaslan et al., 2014). In contrast to tendrils that generally have $\sim$ 6 galaxies, the discovered group has 32 members. Tendrils were initially found in the redshift range of $0.15 < z < 0.2$ (Alpaslan et al., 2014) then later studied in the redshift range of $0.015 < z < 0.05$ (Crone Odekon et al., 2018). The group reported in this thesis is a $z = 0.041$, putting it in the range studied by Crone Odekon et al. (2018). The spatial properties of this group, together with the number of galaxies in the structure, places the group in an intermediate classification with the spatial extent and shape potentially representing that of a tendril but a density that more closely represents that of a group or a cluster. We do not explicitly calculate the density in this work as is done in Crone Odekon et al. (2018). However, it is clear that there are more galaxies within this structure than in the average tendril. The intermediate nature of this structure makes it an

interesting structure to investigate. Some of the investigations that would lead to a better understanding of the structure includes the H I deficiency of the galaxies, dynamical mass estimates, dynamical modeling, and kinematic axis alignment with the filamentary structure. However, these studies are not included in the scope of the thesis and are left for future work.

The galaxy spin axis alignment to associated filaments is one of our primary goals for future work. This was investigated by Tudorache et al. (2022) using 77 H I selected galaxies from MeerKAT International GigaHertz Tiered Extragalactic Exploration (MIGHTEE, Jarvis et al., 2016) which provides them with a larger sample size than (Blue Bird et al., 2020), as well as having sufficient resolution to kinematically resolve many sources (in contrast to Kleiner et al. (2017) and Crone Odekon et al. (2018)). Tudorache et al. (2022) uses The Discrete Persistent Structure Extractor (DisPerSE, Sousbie, 2011) to map the cosmic web. They find that galaxies tend to be more aligned when closer to filaments ($d < 5$ Mpc) when compared to galaxies that are further away ($5 < d < 10$ Mpc). Additionally, they find that lower gas-to-stars ratio galaxies ($\log(M_{HI}/M_*) < 0.11$) tend to be more aligned than galaxies with a higher gas-to-stars ratio ($\log(M_{HI}/M_*) > 0.11$) (Tudorache et al., 2022). We plan to carry out a similiar study in future work, by ellipse fitting and determining the spin vector of the group galaxies reported in this work by following the methodology carried out in Tudorache et al. (2022), then determining the alignment of the spin vector of the galaxies with the filamentary-like structure. This study could potentially be extended by finding nearby filaments using DisPerSE.

5.5 MeerKAT serendipitous discoveries at $z \sim 0.04$

This group discovery provides us with an excellent demonstration of the capabilities of MeerKAT to probe and identify low redshift gravitationally bound structures such as galaxy groups and clusters. In addition to this, we see the value of MeerKAT as a tool for blind H I searches by utilising L-band surveys such as MGCLS (Knowles et al., 2022) for H I science. This is further reinforced by a similar redshift group of 20 galaxies discovered in the XMM-LSS field by Ranchod et al. (2021) which used the MIGHTEE survey. Finally, this result boasts MeerKAT's ability to resolve $z \sim 0.04$ H I galaxies both spatially and spectrally with an angular resolution of 8" and spectral resolution at a fairly broad channel width of 209 kHz. Given that MGCLS was meant to be a continuum emission only survey, the discovery in this thesis shows the utility of MGCLS and similar MeerKAT surveys as tools for serendipitous discovery and study of galaxy evolution though H I.

Chapter 6

Conclusion

In this work, we report the serendipitous discovery of an H I-rich galaxy group in the foreground of (but gravitationally unconnected to) Abell 3365 at RA = 05h48m12s and Dec = −21d56m03s. The group is at a redshift of $z \sim 0.041$ placing it at a luminosity distance of 187.2 Mpc. Data processing is carried out using OXKAT. We generate three cubes with different ROBUST weightings to serve different science objectives. Source finding is performed on the cubes using SOFIA 2, and the ROBUST 2 cube is used as the primary cube for detection purposes. Thereafter we implement a group membership classification algorithm to have a robust method of determining which galaxies are likely to belong to the group. This approach identifies 32 group members. A manual study of the remaining group galaxies is carried out using multi-band images from the Dark Energy Survey, the Wide-field Infrared Survey Explorer, and the MGCLS 1.28 GHz data. Comparing these images with the H I derived maps such as the moment 0 and moment 1 maps from all cubes to further ensure detections are reliable. H I scaling relations are investigated using moment 0 maps to derive values such as the H I mass and H I diameter, while WISE catalogue data is used to derive the SFR and stellar mass values. The values obtained for our sample are compared to well-established H I and SFR scaling relations. Environmental effects are discussed using interacting systems within the group as well as individual galaxies as examples. This is performed by assessing the H I galaxies using a multiwavelength approach as well as considering the kinematics of the galaxies from the H I velocity fields. Attention is brought to the fact that the group has an unusually large (5.33 Mpc) filamentry-like structure and possibilities of associations with large scale structure such as tendrils are investigated. Other properties such as average and total H I mass and H I velocity width are calculated for the group as a whole. Future work includes dynamical modelling of galaxies that are sufficiently spectrally resolved, SFR estimates from radio continuum to compare to the NIR WISE derived values and lastly, investigation of correlation between galaxy spin axis alignment to the filamentary-like structure. This thesis highlights the capabilities of MeerKAT as a blind H I searching instrument while also contributing to the study of galaxy evolution, and adding to a quickly growing list of serendipitous discoveries by MeerKAT in the low-redshift universe.

Appendix A

ROBUST comparison

In this appendix we present a side-by-side comparison of moment 0 maps generated with different cubes with various ROBUST weightings, this is shown for the 32 galaxy group members.

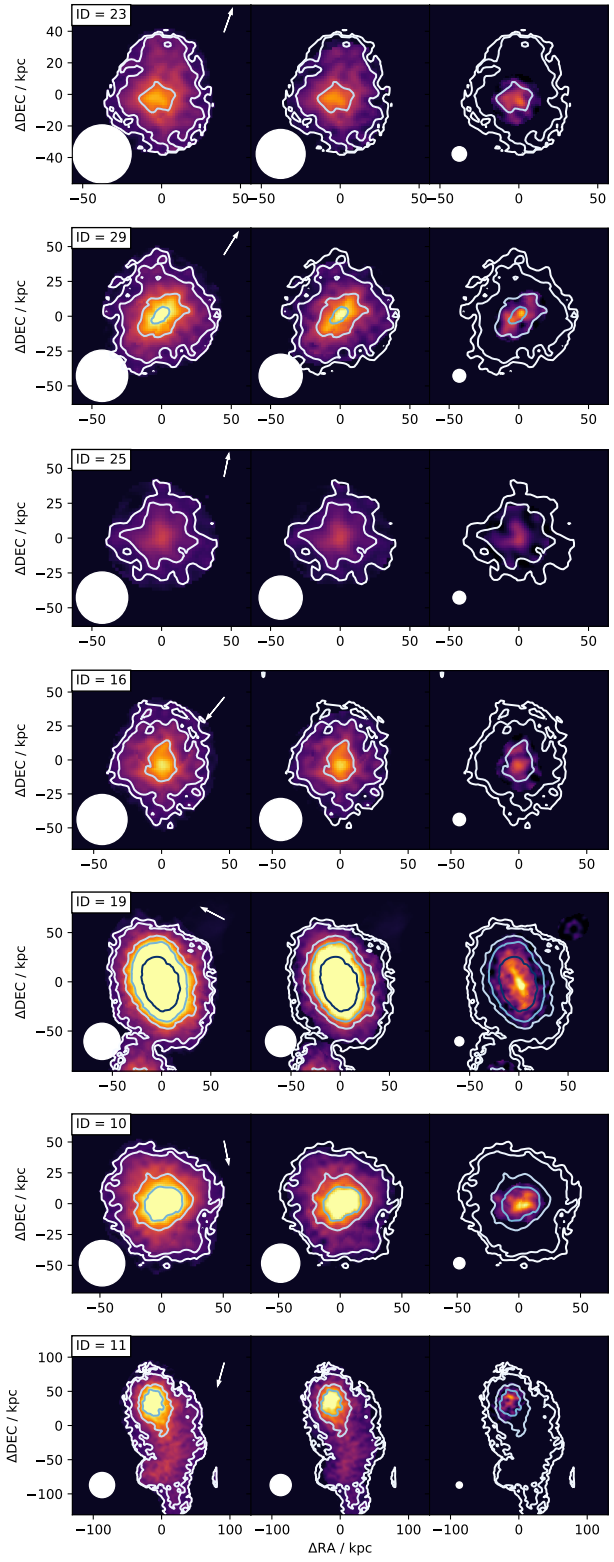


FIGURE A.1: Comparison moment 0 maps generated using different ROBUST weightings: ROBUST 2 (left), ROBUST 1 (middle), and ROBUST 0 (right). The arrow in the left plot points to the geometric mean of the group. The PSF of each weighting is given in the bottom left corner. The contours are the H I contours corresponding to column densities of 0.5×10^{20} cm^{-2}, 1×10^{20} cm^{-2}, 3×10^{20} cm^{-2}, 5×10^{20} cm^{-2}, 10×10^{20} cm^{-2} from the ROBUST 2 cube.

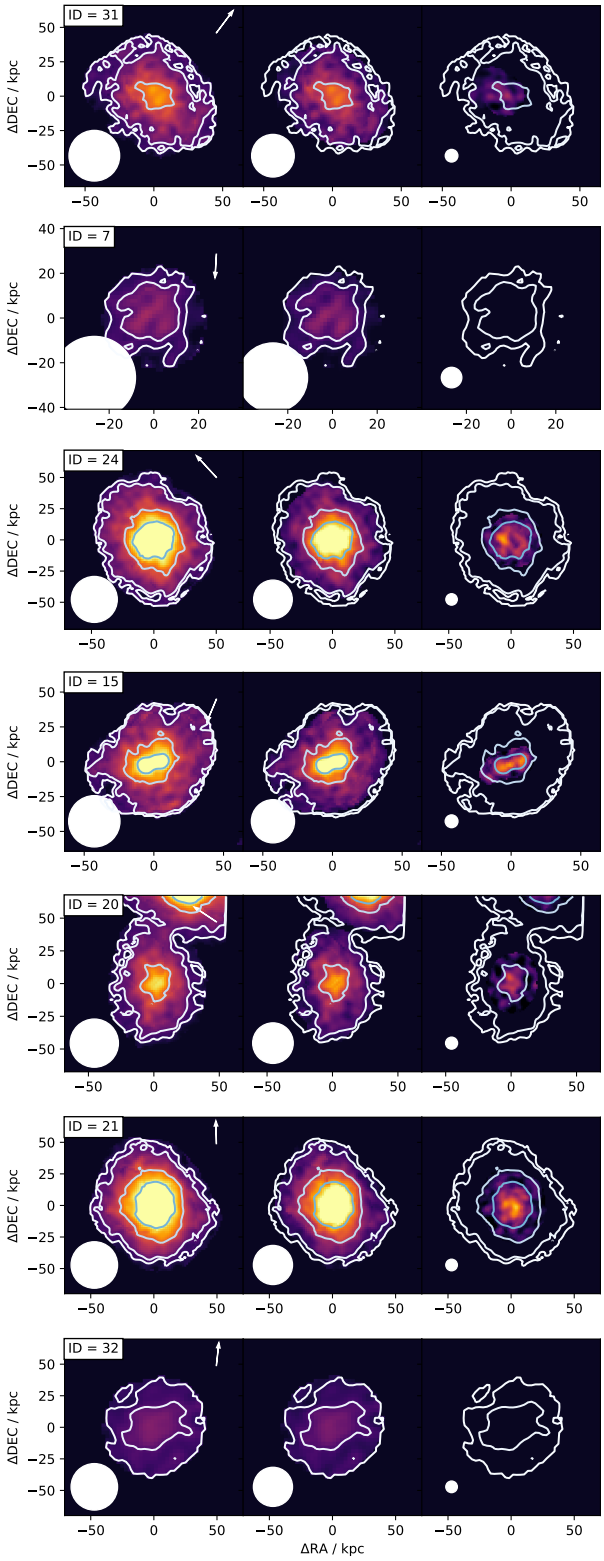


FIGURE A.2: As per Figure A.1

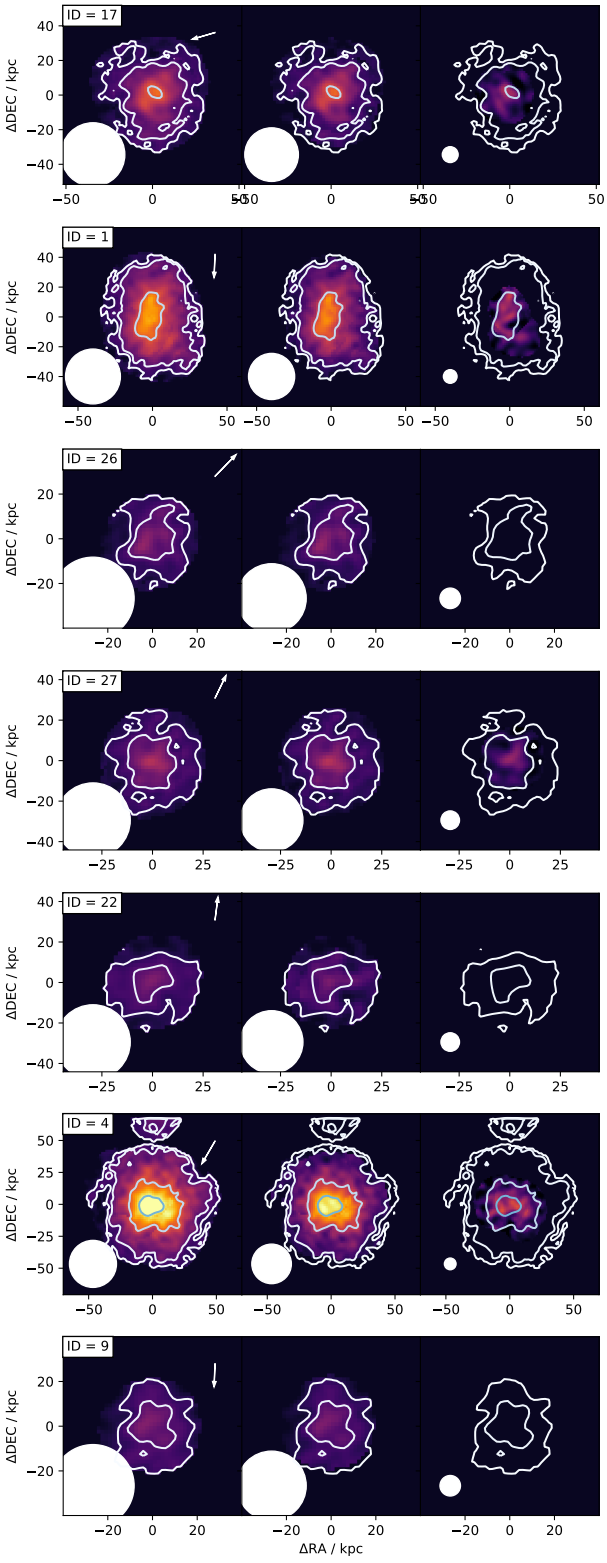


FIGURE A.3: As per Figure A.1

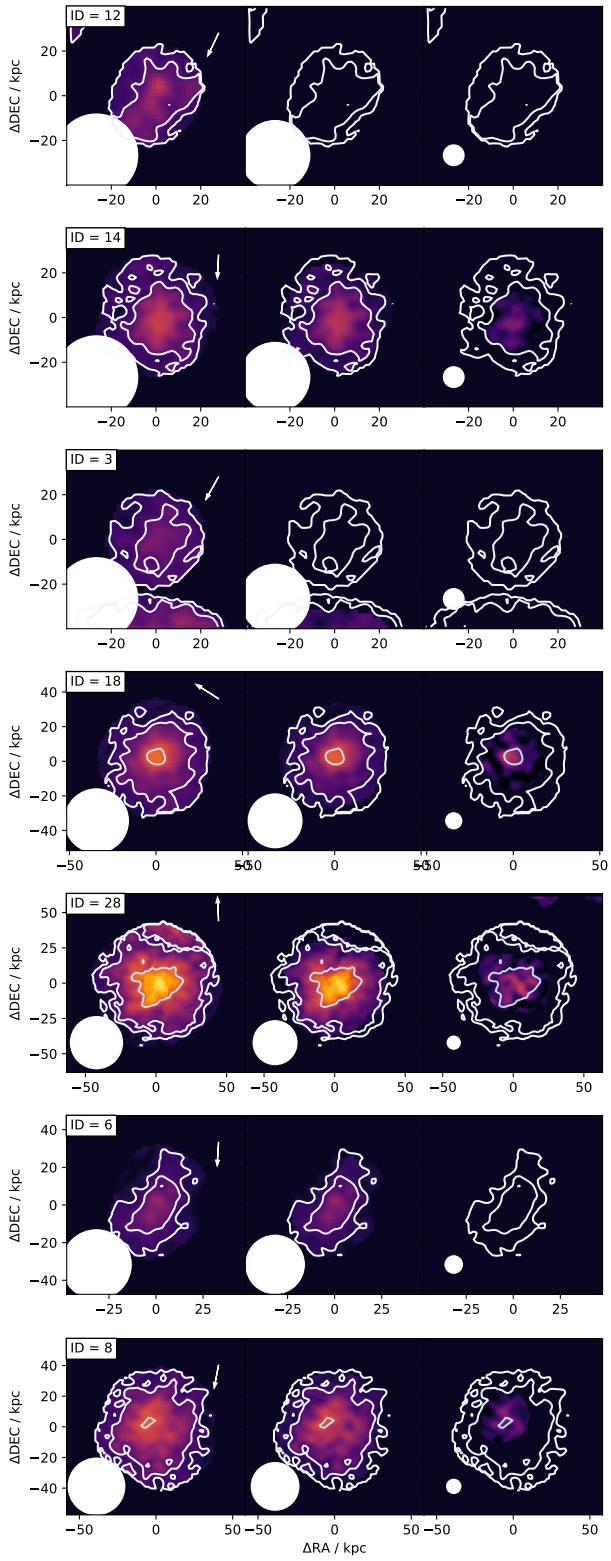


FIGURE A.4: As per Figure A.1

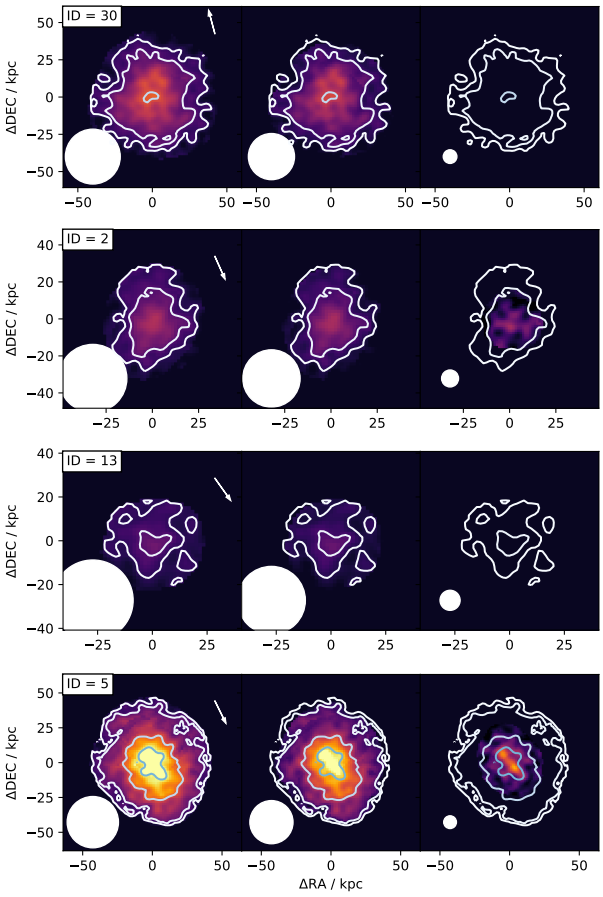


FIGURE A.5: As per Figure A.1

Appendix B

H I spectra

We present the integrated H I spectra for all 32 group galaxies. These spectra were plotted using cubelet integrated H I spectrum text files from running the ROBUST 2 cube through the SOFIA 2 pipeline.

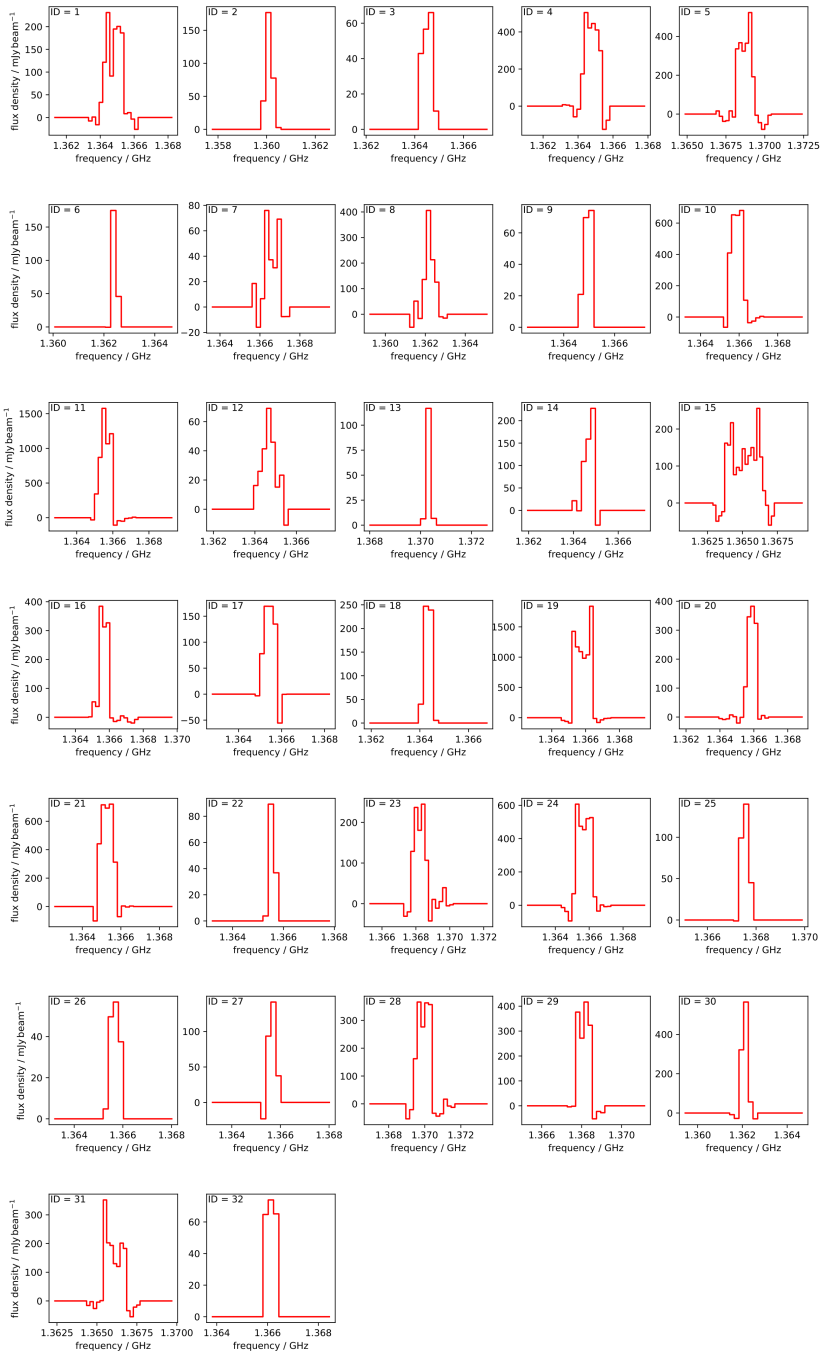


FIGURE B.1: H I spectra for all group galaxies. These spectra were plotted from the cubelet spectrum text files output by SOFIA 2 after source finding using the ROBUST 2 cubes.

Bibliography

Abbott, T. M. C. et al. (2021). "The Dark Energy Survey Data Release 2". In: *The Astrophysical Journal Supplement Series* 255.2, 20, p. 20. DOI: 10.3847/1538-4365/ac00b3. arXiv: 2101.05765 [astro-ph.IM].

Abell, G. O. (1965). "Clustering of Galaxies". In: *Annual Review of Astronomy and Astrophysics* 3, p. 1. DOI: 10.1146/annurev.aa.03.090165.000245.

Abell, George O. (1958). "The Distribution of Rich Clusters of Galaxies." In: *The Astrophysical Journal Supplement Series* 3, p. 211. DOI: 10.1086/190036.

Alpaslan, M. et al. (2014). "Galaxy and Mass Assembly (GAMA): fine filaments of galaxies detected within voids." In: *Monthly Notices of the Royal Astronomical Society* 440, pp. L106–L110. DOI: 10.1093/mnrasl/slu019. arXiv: 1401.7331 [astro-ph.CO].

Aragon Calvo, Miguel A., Mark C. Neyrinck, and Joseph Silk (2019). "Galaxy Quenching from Cosmic Web Detachment". In: *The Open Journal of Astrophysics* 2.1, 7, p. 7. DOI: 10.21105/astro.1697.07881. arXiv: 1607.07881 [astro-ph.GA].

Aragón-Calvo, Miguel A. et al. (2007). "Spin Alignment of Dark Matter Halos in Filaments and Walls". In: *The Astrophysical Journal Letters* 655.1, pp. L5–L8. DOI: 10.1086/511633. arXiv: astro-ph/0610249 [astro-ph].

Bacchini, C. et al. (2019). "The volumetric star formation law in the Milky Way". In: *Astronomy & Astrophysics* 632, A127, A127. DOI: 10.1051/0004-6361/201936559. arXiv: 1911.03480 [astro-ph.GA].

Baker, Andrew J. et al. (2018). "LADUMA: Looking At the Distant Universe with the MeerKAT Array". In: *American Astronomical Society Meeting Abstracts #231*. Vol. 231. American Astronomical Society Meeting Abstracts, 231.07, p. 231.07.

Bautz, L. P. and W. W. Morgan (1970). "On the Classification of the Forms of Clusters of Galaxies". In: *The Astrophysical Journal Letters* 162, p. L149. DOI: 10.1086/180643.

Bharadwaj, Somnath, Suketu P. Bhavsar, and Jatush V. Sheth (2004). "The Size of the Longest Filaments in the Universe". In: *The Astrophysical Journal* 606.1, pp. 25–31. DOI: 10.1086/382140. arXiv: astro-ph/0311342 [astro-ph].

Bigiel, F. et al. (2008). "The Star Formation Law in Nearby Galaxies on Sub-Kpc Scales". In: *The Astronomical Journal* 136.6, pp. 2846–2871. DOI: 10.1088/0004-6256/136/6/2846. arXiv: 0810.2541 [astro-ph].

Blue Bird, J. et al. (2020). "CHILES VI: H I and H α observations for z < 0.1 galaxies; probing H I spin alignment with filaments in the cosmic web". In: *Monthly Notices of the Royal Astronomical Society* 492.1, pp. 153–176. DOI: 10.1093/mnras/stz3357. arXiv: 1912.01062 [astro-ph.GA].

Bond, J. Richard, Lev Kofman, and Dmitry Pogosyan (1996). "How filaments of galaxies are woven into the cosmic web". In: *Nature* 380.6575, pp. 603–606. DOI: 10.1038/380603a0. arXiv: astro-ph/9512141 [astro-ph].

Broeils, A. H. and M. H. Rhee (1997). "Short 21-cm WSRT observations of spiral and irregular galaxies. HI properties." In: *Astronomy & Astrophysics* 324, pp. 877–887.

Burke, Bernard F., Graham, and Peter N. Wilkinson (2019). *An introduction to radio astronomy, 4th edition*.

Butcher, H. and Jr. Oemler A. (1978a). "The evolution of galaxies in clusters. I. ISIT photometry of Cl 0024+1654 and 3C 295." In: *The Astrophysical Journal* 219, pp. 18–30. DOI: 10.1086/155751.

— (1978b). "The evolution of galaxies in clusters. II. The galaxy content of nearby clusters." In: *The Astrophysical Journal* 226, pp. 559–565. DOI: 10.1086/156640.

Cluver, M. E. et al. (2014). "Galaxy and Mass Assembly (GAMA): Mid-infrared Properties and Empirical Relations from WISE". In: *The Astrophysical Journal* 782.2, 90, p. 90. DOI: 10.1088/0004-637X/782/2/90. arXiv: 1401.0837 [astro-ph.GA].

Cluver, M. E. et al. (2017). "Calibrating Star Formation in WISE Using Total Infrared Luminosity". In: *The Astrophysical Journal* 850.1, 68, p. 68. DOI: 10.3847/1538-4357/aa92c7. arXiv: 1710.03469 [astro-ph.GA].

Codis, Sandrine et al. (2012). "Connecting the cosmic web to the spin of dark haloes: implications for galaxy formation". In: *Monthly Notices of the Royal Astronomical Society* 427.4, pp. 3320–3336. DOI: 10.1111/j.1365-2966.2012.21636.x. arXiv: 1201.5794 [astro-ph.CO].

Cortese, L., B. Catinella, and R. Smith (2021). "The Dawes Review 9: The role of cold gas stripping on the star formation quenching of satellite galaxies". In: *Publications of the Astronomical Society of Australia* 38, e035, e035. DOI: 10.1017/pasa.2021.18. arXiv: 2104.02193 [astro-ph.GA].

Crone Odekon, Mary et al. (2018). "The Effect of Filaments and Tendrils on the H I Content of Galaxies". In: *The Astrophysical Journal* 852.2, 142, p. 142. DOI: 10.3847/1538-4357/aaa1e8. arXiv: 1712.05045 [astro-ph.GA].

Daddi, E. et al. (2007). "Multiwavelength Study of Massive Galaxies at z$\sim$2. I. Star Formation and Galaxy Growth". In: *The Astrophysical Journal* 670.1, pp. 156–172. DOI: 10.1086/521818. arXiv: 0705.2831 [astro-ph].

DeBoer, D. R. et al. (2009). "Australian SKA Pathfinder: A High-Dynamic Range Wide-Field of View Survey Telescope". In: *IEEE Proceedings* 97.8, pp. 1507–1521. DOI: 10.1109/JPROC.2009.2016516.

Decarli, Roberto et al. (2019). "The ALMA Spectroscopic Survey in the HUDF: CO Luminosity Functions and the Molecular Gas Content of Galaxies through Cosmic History". In: *The Astrophysical Journal* 882.2, 138, p. 138. DOI: 10.3847/1538-4357/ab30fe. arXiv: 1903.09164 [astro-ph.GA].

Deng, Xin-Fa et al. (2006). "Super-Large-Scale Structures in the Sloan Digital Sky Survey". In: *Chinese Journal of Astronomy and Astrophysics* 6.1, pp. 35–42. DOI: 10.1088/1009-9271/6/1/004.

Dewdney, P. E. et al. (2009). "The Square Kilometre Array". In: *IEEE Proceedings* 97.8, pp. 1482–1496. DOI: 10.1109/JPROC.2009.2021005.

Dressler, A. (1980). "Galaxy morphology in rich clusters: implications for the formation and evolution of galaxies." In: *The Astrophysical Journal* 236, pp. 351–365. DOI: 10.1086/157753.

Dressler, A. and J. E. Gunn (1982). "Spectroscopy of galaxies in distant clusters. I - First results for 3C 295 and 0024 + 1654". In: *The Astrophysical Journal* 263, pp. 533–545. DOI: 10.1086/160524.

Dressler, Alan et al. (1997). "Evolution since z = 0.5 of the Morphology-Density Relation for Clusters of Galaxies". In: *The Astrophysical Journal* 490.2, pp. 577–591. DOI: 10.1086/304890. arXiv: astro-ph/9707232 [astro-ph].

Efstathiou, G., J. R. Bond, and S. D. M. White (1992). "COBE background radiation anisotropies and large-scale structure in the universe". In: *Monthly Notices of the Royal Astronomical Society* 258.1, 1P–6P. DOI: 10.1093/mnras/258.1.1P.

Eggen, O. J., D. Lynden-Bell, and A. R. Sandage (1962). "Evidence from the motions of old stars that the Galaxy collapsed." In: *The Astrophysical Journal* 136, p. 748. DOI: 10.1086/147433.

El-Ad, Hagai and Tsvi Piran (1997). "Voids in the Large-Scale Structure". In: *The Astrophysical Journal* 491.2, pp. 421–435. DOI: 10.1086/304973. arXiv: astro-ph/9702135 [astro-ph].

Elbaz, D. et al. (2007). "The reversal of the star formation-density relation in the distant universe". In: *Astronomy & Astrophysics* 468.1, pp. 33–48. DOI: 10.1051/0004-6361:20077525. arXiv: astro-ph/0703653 [astro-ph].

Feldmann, R., C. M. Carollo, and L. Mayer (2011). "The Hubble Sequence in Groups: The Birth of the Early-type Galaxies". In: *The Astrophysical Journal* 736.2, 88, p. 88. DOI: 10.1088/0004-637X/736/2/88. arXiv: 1008.3386 [astro-ph.CO].

Flöer, L. and B. Winkel (2012). "2D-1D Wavelet Reconstruction as a Tool for Source Finding in Spectroscopic Imaging Surveys". In: *Publications of the Astronomical Society of Australia* 29.3, pp. 244–250. DOI: 10.1071/AS11042. arXiv: 1112.3807 [astro-ph.IM].

For, B. Q. et al. (2019). "WALLABY early science - V. ASKAP H I imaging of the Lyon Group of Galaxies 351". In: *Monthly Notices of the Royal Astronomical Society* 489.4, pp. 5723–5741. DOI: 10.1093/mnras/stz2501.

Geller, M. J. and T. C. Beers (1982). "Substructure within clusters of galaxies." In: *The Publications of the Astronomical Society of the Pacific* 94, pp. 421–439. DOI: 10.1086/131003.

Girardi, Marisa et al. (1998). "Optical Mass Estimates of Galaxy Clusters". In: *The Astrophysical Journal* 505.1, pp. 74–95. DOI: 10.1086/306157. arXiv: astro-ph/9804187 [astro-ph].

Granett, Benjamin R., Mark C. Neyrinck, and István Szapudi (2008). "An Imprint of Superstructures on the Microwave Background due to the Integrated Sachs-Wolfe Effect". In: *The Astrophysical Journal Letters* 683.2, p. L99. DOI: 10.1086/591670. arXiv: 0805.3695 [astro-ph].

Gunn, James E. and III Gott J. Richard (1972). "On the Infall of Matter Into Clusters of Galaxies and Some Effects on Their Evolution". In: *The Astrophysical Journal* 176, p. 1. DOI: 10.1086/151605.

Guth, Alan H. (1981). "Inflationary universe: A possible solution to the horizon and flatness problems". In: *Physical Review D (Particles and Fields)* 23.2, pp. 347–356. DOI: 10.1103/PhysRevD.23.347.

Hamaker, J. P. and J. D. Bregman (1996). "Understanding radio polarimetry. III. Interpreting the IAU/IEEE definitions of the Stokes parameters." In: *Astronomy and Astrophysics Supplement* 117, pp. 161–165.

Heywood, Ian (2020). *oxkat: Semi-automated imaging of MeerKAT observations*. Astrophysics Source Code Library, record ascl:2009.003. ascl: 2009.003.

Horváth, István, Jon Hakkila, and Zsolt Bagoly (2014). "Possible structure in the GRB sky distribution at redshift two". In: *Astronomy & Astrophysics* 561, L12, p. L12. DOI: 10.1051/0004-6361/201323020. arXiv: 1401.0533 [astro-ph.CO].

Huchra, J. P. and M. J. Geller (1982). "Groups of Galaxies. I. Nearby groups". In: *The Astrophysical Journal* 257, pp. 423–437. DOI: 10.1086/160000.

Jarvis, M. et al. (2016). "The MeerKAT International GHz Tiered Extragalactic Exploration (MIGHTEE) Survey". In: *MeerKAT Science: On the Pathway to the SKA*, 6, p. 6. DOI: 10.22323/1.277.0006. arXiv: 1709.01901 [astro-ph.GA].

Jeans, J. H. (1902). "The Stability of a Spherical Nebula". In: *Philosophical Transactions of the Royal Society of London Series A* 199, pp. 1–53. DOI: 10.1098/rsta.1902.0012.

Jonas, J. L. (2009). "MeerKAT - The South African Array With Composite Dishes and Wide-Band Single Pixel Feeds". In: *IEEE Proceedings* 97.8, pp. 1522–1530. DOI: 10.1109/JPROC.2009.2020713.

Jones, Michael G. et al. (2018). "The ALFALFA H I mass function: a dichotomy in the low-mass slope and a locally suppressed 'knee' mass". In: *Monthly Notices of the Royal Astronomical Society* 477.1, pp. 2–17. DOI: 10.1093/mnras/sty521. arXiv: 1802.00053 [astro-ph.GA].

Kennicutt Robert C., Jr. et al. (2003). "SINGS: The SIRTF Nearby Galaxies Survey". In: *The Publications of the Astronomical Society of the Pacific* 115.810, pp. 928–952. DOI: 10.1086/376941. arXiv: astro-ph/0305437 [astro-ph].

Kennicutt, R. C. et al. (2011). "KINGFISH—Key Insights on Nearby Galaxies: A Far-Infrared Survey with Herschel: Survey Description and Image Atlas". In: *The Publications of the Astronomical Society of the Pacific* 123.910, p. 1347. DOI: 10.1086/663818. arXiv: 1111.4438 [astro-ph.CO].

Kenyon, J. S. et al. (2018). "CUBICAL - fast radio interferometric calibration suite exploiting complex optimization". In: *Monthly Notices of the Royal Astronomical Society* 478.2, pp. 2399–2415. DOI: 10.1093/mnras/sty1221. arXiv: 1805.03410 [astro-ph.IM].

Kleiner, Dane et al. (2017). "Evidence for H I replenishment in massive galaxies through gas accretion from the cosmic web". In: *Monthly Notices of the Royal Astronomical Society* 466.4, pp. 4692–4710. DOI: 10.1093/mnras/stw3328. arXiv: 1701.03467 [astro-ph.GA].

Knowles, K. et al. (2022). "The MeerKAT Galaxy Cluster Legacy Survey. I. Survey Overview and Highlights". In: *Astronomy & Astrophysics* 657, A56, A56. DOI: 10.1051/0004-6361/202141488. arXiv: 2111.05673 [astro-ph.GA].

Koribalski, Bärbel S. et al. (2020). "WALLABY - an SKA Pathfinder HI survey". In: *Astrophysics and Space Science* 365.7, 118, p. 118. DOI: 10.1007/s10509-020-03831-4. arXiv: 2002.07311 [astro-ph.GA].

Kraljic, Katarina, Romeel Davé, and Christophe Pichon (2020). "And yet it flips: connecting galactic spin and the cosmic web". In: *Monthly Notices of the Royal Astronomical Society* 493.1, pp. 362–381. DOI: 10.1093/mnras/staa250. arXiv: 1906.01623 [astro-ph.GA].

Kravtsov, Andrey V. and Stefano Borgani (2012). "Formation of Galaxy Clusters". In: *Annual Review of Astronomy and Astrophysics* 50, pp. 353–409. DOI: 10.1146/annurev-astro-081811-125502. arXiv: 1205.5556 [astro-ph.CO].

Larson, Richard B. (1974). "Dynamical models for the formation and evolution of spherical galaxies". In: *Monthly Notices of the Royal Astronomical Society* 166, pp. 585–616. DOI: 10.1093/mnras/166.3.585.

Libeskind, Noam I. et al. (2018). "Tracing the cosmic web". In: *Monthly Notices of the Royal Astronomical Society* 473.1, pp. 1195–1217. DOI: 10.1093/mnras/stx1976. arXiv: 1705.03021 [astro-ph.CO].

Madau, Piero and Mark Dickinson (2014). "Cosmic Star-Formation History". In: *Annual Review of Astronomy and Astrophysics* 52, pp. 415–486. DOI: 10.1146/annurev-astro-081811-125615. arXiv: 1403.0007 [astro-ph.CO].

Martin, Ann M. et al. (2010). "The Arecibo Legacy Fast ALFA Survey. X. The H I Mass Function and Ω_H I from the 40% ALFALFA Survey". In: *The Astrophysical Journal* 723.2, pp. 1359–1374. DOI: 10.1088/0004-637X/723/2/1359. arXiv: 1008.5107 [astro-ph.CO].

McMullin, J. P. et al. (2007). "CASA Architecture and Applications". In: *Astronomical Data Analysis Software and Systems XVI*. Ed. by R. A. Shaw, F. Hill, and D. J. Bell. Vol. 376. Astronomical Society of the Pacific Conference Series, p. 127.

Meyer, Martin et al. (2017). "Tracing HI Beyond the Local Universe". In: *Publications of the Astronomical Society of Australia* 34, p. 52. DOI: 10.1017/pasa.2017.31. arXiv: 1705.04210 [astro-ph.CO].

Mo, Houjun, Frank C. van den Bosch, and Simon White (2010). *Galaxy Formation and Evolution*.

Mohr, Joseph J., Benjamin Mathiesen, and August E. Evrard (1999). "Properties of the Intracluster Medium in an Ensemble of Nearby Galaxy Clusters". In: *The Astrophysical Journal* 517.2, pp. 627–649. DOI: 10.1086/307227. arXiv: astro-ph/9901281 [astro-ph].

Muñoz, R. P. et al. (2013). "Dynamical analysis of strong-lensing galaxy groups at intermediate redshift". In: *Astronomy & Astrophysics* 552, A80, A80. DOI: 10.1051/0004-6361/201118513. arXiv: 1212.2624 [astro-ph.CO].

Mulchaey, John S. (2000). "X-ray Properties of Groups of Galaxies". In: *Annual Review of Astronomy and Astrophysics* 38, pp. 289–335. DOI: 10.1146/annurev.astro.38.1.289. arXiv: astro-ph/0009379 [astro-ph].

Neeleman, Marcel et al. (2016). "The H I Content of the Universe Over the Past 10 GYRS". In: *The Astrophysical Journal* 818.2, 113, p. 113. DOI: 10.3847/0004-637X/818/2/113. arXiv: 1601.01691 [astro-ph.GA].

Obreschkow, D. and S. Rawlings (2009). "The Cosmic Decline in the H_2/H I Ratio in Galaxies". In: *The Astrophysical Journal Letters* 696.2, pp. L129–L132. DOI: 10.1088/0004-637X/696/2/L129. arXiv: 0904.0213 [astro-ph.GA].

Offringa, A. R. et al. (2014). "WSCLEAN: an implementation of a fast, generic wide-field imager for radio astronomy". In: *Monthly Notices of the Royal Astronomical*

Society 444.1, pp. 606–619. DOI: 10.1093/mnras/stu1368. arXiv: 1407.1943 [astro-ph.IM].

Pan, Danny C. et al. (2012). "Cosmic voids in Sloan Digital Sky Survey Data Release 7". In: *Monthly Notices of the Royal Astronomical Society* 421.2, pp. 926–934. DOI: 10.1111/j.1365-2966.2011.20197.x. arXiv: 1103.4156 [astro-ph.CO].

Parkash, Vaishali et al. (2018). "Relationships between HI Gas Mass, Stellar Mass, and the Star Formation Rate of HICAT+WISE (H I-WISE) Galaxies". In: *The Astrophysical Journal* 864.1, 40, p. 40. DOI: 10.3847/1538-4357/aad3b9. arXiv: 1807.06246 [astro-ph.GA].

Pisano, D. J. et al. (2011). "An H I Survey of Six Local Group Analogs. II. H I Properties of Group Galaxies". In: *The Astrophysical Journal Supplement Series* 197.2, 28, p. 28. DOI: 10.1088/0067-0049/197/2/28. arXiv: 1110.3431 [astro-ph.CO].

Planck Collaboration et al. (2016). "Planck 2015 results. XIII. Cosmological parameters". In: *Astronomy & Astrophysics* 594, A13, A13. DOI: 10.1051/0004-6361/201525830. arXiv: 1502.01589 [astro-ph.CO].

Popping, A. et al. (2012). "Comparison of Potential ASKAP HI Survey Source Finders". In: *Publications of the Astronomical Society of Australia* 29.3, pp. 318–339. DOI: 10.1071/AS11067. arXiv: 1201.3994 [astro-ph.IM].

Ranchod, Shilpa et al. (2021). "MIGHTEE-HI: discovery of an H I-rich galaxy group at z = 0.044 with MeerKAT". In: *Monthly Notices of the Royal Astronomical Society* 506.2, pp. 2753–2765. DOI: 10.1093/mnras/stab1817. arXiv: 2107.01237 [astro-ph.GA].

Robson, Dylan and Romeel Davé (2020). "X-ray emission from hot gas in galaxy groups and clusters in SIMBA". In: *Monthly Notices of the Royal Astronomical Society* 498.3, pp. 3061–3076. DOI: 10.1093/mnras/staa2394. arXiv: 2003.04115 [astro-ph.GA].

Schechter, P. (1976). "An analytic expression for the luminosity function for galaxies." In: *The Astrophysical Journal* 203, pp. 297–306. DOI: 10.1086/154079.

Serra, Paolo et al. (2012). "The ATLAS^{3D} project - XIII. Mass and morphology of H I in early-type galaxies as a function of environment". In: *Monthly Notices of the Royal Astronomical Society* 422.3, pp. 1835–1862. DOI: 10.1111/j.1365-2966.2012.20219.x. arXiv: 1111.4241 [astro-ph.CO].

Serra, Paolo et al. (2015). "SOFIA: a flexible source finder for 3D spectral line data". In: *Monthly Notices of the Royal Astronomical Society* 448.2, pp. 1922–1929. DOI: 10.1093/mnras/stv079. arXiv: 1501.03906 [astro-ph.IM].

Silk, Joseph and Gary A. Mamon (2012). "The current status of galaxy formation". In: *Research in Astronomy and Astrophysics* 12.8, pp. 917–946. DOI: 10.1088/1674-4527/12/8/004. arXiv: 1207.3080 [astro-ph.CO].

Skrutskie, M. F. et al. (2006). "The Two Micron All Sky Survey (2MASS)". In: *The Astronomical Journal* 131.2, pp. 1163–1183. DOI: 10.1086/498708.

Smirnov, O. M. (2011). "Revisiting the radio interferometer measurement equation. I. A full-sky Jones formalism". In: *Astronomy & Astrophysics* 527, A106, A106. DOI: 10.1051/0004-6361/201016082. arXiv: 1101.1764 [astro-ph.IM].

Somerville, Rachel S. and Romeel Davé (2015). "Physical Models of Galaxy Formation in a Cosmological Framework". In: *Annual Review of Astronomy and Astrophysics* 53, pp. 51–113. DOI: 10.1146/annurev-astro-082812-140951. arXiv: 1412.2712 [astro-ph.GA].

Sousbie, T. (2011). "The persistent cosmic web and its filamentary structure - I. Theory and implementation". In: *Monthly Notices of the Royal Astronomical Society* 414.1, pp. 350–383. DOI: 10.1111/j.1365-2966.2011.18394.x. arXiv: 1009.4015 [astro-ph.CO].

Spergel, D. N. et al. (2003). "First-Year Wilkinson Microwave Anisotropy Probe (WMAP) Observations: Determination of Cosmological Parameters". In: *The Astrophysical Journal Supplement Series* 148.1, pp. 175–194. DOI: 10.1086/377226. arXiv: astro-ph/0302209 [astro-ph].

Steinmetz, Matthias (1999). "Numerical Simulations of Galaxy Formation". In: *Astrophysics and Space Science* 269, pp. 513–532. DOI: 10.1023/A:1017006732013. arXiv: astro-ph/9910002 [astro-ph].

Tacconi, L. J. et al. (2013). "Phibss: Molecular Gas Content and Scaling Relations in z ~1-3 Massive, Main-sequence Star-forming Galaxies". In: *The Astrophysical Journal* 768.1, 74, p. 74. DOI: 10.1088/0004-637X/768/1/74. arXiv: 1211.5743 [astro-ph.CO].

Thompson, A. Richard, James M. Moran, and Jr. Swenson George W. (2017). *Interferometry and Synthesis in Radio Astronomy, 3rd Edition*. DOI: 10.1007/978-3-319-44431-4.

Tudorache, Madalina N. et al. (2022). "MIGHTEE - H I. The relation between the H I gas in galaxies and the cosmic web". In: *Monthly Notices of the Royal Astronomical Society* 513.2, pp. 2168–2177. DOI: 10.1093/mnras/stac996. arXiv: 2204.03041 [astro-ph.GA].

Walter, Fabian et al. (2020). "The Evolution of the Baryons Associated with Galaxies Averaged over Cosmic Time and Space". In: *The Astrophysical Journal* 902.2, 111, p. 111. DOI: 10.3847/1538-4357/abb82e. arXiv: 2009.11126 [astro-ph.GA].

Wang, Jing et al. (2016). "New lessons from the H I size-mass relation of galaxies". In: *Monthly Notices of the Royal Astronomical Society* 460.2, pp. 2143–2151. DOI: 10.1093/mnras/stw1099. arXiv: 1605.01489 [astro-ph.GA].

Westmeier, T. et al. (2021). "SOFIA 2 - an automated, parallel H I source finding pipeline for the WALLABY survey". In: *Monthly Notices of the Royal Astronomical Society* 506.3, pp. 3962–3976. DOI: 10.1093/mnras/stab1881. arXiv: 2106.15789 [astro-ph.IM].

Whitaker, Katherine E. et al. (2012). "The Star Formation Mass Sequence Out to z = 2.5". In: *The Astrophysical Journal Letters* 754.2, L29, p. L29. DOI: 10.1088/2041-8205/754/2/L29. arXiv: 1205.0547 [astro-ph.CO].

Whiting, Matthew T. (2012). "DUCHAMP: a 3D source finder for spectral-line data". In: *Monthly Notices of the Royal Astronomical Society* 421.4, pp. 3242–3256. DOI: 10.1111/j.1365-2966.2012.20548.x. arXiv: 1201.2710 [astro-ph.IM].

Wiese, W. L. and J. R. Fuhr (2009). "Accurate Atomic Transition Probabilities for Hydrogen, Helium, and Lithium". In: *Journal of Physical and Chemical Reference Data* 38.3, pp. 565–720. DOI: 10.1063/1.3077727.

Wright, Edward L. et al. (2010). "The Wide-field Infrared Survey Explorer (WISE): Mission Description and Initial On-orbit Performance". In: *The Astronomical Journal* 140.6, pp. 1868–1881. DOI: 10.1088/0004-6256/140/6/1868. arXiv: 1008.0031 [astro-ph.IM].

Yun, M. S., P. T. P. Ho, and K. Y. Lo (1994). "A high-resolution image of atomic hydrogen in the M81 group of galaxies". In: *Nature* 372.6506, pp. 530–532. DOI: 10.1038/372530a0.

Zwaan, M. A. et al. (2005). "The HIPASS catalogue: Ω_{HI} and environmental effects on the HI mass function of galaxies". In: *Monthly Notices of the Royal Astronomical Society* 359.1, pp. L30–L34. DOI: 10.1111/j.1745-3933.2005.00029.x. arXiv: astro-ph/0502257 [astro-ph].